Tunneling dynamics of ultracold atoms

Juan Polo Gomez

Submitted in fulfillment of
the requirements for the degree of
Doctor of Physics

Thesis supervisor:
Dr. Verònica Ahufinger

Departament de Física
Universitat Autònoma de Barcelona

Bellaterra, September 2016

A mis padres

Acknowledgments

Primerament voldria agrair a la Verònica per donar-me l'oportunitat de fer un doctorat, i de fet, per ser la meva supervisora tan del treball grau com del de màster. Des de un primer moment m'has ensenyat que és fer recerca, com ser un bon científic i com treballant dur es poden aconseguir uns resultats amb els que pots estar satisfet amb tu mateix. Ja són bastants anys els que m'has hagut de suportar, espero que no hagi estat molt dur, però t'estic molt agraït per tot, has sabut quan exigir i quan deixar-me marge per aprendre jo mateix, has estat una excel·lent supervisora, i espero que puguem continuar treballant junts en el futur (tot i que intentaré evitar el més d'agost). També voldria agrair al Jordi, que tot i no haver estat el meu supervisor, sempre ha estat allà quan l'he necessitat i també he pogut gaudir de la oportunitat de treballar amb ell i amb la Verònica en un projecte. Es nota que als dos us agrada la ciència, i ho sabeu transmetre a la resta.

També voldria dedicar unes paraules a la resta de professors del grup. A en Gaspar per la seva passió explicant, al Francesc per estar sempre allà disposat a ajudar, al Juan i a la Marifí que han estat excel·lents professors a la carrera, al Todor amb el qui he compartit classes i és sempre apassionant parlar de física i al Ramón, amb qui també he compartit docència i que per mi és un exemple del que un professor a d'esdevenir amb el temps, agradable, accessible, graciós i apassionat pel que fa.

My short stays abroad were also wonderful experiences. In Durham, were I worked with Prof. Simon Gardiner, I learned so many things and, moreover, he made me feel part of his group, like I was one of his own PhD students. Thank you for this warm welcome and for the time that you have dedicated to our work while I was there. I also want to thank Anna Minguzzi and Frank Hekking, with whom I worked in Grenoble. The two of them have invested so much time in introducing me to a new field almost from scratch, and thanks to them I could learn so much in almost record time. I also want to thank them for offering me the opportunity to do a postdoc there, I am very

excited about starting it soon, because I am sure we will work on new things and that I will learn a lot.

Per descomptat no em puc oblidar del excel·lents companys de doctorat que he tingut. Quan vaig començar n'hi havia molts, i amb el temps alguns han anat marxant i d'altres entrant. A l'Albert li he d'agrair l'ajuda que em va donar al principi del doctorat, al Ricard per haver-me ensenyat que no només és important el que fas sinó com ho expliques, a l'Àlex per haver estat sempre allà donant-me forces i amb qui he tingut el plaer de col·laborar, al Juanlu amb qui porto uns anys compartint despatx i amb qui m'encanta parlar, tan de ciències com d'altres temes més seriosos, al Dani per ensenyar-me els vídeos bàsics per ser un doctorant al grup i, finalment, a les últimes incorporacions, al Gerard a qui li desitjo lo millor pel seu doctorat (que segur que ho trobarà) i a la Irene amb qui he compartit bones converses fent cafè i parlant de Galícia.

Han estat uns anys treballant dur, m'ha agradat molt el que he fet, però sempre tinc la sensació que no he dedicat prou temps a tothom, un exemple són els amics que he fet durant la carrera, tot els bons moments de la carrera han estat al seu voltant, espero que continuem veient-nos sempre, tot i que ens dispersem pel món, gràcies a tots, Xavi, Ernest, Pau Masters, Jofre, Bernat, Pau Santos, Pau Pulido, Linus, Marga, Oriol, Jaume, Txema, i alguns noms que em deixaré amb les preses de la tesis. Gràcies a tots per ser tan bons companys i amics. També deixo un petit comentari pels companys de pis durant la carrera, amb ells també m'ho he passat molt i molt bé, i ha estat un plaer compartir pis i passar quatre anys amb ells, Niko, Marc, Jandro i Biel.

Finalment, voldria agrair a la meva família. Sense el suport dels meus pares i del meu germà no hagués fet mai un doctorat, ni tan sols hagués anat a la universitat. Sempre m'han deixat fer el que he volgut però a la vegada m'han guiat i m'han intentat presentar totes les opcions, ajudant-me a escollir el millor per mi. Gràcies per tot, mai podré agrair suficient tot el que heu fet per mi. A la Rux també l'hi he d'agrair moltíssimes coses. M'ha ajudat molt durant aquests anys, m'ha obert a noves experiències, hobbies i sobretot m'ha hagut de suportar en els moments més complicats. Encara ens queda moltes coses a fer, però em tranquil·litza pensar que ho faré amb ella al costat.

Segur que me n'oblido de molta gent, era d'esperar... Gràcies a tots amb els que he compartit part d'aquesta etapa, potser en el moment d'escriure se m'ha passat algú, però tots heu influenciat en la persona que sóc ara.

Joan Polo Gomez
Bellaterra, Setembre de 2016.

List of publications by Juan Polo

The research contained in this thesis is supported by the publications listed below:

Chapter 3: Matter-wave bright soliton interferometer

1. J. Polo and V. Ahufinger, *Soliton-based matter-wave interferometer*, Phys. Rev. A **88**, 053628 (2013).

Chapter 4: Density profiles of a miscible two-component Bose–Einstein condensates

2. J. Polo, V. Ahufinger, P. Mason, S. Sridhar, T. P. Billam, and S. A. Gardiner, *Analysis beyond the Thomas-Fermi approximation of the density profiles of a miscible two-component Bose-Einstein condensate*, Phys. Rev. A **91**, 053626 (2015).

Chapter 5: Transport of ultracold atoms between concentric traps via spatial adiabatic passage

3. J. Polo, A. Benseny, Th. Busch, V. Ahufinger and J. Mompart, *Transport of ultracold atoms between concentric traps via spatial adiabatic passage*, New J. Phys. **18** 015010, (2016).

Chapter 6: Geometrically induced complex tunnelings for ultracold atoms carrying orbital angular momentum

4. J. Polo, J. Mompart, and V. Ahufinger, *Geometrically induced complex tunnelings for ultracold atoms carrying orbital angular momentum*, Phys. Rev. A **93**, 033613, (2016).

Chapter 7: Single atom edge-like states via quantum interference

5. G. Pelegrí, J. Polo, A. Turpin, M. Lewenstein, J. Mompart, V. Ahufinger *Single atom edge-like states via quantum interference*, *Submitted to Phys. Rev. Lett.* (2016).

Other publications of Juan Polo not contained in this thesis:

6. A. L. Marchant, T. P. Billam, M. M. H. Yu, A. Rakonjac, J. L. Helm, J. Polo, C. Weiss, S. A. Gardiner, and S. L. Cornish, *Quantum reflection of bright solitary matter waves from a narrow attractive potential*, Phys. Rev. A **93**, 021604(R), (2016).

7. A. Turpin, J. Polo, Yu. V. Loiko, J. Küber, F. Schmaltz, T. K. Kalkandjiev, V. Ahufinger, G. Birkl, and J. Mompart, *Blue-detuned optical ring trap for Bose-Einstein condensates based on conical refraction* , Opt. Express **23**, 1638-1650 (2015).

Contents

Preface

In this thesis, we explore systems of ultracold atoms in which quantum tunneling is the fundamental mechanism driving the dynamics. The theory describing the tunneling phenomenon was developed in the late 1920s [1–3] in order to explain the α-radioactivity emission at low energies. Since then, this theory has proven to be very successful to study quantum phenomena in a wide range of different fields such as nuclear physics [4, 5], quantum chemistry [6, 7], biophysics [8, 9], among others. Moreover, tunneling is a key element in many devices, such as scanning tunneling microscopes [10], superconducting quantum interference devices (SQUIDs) [11], atomic analogs of SQUIDs [12–15] and atomic interferometers [16]. In particular, nonlinear systems, in which tunneling occurs, can exhibit new phenomena such as the Josephson effect, which has been largely studied in superconducting devices [17, 18] and in ultracold atomic systems [19–22]. In addition, tunneling is also playing an important role in new emerging fields such as *Atomtronics* [23], where neutral atoms are used to build analogues of electronic circuits and devices [13, 14, 24–26].

The tunneling phenomenon is considered to be a purely quantum mechanical process in the sense that it lacks a classical analog. In particular, tunneling occurs when a particle is in a potential landscape with a classical energetically allowed region and a forbidden region, which are typically separated by a potential barrier. In general, a tunneling event takes place whenever a quantum particle is able to access the classically forbidden region without having the necessary kinetic energy. In order to see the main differences between the classical picture and the quantum picture we can juxtapose the two cases. In the classical picture, for a given initial velocity of the particle, two different situations can occur, either the particle has enough kinetic energy to overcome the potential barrier or otherwise the particle is completely reflected (see Fig. 1.1 top

Classical picture

Quantum picture
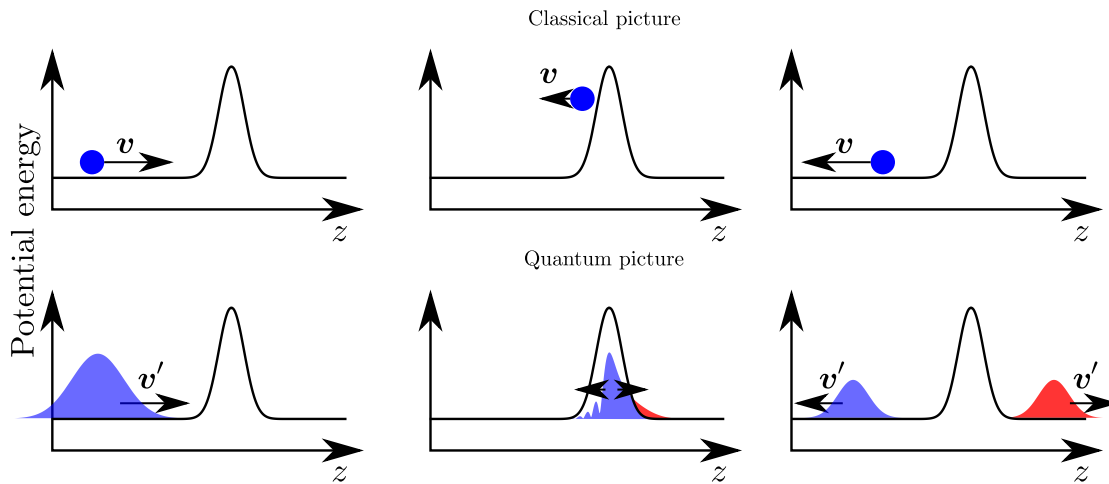
Figure 1.1: The first row shows a classical particle being reflected by a potential barrier. The second row shows the density profile of a quantum particle begin partially reflected and partially transmitted after a collision with a potential barrier. The length of the horizontal arrows gives a qualitatively indication of the modulus of the velocity of the classical particle and of the group velocity of the wavepacket.

row). On the other hand, in the quantum picture, where the wave character of the particle emerges, we find three different situations, the particle can be totally reflected, totally transmitted or partially reflected and transmitted (see Fig. 1.1 bottom row). This behavior is studied in many textbooks of Quantum Mechanics (see [27] for example) being the typical examples the ones of a free particle colliding with a delta barrier or with a rectangular potential barrier for which the reflection and transmission coefficients are calculated.

Up to now we have been discussing the tunneling of a single quantum particle through a potential barrier however, there is nothing that prevents us to consider larger systems or multiple particles. There are many examples where a mechanical system can be described within the theory of Quantum Mechanics and whose spatial scale is larger than the one of a single quantum particle. In fact, a very interesting question arises when considering macroscopic systems: how can we characterize the limits of quantum mechanics in macroscopic objects? A.J. Leggett in [28] addressed this question and proposed two strategies to determine the existence of macroscopic quantum behavior. The first consisted on designing an experiment where macroscopic quantum tunneling (MQT) could be observed and the second one creating a system where macroscopic quantum coherence was preserved over time.

One of the most appealing systems to study MQT are Bose–Einstein condensates (BECs), a state of matter where all the particles macroscopically occupy a single quantum state. BECs were predicted in 1924 by S. N. Bose while studying the quantum

statistics of photons [29] and was then extended to massive bosons by Einstein in 1924 [30, 31]. They predicted that, below a critical temperature, bosons undergo a quantum phase transition in which all particles occupy a single quantum state. In the atomic case, this phase transition occurs in a temperature range where de Broglie wavelength (which for free particles reads $\lambda_{dB} = \sqrt{2\pi\hbar^2/mk_BT}$ with m being the mass of the particle and T, $\hbar$ and k_B are the temperature, Planck constant and Boltzmann constant, respectively) becomes comparable to the average distance between particles and, the individual atomic wavefunctions overlap one another. BECs in atomic gases were first observed experimentally in 1995 by Eric Cornell and Carl Wieman [32], Wolfgang Ketterle [33] and Randall Hulet [34] after being able to cool down the atoms to temperatures of the order of nanokelvin. These remarkable experiments that required such low temperatures were only possible thanks to the previous advances on laser cooling techniques [35]. These achievements led to two Nobel prizes, one *for the development of methods to cool and trap atoms with laser light* awarded to Steven Chu, Claude Cohen-Tannoudji and William D. Phillips in 1997 and the second one *for the achievement of Bose-Einstein condensation in dilute gases of alkali atoms, and for early fundamental studies of the properties of the condensates* for Eric A. Cornell, Wolfgang Ketterle and Carl E. Wieman in 2001.

It is important to remark that atomic BECs are intrinsically nonlinear systems due to atom-atom interactions. In many situations, BECs can be described using a mean field theory, in which the nonlinearity is reduced to two-body contact interactions that leads to a cubic nonlinear term characterized by the s-wave scattering length, a_s. Depending on the atomic species, a_s can be modified, both in magnitude and in sign through Feshbach resonances using an external magnetic field [36–41] or by optical means [42, 43]. An interesting situation occurs when the scattering length vanishes and null nonlinear interactions are obtained. Then, the description of the BEC takes the form of a single quantum particle problem that can be described using the Schrödinger equation.

In the presence of nonlinearity, other macroscopic objects that are particularly compelling for studying MQT are matter-wave bright solitons [44, 45] created in BECs. These states propagate without distortion due to the compensation of nonlinearity and dispersion and are characterized by a density maximum and a constant phase. They can exhibit a particle-like behavior [46, 47] despite that their evolution is given by the same mean field nonlinear wave equation describing BECs. Nonetheless, sufficiently strong perturbations such as potential barriers [48] are able to overcome this localization and make the wave character of the soliton emerge. This particular behavior is crucial to applications such as interferometry where the splitting mechanism of matter-wave bright solitons through the interaction with a potential barrier has been largely studied in different situations: collisions with square barrier [49–51], with delta and narrow Gaussian potential barriers [52–58] and with finite width barriers [48] (a further discussion can be found in chapter 3).

Another form in which the tunneling phenomena can appear is through oscillations

between neighboring potentials. This behavior appears both in linear systems [59] and in nonlinear systems, and have been largely studied in two and three tunnel-coupled traps. In BECs, interactions bring new effects such as the macroscopic quantum self-trapping in double well potentials [19, 60], in which large amplitude coherent oscillations of the density are inhibited. Moreover, interactions can also enrich the dynamics of tunneling-based phenomena like the Josephson effect [19–22].

Generally, in tunnel-coupled systems it is assumed that atoms do not acquire any particular phase when a tunneling event occurs since, typically, tunneling amplitudes are real. However, it is possible to engineer systems where tunneling introduces a non-trivial phase into the atomic state, and thus, tunneling can then be regarded as an effective complex tunneling. Different proposals to generate these complex tunneling amplitudes have been recently reported, for instance, introducing a suitable force into an optical lattice [61], using a combination of radio-frequency and optical Raman coupling fields [62] and by employing angular momentum states in sided coupled cylindrically symmetric traps [63] (this last approach will be discussed in chapters 6 and 7). Complex tunnelings are particularly appealing for the generation of staggered fluxes [64, 65], implementation of the Hofstadter Hamiltonian and the observation of large homogeneous artificial magnetic fields [66], as well as the realization of the topological Haldane model [67] and of the Harper and Weyl Hamiltonians [68, 69].

In this thesis, we will explore some of the rich phenomena that tunneling provides in BECs and single atom systems. In chapter 2, we introduce some preliminary concepts, starting with the basic formalism describing BECs, which includes the derivation of the Gross-Pitaevskii equation and a discussion of its validity. We also review how the BEC description is affected by the dimensionality of the system by looking at the low dimensional Gross-Pitaevskii equation. Afterwards, the Thomas–Fermi approximation for the limit of strong nonlinear repulsive interactions is introduced. The mean field description of two-component BECs is also considered in this chapter. In addition, we present the soliton solutions of the one dimensional Gross-Pitaevskii equation and discuss some of their properties. Different trapping techniques for ultracold neutral atoms are reviewed, focusing on optically generated trapping potentials which are the more suitable to experimentally implement the potentials considered in this thesis. Finally, we introduce a model to describe the dynamics of a single atom in a system of weakly tunnel-coupled subsystems, using a subspace of eigenstates of the individual subsystems. Due to the generality of these few-state models they can be applied in many different situations; in particular, we will use them in chapter 5, chapter 6 and chapter 7.

In chapter 3, we study the implementation of a matter-wave interferometer using bright solitons in one dimensional BECs [48]. The system consists of a harmonic potential trap with a potential barrier located at its center on which an incident soliton collides and splits into two solitons. After the splitting event, the two solitons undergo a dipole oscillation in the harmonic trap and recombine at the position of the barrier. Our main focus is the characterization of the splitting process which we compare with

previous works where analytical solutions can be found [52, 53, 57]. We pay special attention to the case where the reflected and transmitted solitons have the same number of atoms. By means of a thorough analysis of the equally size splitting, we perform a characterization of the phase difference evolution during the whole process. We also find a semi-analytical formula to determine the main dependencies of the velocity of the split solitons and the phase difference on the velocity of the incident soliton, the nonlinearity and the width of the barrier. The implementation of the full interferometer sequence is tested by means of the phase imprinting method [70].

Chapter 4 is devoted to study the boundary regions of a harmonically trapped two-component BEC within the miscible phase [71]. We develop an analytical universal equation describing the boundaries separating different components in one, two and three dimensions. We also present a general procedure to solve the Thomas–Fermi approximation in all three spatial dimensionalities and find the frontier between the two different density patterns obtained within the miscible phase. These results aim to be used on precise analytical estimations of the ground state kinetic energy [72] and on calculations of the tunneling amplitudes to neighboring potentials [73].

In chapter 5 we study spatial adiabatic passage (SAP) processes [59] for a single atom in concentric tunnel-coupled traps [74]. We focus on ring geometries, and by making use of SAP techniques we provide a mechanism to load and transport an ultracold atom between the potentials in a robust way. First, we use the matter-wave analog of the RAP technique [75] to study the loading of an atom from a harmonic potential to a ring potential, and also to study the transport between two concentric ring traps. In addition, we use the matter-wave analog of the stimulated Raman adiabatic passage (STIRAP) technique [76] in a system of three concentric rings to transport the atom from the innermost to the outermost ring. In all the cases, we use a few-state model to describe the dynamics of the RAP-like and STIRAP-like processes obtaining an excellent agreement with the numerical simulations of the two-dimensional Schrödinger equation.

In chapter 6 we demonstrate that complex tunneling amplitudes appear naturally in the dynamics of orbital angular momentum states for a single ultracold atom trapped in two dimensional systems of sided coupled cylindrically symmetric identical traps [63]. Specifically, in this chapter we consider two in-line ring potentials and three rings in a triangular configuration whose Hilbert space consists of a set of decoupled manifolds spanned by ring states with identical vibrational and orbital angular momentum quantum numbers. Recalling basic geometric symmetries of the system, we determine that the tunneling amplitudes between different ring states, named cross-couplings, with (without) variation of the winding number, are complex (real). Moreover, we also show that a complex self-coupling between states with opposite winding number within a ring arises due to the breaking of cylindrical symmetry induced by the presence of additional rings. All these complex couplings can be controlled geometrically. We also demonstrate that, although for two in-line rings, the complex couplings are shown to give a non-physically relevant phase, in a triangular ring configuration they lead to the

possibility of engineering spatial dark states, which allows manipulating the transport of angular momentum states via quantum interference.

In chapter 7, we demonstrate that quantum interference leads to the appearance of robust edge-like states of a single ultracold atom in a two-dimensional optical ribbon [77]. We show that these states can be engineered either within the manifold of local ground states of the sites forming the ribbon, or of states carrying one unit of angular momentum. In the former case, we show that the implementation of edge-like states can be extended to other geometries, such as tilted square lattices. In the latter, we propose the use of the winding number associated to the angular momentum as a synthetic dimension to quantum simulate 3D systems in 2D optical ribbons.

We conclude in chapter 8 by summarizing the work presented in this thesis and discussing future perspectives.

Introduction

In this chapter, we give a brief overview of the main theoretical tools and concepts that we will use along the thesis to describe the different systems investigated. First, we introduce the Gross-Pitaevskii equation (GPE) (Sec. 2.1), a mean field wave equation that can be used to describe the dynamics of ultracold bosonic gases in a wide range of experimentally feasible parameters without using a full many-body description. In Sec. 2.1.1, we focus on BECs in different dimensionalities and discuss the validity of the mean field description when reducing the system dimensions. Section 2.1.2 is devoted to the limit of large interatomic interactions where the Thomas–Fermi approximation gives an analytical description of the ground state density profile of a repulsive BEC. In Sec. 2.2, we present the matter-wave soliton solution of the one dimensional homogeneous GPE. The GPE is extended to two-components in Sec. 2.3, where we also show the different phases appearing in these systems. Section 2.4 is devoted to the discussion of optically generated potentials using the dipole force and, finally, in Sec. 2.5 we derive a general technique to analytically describe a single atom trapped in tunnel-coupled systems using a subspace of subsystem eigenstates.

2.1   Gross–Pitaevskii equation

In this section we introduce the GPE, a mean field equation that describes the zero-temperature properties of a BEC in the weakly interacting regime.

From the microscopic theory, the many-body Hamiltonian in second quantization

describing a system of N bosons [78] reads:

$$\hat{H} = \int d\mathbf{r}\,\hat{\Psi}^\dagger(\mathbf{r})\left[-\frac{\hbar^2}{2m}\nabla^2 + V_{\text{ext}}(\mathbf{r})\right]\hat{\Psi}(\mathbf{r}) + \frac{1}{2}\int\int d\mathbf{r}\,d\mathbf{r}'\,\hat{\Psi}^\dagger(\mathbf{r}')\hat{\Psi}^\dagger(\mathbf{r})V(\mathbf{r}-\mathbf{r}')\hat{\Psi}(\mathbf{r}')\hat{\Psi}(\mathbf{r}),$$

(2.1)

where $\hat{\Psi}^\dagger(\mathbf{r})$ ($\hat{\Psi}(\mathbf{r})$) is the creation (annihilation) bosonic field operator with commutation relation $[\hat{\Psi}(\mathbf{r}'),\hat{\Psi}^\dagger(\mathbf{r})] = \delta(\mathbf{r}-\mathbf{r}')$ and $[\hat{\Psi}^\dagger(\mathbf{r}'),\hat{\Psi}^\dagger(\mathbf{r})] = [\hat{\Psi}(\mathbf{r}'),\hat{\Psi}(\mathbf{r})] = 0$. The first term in Eq. (2.1) corresponds to the single particle contribution, being $-(\hbar^2/(2m))\nabla^2$ the kinetic energy operator where m is the mass of the atomic species and $V_{\text{ext}}(\mathbf{r})$ the external potential acting on the external degrees of freedom. The second term corresponds to two-body elastic collisions, with $V(\mathbf{r}-\mathbf{r}')$ being the interatomic interaction potential.

For a sufficiently dilute gas at very low temperatures, only two-body s-wave collisions are relevant and thus, we can consider short-range isotropic interactions. In this regime, the interaction potential can be approximated to a pseudo-potential $V(\mathbf{r}-\mathbf{r}') = g_{3D}\delta(\mathbf{r}-\mathbf{r}')$ [78–80] with strength $g_{3D} = 4\pi\hbar^2 a_s/m$, characterized by the s-wave scattering length, a_s, [27] which can be positive ($a_s > 0$) or negative ($a_s < 0$) indicating that the effective interactions are repulsive or attractive, respectively. Note that a_s can be tuned in magnitude and sign using magnetic [36–38, 41] or optical [42, 43] Feshbach resonances.

Introducing the pseudo-potential potential $V(\mathbf{r}) = g_{3D}\delta(\mathbf{r}-\mathbf{r}')$ in Eq. (2.1) and integrating over $\mathbf{r}'$ we obtain:

$$\hat{H} = \int d\mathbf{r}\,\hat{\Psi}^\dagger(\mathbf{r})\left[-\frac{\hbar^2}{2m}\nabla^2 + V_{\text{ext}}(\mathbf{r}) + \frac{g_{3D}}{2}\hat{\Psi}^\dagger(\mathbf{r})\hat{\Psi}(\mathbf{r})\right]\hat{\Psi}(\mathbf{r}).$$

(2.2)

Using the Heisenberg picture, $i\hbar\partial_t\hat{A}(t) = [\hat{A}(t),\hat{H}]$ with $\hat{A}(t) = e^{i\hat{H}t/\hbar}\hat{A}e^{-i\hat{H}t/\hbar}$, and the commutation relations of the bosonic field operators introduced above, we obtain the temporal evolution of the field operators:

$$i\hbar\frac{\partial\hat{\Psi}(\mathbf{r}',t)}{\partial t} = [\hat{\Psi}(\mathbf{r}',t),\hat{H}] = \hat{\Psi}(\mathbf{r}',t)\hat{H} - \hat{H}\hat{\Psi}(\mathbf{r}',t),$$

$$= \hat{\Psi}(\mathbf{r}',t)\hat{H} - \int d\mathbf{r}\,\hat{\Psi}^\dagger(\mathbf{r},t)\left[-\frac{\hbar^2}{2m}\nabla^2 + V_{\text{ext}}(\mathbf{r}) + \frac{g_{3D}}{2}\hat{\Psi}^\dagger(\mathbf{r},t)\hat{\Psi}(\mathbf{r},t)\right]\hat{\Psi}(\mathbf{r},t)\hat{\Psi}(\mathbf{r}',t)$$

$$= \hat{\Psi}(\mathbf{r}',t)\hat{H} - \int d\mathbf{r}\left(\hat{\Psi}(\mathbf{r}',t)\hat{\Psi}^\dagger(\mathbf{r},t) - \delta(\mathbf{r}-\mathbf{r}')\right)\left[-\frac{\hbar^2}{2m}\nabla^2 + V_{\text{ext}}(\mathbf{r}) + \frac{g_{3D}}{2}\hat{\Psi}^\dagger(\mathbf{r},t)\hat{\Psi}(\mathbf{r},t)\right]\hat{\Psi}(\mathbf{r},t)$$

$$\quad + \int d\mathbf{r}\,\delta(\mathbf{r}-\mathbf{r}')\hat{\Psi}^\dagger(\mathbf{r},t)\frac{g_{3D}}{2}\hat{\Psi}^\dagger(\mathbf{r},t)\hat{\Psi}(\mathbf{r},t)\hat{\Psi}(\mathbf{r},t)$$

$$= \hat{\Psi}(\mathbf{r}',t)\hat{H} - \hat{\Psi}(\mathbf{r}',t)\hat{H} + \left[-\frac{\hbar^2}{2m}\nabla'^2 + V_{\text{ext}}(\mathbf{r}') + g_{3D}\hat{\Psi}^\dagger(\mathbf{r}')\hat{\Psi}(\mathbf{r}',t)\right]\hat{\Psi}(\mathbf{r}',t)$$

$$= \left[-\frac{\hbar^2}{2m}\nabla'^2 + V_{\text{ext}}(\mathbf{r}') + g_{3D}\hat{\Psi}^\dagger(\mathbf{r}')\hat{\Psi}(\mathbf{r}',t)\right]\hat{\Psi}(\mathbf{r}',t).$$

(2.3)

Within the mean field description, we can write the bosonic field operator as its expectation value plus an operator that accounts for thermal and quantum fluctuations $\hat{\Psi}(\mathbf{r}, t) = \langle \hat{\Psi}(\mathbf{r}, t) \rangle + \delta \hat{\Psi}(\mathbf{r}, t)$. By considering the zero temperature limit and a large number of particles, the thermal and quantum fluctuations can be neglected, and Eq. (2.3) gives the time evolution of the condensate wavefunction $\hat{\Psi}(\mathbf{r}, t) = \langle \hat{\Psi}(\mathbf{r}, t) \rangle$. It is the well-known Gross–Pitaevskii equation:

$$i\hbar \frac{\partial \Psi(\mathbf{r}, t)}{\partial t} = \left[-\frac{\hbar^2}{2m} \nabla^2 + V_{\text{ext}}(\mathbf{r}) + g_{3D} |\Psi(\mathbf{r}, t)|^2 \right] \Psi(\mathbf{r}, t); \qquad (2.4)$$

introduced by Gross [81] and Pitaevskii [82] in the 60's. In the above equation the wavefunction is normalized to the particle number $\int d\mathbf{r} \, |\Psi(\mathbf{r}, t)|^2 = N$. The time independent GPE is obtained by considering $\Psi(\mathbf{r}, t) = \Psi(\mathbf{r}) e^{-i\mu t/\hbar}$:

$$\left[-\frac{\hbar^2}{2m} \nabla^2 + V_{\text{ext}}(\mathbf{r}) + g_{3D} |\Psi(\mathbf{r})|^2 - \mu \right] \Psi(\mathbf{r}) = 0, \qquad (2.5)$$

where μ is the chemical potential, i.e., the energy required to extract a single atom from the system, and the total energy of the system within the mean field approach is given by [78]:

$$E = \int d\mathbf{r} \left[\frac{\hbar^2}{2m} |\nabla \Psi(\mathbf{r})|^2 + V_{\text{ext}}(\mathbf{r}) |\Psi(\mathbf{r})|^2 + \frac{g_{3D}}{2} |\Psi(\mathbf{r})|^4 \right]. \qquad (2.6)$$

2.1.1 Dimensionality

The effective dimensionality of a BEC can be reduced by confining the particles motion to zero point oscillations in one or two directions, obtaining a two dimensional (2D) [83–94] or a one dimensional (1D) [95–104] kinematical system, respectively. In particular, if we use a tightening harmonic potential with frequency $\omega_\perp$ the condition $\mu \ll \hbar \omega_\perp$ [105], with μ being the chemical potential, has to be satisfied in order to "freeze" the particles motion in the trapping direction.

When studying low dimensionalities, it is important to recall that BEC requires long-range order in the one-body density matrix $\rho(\mathbf{r}, \mathbf{r}') = \langle \hat{\Psi}(\mathbf{r}) \hat{\Psi}(\mathbf{r}') \rangle$. In 3D, $\rho(\mathbf{r}, \mathbf{r}')$ has a finite value [106], which permits the existence of true BEC for temperatures below the BEC transition temperature T_c [78]. In low dimensionalities, however, it has been found that at finite temperature, phase fluctuations of the bosonic field provide a power law (in 2D) or exponential (in 1D) decay of the one-body density matrix [107]. Nonetheless, for low dimensional trapped ultracold Bose-gases there are some temperature ranges where Bose–Einstein condensation exists. In particular, in the 2D case well below the transition temperature T_c true condensation occurs, however, for temperatures just below T_c only "quasicondensates" or condensates with fluctuating phase exist [108]. The superfluid transition in 2D BECs was first introduced by Berezinskii, Kosterlitz and Thouless (BKT) [109–111] in homogeneous systems, however, it has been shown that

in trapped systems the BKT transition [85, 112] is the one bringing the superfluid behavior in interacting 2D BECs. On the other hand, in 1D trapped ultracold Bose-gases there are three different regimes depending on the temperature, number of particles and nonlinear interactions [113]. For sufficiently low temperatures and large number of particles the phase fluctuations are suppressed due to the finite size of the system and true condensation occurs; however, for temperatures just below the degeneracy temperature T_d (see [113]) only quasicondensation or condensate with fluctuating phase exists. In addition, another regime emerges in the limit of infinitely strong repulsive interactions, the Tonks gas or gas of impenetrable bosons [114]. In this thesis, however, we will investigate weakly interacting low dimensional trapped systems, in which by assuming $T = 0$, true condensation is always possible.

An additional condition to describe BECs within the mean field is $\xi \gg d$, where d is the interparticle separation, which strongly depends on the dimensionality, and

$$\xi = \frac{1}{\sqrt{8\pi n a_s}} \tag{2.7}$$

is the healing length, that corresponds to the distance at which the kinetic energy term and the nonlinear interaction term balance.

Two-dimensional Bose–Einstein condensates

Let us consider a homogeneous BEC in the x and y directions which is confined in z by a harmonic trap, $V(z) = m\omega_z^2 z^2/2$, with an associated length scale $a_z = \sqrt{\hbar/m\omega_z}$.

Assuming a sufficiently tight confinement ($\mu \ll \hbar\omega_z$), the BEC wavefunction can be factorized to first order approximation into two parts, $\Psi(\mathbf{r}) = \phi(z)\psi(x,y)$ [78, 115]. The z dependent part of the wavefunction can be written as:

$$\phi(z) = \sqrt{n_{2D}}f(z')/\sqrt{a_z} \tag{2.8}$$

where $n_{2D} = \int dz\, |\Psi(\mathbf{r})|^2 = N/S$ is the two-dimensional density, with N/S being the number of particles over the total surface, $f(z')$ is a normalized function and $z' = z/a_z$ is the dimensionless z coordinate. Introducing the previously factorized wavefunction into Eq. (2.5) we obtain a wave equation for the order parameter $\phi(z)$ that takes the form of a one-dimensional time-independent dimensionless GPE:

$$\left(-\frac{1}{2}\frac{\partial^2}{\partial z'^2} + \frac{1}{2}z'^2 + 4\pi a_s n_{2D}f(z')^2 \right)f(z') = \frac{\mu}{\hbar\omega_z}f(z'). \tag{2.9}$$

The solution of this dimensionless differential equation, Eq. (2.9), is governed by the parameter $a_s n_{2D}$. Therefore, if we assume $a_s n_{2D} \ll 1$, the nonlinear part can be treated perturbatively and $f(z')$ can be approximated by the ground state of the tightening

harmonic potential in z', $f_{h.o.}(z')$. By imposing the normalization condition of $f_{h.o.}(z')$ in Eq. (2.9), we obtain the two-dimensional chemical potential:

$$\mu_{2D} = \frac{\hbar\omega_z}{2} + g_{2D}n_{2D}, \tag{2.10}$$

with a two-dimensional nonlinear parameter

$$g_{2D} = \sqrt{8\pi}\frac{\hbar^2}{m}\frac{a_s}{a_z}. \tag{2.11}$$

If we now consider Eq. (2.4) with a shallow confinement in the x and y directions, $V_{\text{ext}}(x,y)$, such that the trapping frequency on z is much larger than the x, y associated one and that $a_s n_{2D} \ll 1$ is satisfied everywhere, the total wavefunction can be factorized as $\Psi(\mathbf{r},t) = \phi_{h.o.}(z)\psi(x,y,t)$, where $\phi_{h.o.}(z)$ is the ground state of the harmonic potential in z. Introducing the factorized wavefunction into Eq. (2.4) multiplying by $\phi_{h.o.}^*(z)$ and integrating over z, one obtains the 2D Gross–Pitaevskii equation:

$$i\hbar\frac{\partial\psi(x,y,t)}{\partial t} = \left[-\frac{\hbar^2}{2m}\nabla^2 + V_{\text{ext}}(x,y) + g_{2D}|\psi(x,y,t)|^2\right]\psi(x,y,t). \tag{2.12}$$

One-dimensional Bose–Einstein condensates

Let us consider a longitudinally homogeneous BEC trapped in a tight radial harmonic potential with an associated length scale $a_r = \sqrt{\hbar/m\omega_r}$. For $\mu \ll \hbar\omega_r$ we can separate the wavefunction as $\Psi(\mathbf{r}) = \psi(z)\phi(r)$, where the radial wavefunction reads $\phi(r) = \sqrt{n_{1D}}f(r')/a_r$ with $n_{1D} = \int r\,dr\,d\theta\,|\Psi(\mathbf{r})|^2 = N/L$ being the homogeneous one-dimensional density, N/L is the number of particles over the total length, $r' = r/a_r$ is the dimensionless radial coordinate and $f(r')$ is a normalized function. Introducing the factorized $\Psi(\mathbf{r})$ into Eq. (2.5) we find that the radial equation describing the BEC can be written as a two-dimensional time-independent dimensionless GPE:

$$\left(-\frac{1}{2}\frac{\partial^2}{\partial r'^2} - \frac{1}{2r'}\frac{\partial}{\partial r'} + \frac{1}{2}r'^2 + 4\pi a_s n_{1D}f(r')^2\right)f(r') = \frac{\mu}{\hbar\omega_r}f(r'). \tag{2.13}$$

Considering the limit of $a_s n_{1D} \ll 1$, Eq. (2.13) can be solved, to first order approximation, by treating the nonlinear part perturbatively obtaining the ground state of the radial two-dimensional harmonic trapping potential $f_{h.o.}(r')$. By imposing the normalization condition on $f_{h.o.}(r')$ in Eq. (2.13) we find the following 1D chemical potential:

$$\mu_{1D} = \hbar\omega_r + g_{1D}n_{1D} \tag{2.14}$$

with

$$g_{1D} = 2\hbar\omega_r a_s, \tag{2.15}$$

being the one-dimensional interaction parameter.

Assuming a shallow confinement in the z direction, $V_{\text{ext}}(z)$, in Eq. (2.4) such that the radial trapping frequency is much larger than the associated z one and $a_s n_{1D} \ll 1$, we can still factorize the total wavefunction as $\Psi(\mathbf{r},t) = \psi(z,t)\phi_{h.o}(r)$, where $\phi_{h.o.}(r)$ is the two dimensional ground state of the radial harmonic potential. Introducing the factorized wavefunction into Eq. (2.4) multiplying by $\phi^*_{h.o.}(r)$ and integrating over r and θ the 1D GPE is obtained:

$$i\hbar\frac{\partial\psi(z,t)}{\partial t} = \left[-\frac{\hbar^2}{2m}\nabla^2 + V_{\text{ext}}(z) + g_{1D}|\psi(z,t)|^2\right]\psi(z,t). \tag{2.16}$$

2.1.2 Thomas–Fermi approximation

The Thomas–Fermi approximation (TFA) [116, 117] can be applied when the spatial variation of the density is much smaller than the healing length, Eq. (2.7). Under this condition, the kinetic energy or quantum pressure term of the GPE can be neglected in front of the nonlinear interaction term.

Here, we calculate within the TFA, the density profile of a D dimensional BEC trapped in an isotropic harmonic potential $V(\mathbf{r}) = m\omega^2|\mathbf{r}|^2/2$ and where a tight harmonic confinement in the "frozen" directions is applied for the $D = 1$ and $D = 2$ cases. We start from the Thomas–Fermi approximated time-independent GPE in D dimensions, i.e. neglecting the kinetic term in Eq. (2.5):

$$i\hbar\mu_D\psi(\mathbf{r}) = \left[\frac{1}{2}m\omega|\mathbf{r}|^2 - |g_D||\psi(\mathbf{r})|^2\right]\psi(\mathbf{r}), \tag{2.17}$$

from which we obtain the density, $n(\mathbf{r}) = |\psi(\mathbf{r})|^2$, to be:

$$n(\mathbf{r}) = \frac{\mu_D - \frac{1}{2}m\omega|\mathbf{r}|^2}{g_D}. \tag{2.18}$$

Note that the dimensionality is indicated as a subindex in the chemical potential, μ_D, and in the nonlinear interaction parameter g_D. The Thomas–Fermi radius (TFR), R_{TF}, is defined as the distance from the trap center at which the density vanishes, i.e:

$$R_{TF}^2 = \frac{2\mu_D}{m\omega}. \tag{2.19}$$

By imposing the normalization condition, $\int d\mathbf{r}\, n(\mathbf{r}) = N$, into the density given in

Eq. (2.18) we find the chemical potential:

$$\mu_D^{\frac{D+2}{2}} = \frac{g_D}{N\beta_D}\frac{D(D+2)}{2^D}\left(\frac{m\omega}{2}\right)^{D/2}. \tag{2.20}$$

where $\beta_D = 2\,(\pi)$ for $D = 1$ ($D = 2, 3$).

Finally, introducing Eq. (2.20) into Eq. (2.18), the density profile of the BEC within the TFA for any given dimension, $D = 1$, 2 and 3, is obtained. Note that the resulting density profile takes an inverted parabola shape instead of the Gaussian profile obtained in the noninteracting case, $g_D = 0$, corresponding to the ground state of the harmonic confining potential.

2.2   Matter-wave solitons

In general, solitons are solutions of nonlinear equations that fulfill three main properties: they are localized solutions, they propagate without changing their form, and they emerge unchanged after interacting with other solitons [118]. These solutions appear due to the presence of both, nonlinearity and dispersion, which can exactly compensate each other giving rise to non-dispersive waves. Strictly speaking, the term soliton is used for localized solutions of integrable models [119] such as, for instance, the 1D homogeneous GPE, equivalent to the 1D homogeneous nonlinear Schrödinger equation (NLSE), that takes the form:

$$i\hbar\frac{\partial\psi(z,t)}{\partial t} = \left[-\frac{\hbar^2}{2m}\nabla^2 + g_{1D}|\psi(z,t)|^2\right]\psi(z,t). \tag{2.21}$$

Soliton solutions can appear in different forms depending on the value and sign of the nonlinear interaction term. For example, two different soliton solutions exist in the 1D homogeneous GPE [119]: dark solitons which appear for repulsive interactions ($a_s > 0$) and whose density profile presents a dark region or notch with a sharp phase jump; and bright solitons, which appear for attractive interatomic interactions ($a_s < 0$) and are self-contained localized wavepackets with constant phase in which their own density produces the self-focusing effect. In Fig. 2.1, we present a schematic plot of the density profile of a dark and a bright soliton with their corresponding phase distribution. Note the characteristic π phase jump that dark solitons exhibit at the position of the notch and that bright solitons present a constant phase all across their density.

For concreteness, here we show the bright soliton solution of the homogeneous 1D GPE, Eq. (2.21). This solution is obtained through the inverse scattering transform technique [119–121] and reads:

$$\psi(z,t) = \sqrt{\frac{\alpha}{2}}\,\text{sech}\left[\alpha(z - z_0 - vt)\right]e^{i\phi(z,t)}, \tag{2.22}$$

where:

$$\phi(z,t) = \frac{mv}{\hbar}\left((z - z_0) - \frac{vt}{2}\right) + \frac{\hbar}{2m}\alpha^2 t + \theta, \qquad (2.23)$$

v is the soliton velocity, z_0 is its initial position, θ is an arbitrary initial phase and $\alpha = N\omega_r a_s m/\hbar$ with N, ω_r, a_s and m corresponding to the atom number, frequency of the radial confinement, s-wave scattering length and atomic mass, respectively.

Note that in experiments, there usually is a weak harmonic axial trap $V(z) = m\omega_z^2 z^2/2$ which breaks the integrability of the 1D homogeneous GPE. However, the system still admits soliton-like solutions [47, 122]. These solutions are localized wavepackets that propagate without distortion and are also known as solitary-wave solutions. Nevertheless, solitary waves are not always unconditionally stable as true soliton solutions are. Therefore, new phenomenology appears associated to the breaking of the stability of these states. In particular, in attractive 2D and 3D trapped BECs, collapse occurs [123]. In 2D BECs, collapse takes place when the number of particles exceeds a critical value [124, 125] while in 3D BECs [126], collapse can occur for any number of particles, and it is only suppressed for a small range of trapping and nonlinear interaction strength parameter values for which a 3D BEC metastable state exists [127–129]. Hereafter, and following the nomenclature used by the ultracold atom community, we will use the term soliton and solitary wave indistinctly.

Matter-wave bright solitons were first observed in lithium as soliton trains [44] and individual wavepackets [45], and few years later with rubidium atoms [128] in attractive BECs. Nonetheless, there are other situations in which it is possible to create bright solitons even with repulsive atom-atom interactions, it is the case when a wavepacket is prepared at the edge of the first Brillouin zone of a weakly periodic potential that presents anomalous dispersion [130]. The experimental realization of dark solitons, typically with rubidium, required new techniques and procedures due to its particular phase pattern (see Fig. 2.1b), so a different number of approaches were developed: phase-imprinting method [131, 132], density-engineering [133, 134], interference methods [135, 136] or using a fast moving barrier across the BEC [137].

In this thesis, we will study an application that makes use of the robustness and dispersionless behavior [138] of matter-wave bright solitons in 1D attractive BECs, which makes them ideal candidates for applications that require large coherent propagation lengths as they do not require a continuous wavepacket refocusing [139], a matter-wave interferometer. In particular, in chapter 3, we discuss the proposed matter-wave interferometer consisting of a harmonic potential trap with a potential barrier at its center in which an incident matter-wave bright soliton collides and splits into two solitons [48]. The two split solitons recombine after a dipole oscillation in the trap at the position of the barrier producing two output matter waves. This scheme presents an interesting property: after the recombination, the number of atoms at the outputs provides a measure of the phase difference between the two arms of the interferometer.

(a)

Bright soliton

(b)
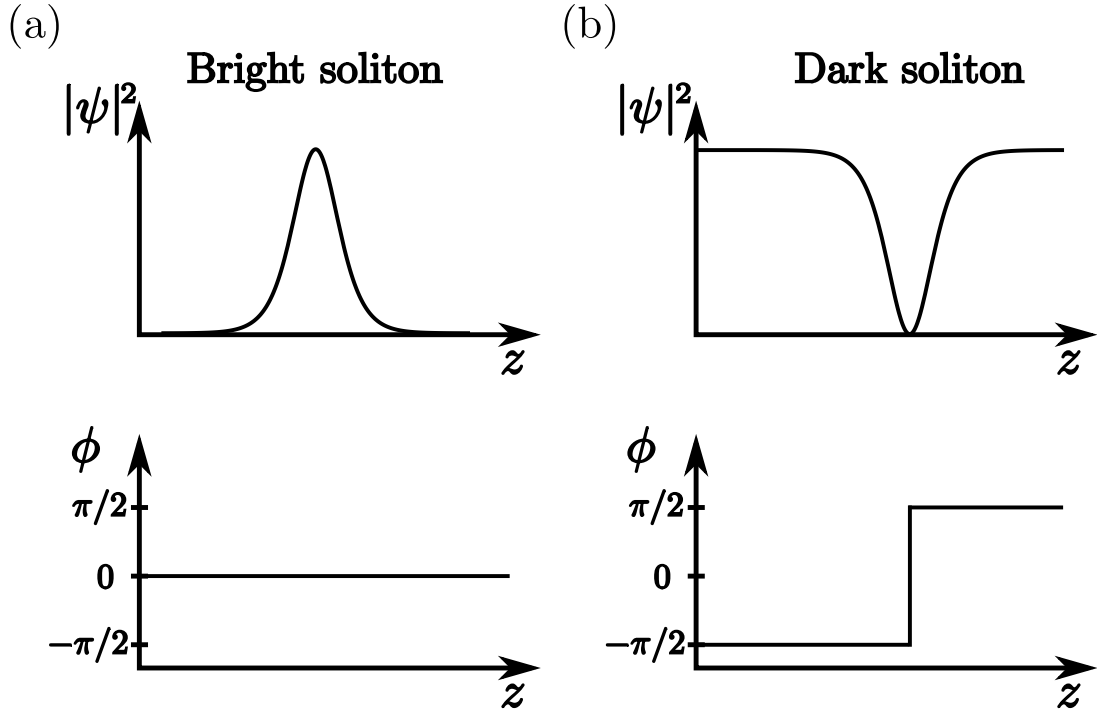
Dark soliton

Figure 2.1: Schematic figure of the density and phase of a bright (a) and a dark (b) soliton. Bright solitons are characterized by a density maximum together with a constant phase, while dark solitons exhibit a density notch and a phase jump at the position of the minimum.

2.3   Two-component Bose–Einstein condensates

In this section, we review the mean field description of two-component BECs (TCBECs) in which two quantum states are macroscopically occupied. TCBECs have been experimentally obtained using different approaches, such as using mixtures of two atomic species [140–144], two isotopes of the same species [145] or two hyperfine states of the same isotope [146–153].

These systems exhibit a large variety of complex density profiles [154–156] that have been subject of many theoretical and experimental studies. Some examples of the different density profiles appearing in TCBECs are symmetry-breaking states [157–159], vortex lattices [152, 160, 161] and skyrmions [162]. All these phenomena are possible thanks to the large number of controllable parameters in the system, going from atom number, masses, inter- and intra-species interactions, to the trapping frequencies that can be varied for each species independently. Consequently, analytical models are of great interest in order to explore the whole parameter space and then use numerical simulations for specific regions of interest.

First, we look at the theoretical mean field description that can be obtained by

generalizing the derivation of the GPE, Sec. 2.1, when assuming that there are no spin-exchange collisions. Two-coupled GPEs with an extra nonlinear interaction term, that accounts for the collisions between atoms in different components, are obtained from such a generalization [154, 163–165]. Thus, we refer to these equations as the two-component Gross–Pitaevskii equation (TCGPE), that reads:

$$
i\hbar\frac{\partial\Psi_s(\mathbf{r},t)}{\partial_t} = \left(-\frac{\hbar^2\nabla^2}{2m_s} + V_s(\mathbf{r}) + \tilde{g}_s N_s|\Psi_s(\mathbf{r},t)|^2 + \tilde{g}_{12}N_{3-s}|\Psi_{3-s}(\mathbf{r},t)|^2\right)\Psi_s(\mathbf{r},t)\ ,
$$
$$(2.24)$$

where $s = 1$ or 2 refers to each component of the BEC, whilst m_s, N_s and $V_s(\mathbf{r})$ are the mass, number of atoms and external potential of the s component, respectively. The intra- and inter-species interaction coefficients are given by $\tilde{g}_s = 4\pi\hbar^2 a_s/2m_s$ and $\tilde{g}_{12} = 2\pi\hbar^2(m_1+m_2)a_{12}/m_1 m_2$ where a_s and a_{12} are the s-wave intra- and inter-species scattering lengths, respectively; and both wavefunctions are normalized to unity.

2.3.1 Overlapping and segregated phases

The ground state of TCBECs exhibit two different phases depending on the ratio of the intra- and inter-species nonlinear interactions; an overlapping and a segregate phase [154]. Here we use the time-independent TCGPE of two homogeneous BECs, $V_s(\mathbf{r}) = 0$, which, by considering particle conservation, leads to the following expressions for the chemical potential of each component, μ_1 and μ_2 [80, 155, 166, 167]:

$$
g_1 N_2 n_1 + g_{12}N_2 n_2 = \mu_1
$$
$$
g_2 N_2 n_2 + g_{12}N_1 n_1 = \mu_2,
$$
$$(2.25)$$

where $n_1 = |\Psi_1(\mathbf{r})|^2$ and $n_2 = |\Psi_2(\mathbf{r})|^2$ are the densities of component 1 and 2, respectively.

In order to study the stability of the two-component homogeneous solution we look at how the energy increases for small density deviations (see Eq. (2.6) for the energy of a single component BEC). Since the first order density deviations cancel due to particle conservation, we analyze the second order ones:

$$
\delta^2 E = \frac{1}{2}\int d\mathbf{r}\left[\frac{\partial\mu_1}{\partial n_1}(\delta n_1)^2 + \frac{\partial\mu_2}{\partial n_2}(\delta n_2)^2 + \frac{\partial\mu_1}{\partial n_2}\delta n_1\delta n_2 + \frac{\partial\mu_2}{\partial n_1}\delta n_1\delta n_2\right].
$$
$$(2.26)$$

This second order variation of the total energy must be positive, as we assumed that the homogeneous solution is a stable solution. Thus, we obtain the following stability conditions:

$$
\frac{\partial\mu_1}{\partial n_1} > 0, \qquad \frac{\partial\mu_2}{\partial n_2} > 0,
$$
$$
\frac{\partial\mu_1}{\partial n_1}\frac{\partial\mu_2}{\partial n_2} - \frac{\partial\mu_1}{\partial n_2}\frac{\partial\mu_2}{\partial n_1} > 0.
$$
$$(2.27)$$

The first two conditions along with Eq. (2.25) and Eq. (2.26) translate into $g_1 > 0$ and $g_2 > 0$, i.e. repulsive interactions, and the third condition gives $g_1 g_2 > g_{12}^2$. Therefore, the so called miscible (overlapping) phase will satisfy the previous inequalities, otherwise, immiscibility (segregation) appears between the two components. Both phases, miscible and immiscible, have been experimentally observed in [142, 145] and [143, 145, 148], respectively.

In Fig. 2.2 we present an example of these two phases when using the TFA in harmonically trapped TCBECs. Figure 2.2 (a) shows the miscible phase where the two components overlap and Fig. 2.2 (b) shows the immiscible phase which, within the TFA, has no overlap between components.
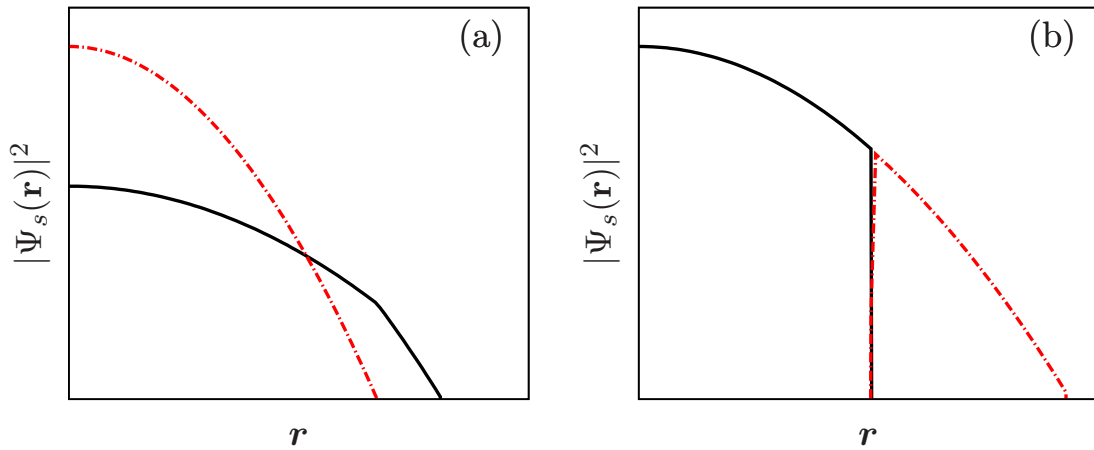
Figure 2.2: Examples of Thomas-Fermi density profiles of a 3D repulsive TCBEC trapped in a harmonic potential for the miscible, $g_1 g_2 > g_{12}^2$, (a) and the immiscible, $g_1 g_2 < g_{12}^2$, (b) phases.

In a real experimental situation, the density of each component of a trapped TCBEC always exhibits a small overlap, even in the immiscible phase [168, 169]. Therefore, an analytical characterization of the density around these areas, beyond the TFA, is important in order to understand the transition from the miscible to the immiscible phase in trapped systems [170, 171]. In addition, a description of these boundaries is not only important from the theoretical point of view, such as for estimating the kinetic energy [72, 73] or the penetration of one component into the other [168], but also for applications involving tunneling to neighboring potentials [73] or to study instabilities [172]. Thus, in chapter 4 we look at these boundary regions and develop an analytical formulation to study how one component penetrates into the other. We also compare our results with the ones obtained within the TFA and by integrating the GPE in the 1D, 2D and 3D cases [173].

2.4   Optical dipole traps

In this section, we discuss how the potentials that we have introduced so far as $V_{ext}(\mathbf{r})$, can be generated in current ultracold atom experiments. Ultracold neutral atoms can be trapped either magnetically, by means of the state-dependent force that an atom feels in the presence of an inhomogeneous magnetic field through the magnetic dipole moment [174], or optically, through the dipole force that appears due to the electric dipole interaction between the atoms and a far-detuned laser beam [175]. Note that in the literature we can also find the use of the radiation-pressure force to trap neutral atoms [176, 177]. However, even though it generates typical depths of the order of few kelvin, which allows to directly trap atoms from a thermal gas, it requires quasi-resonant light, leading to a temperature limit given by the photon recoil and thus, it cannot be used to trap BECs or single ultracold atoms in the ground state of potential traps, as we are interested here.

Magnetic traps are conservative traps which can reach trapping depths up to hundreds of milikelvin and are commonly used for the evaporative cooling process of BECs [178]. One of their main downsides is that they relay on the internal state of the atom, therefore, limiting their application to experiments that do not have internal state dynamics. Moreover, the geometries available are also limited, as magnetic traps are mostly generated using fix coils. Nonetheless, atom chips have opened new possibilities in this sense, creating complex circuitry arrangements [16, 101, 102, 179–181].

Optical traps based on the dipole force, which can also be understood in terms of a position dependent light shift due to spatial variation of light intensity [182], are generally weaker than magnetic traps, with depths under the milikelvin. However, they present some advantages, such as their independence of the ground-state sublevel being trapped, absence of excitations and the possibility to implement many different trapping geometries, specially with new techniques and tools such as spatial light modulators (SLM), [183–185] or time averaged potentials [186, 187]. Thus, in this section we will focus on optical dipole traps [188–191].

The dipole force obtained through the interaction of an atom with a far-detuned laser field is given by the gradient of the spatial intensity distribution of the field, $I(\mathbf{r})$ [182], offering a high flexibility on the possible trapping geometries that can be generated. Its sign is determined by the detuning $\delta = \omega_L - \omega_0$ (where $|\delta| < \omega_L, \omega_0$) with ω_L being the frequency of the laser field and ω_0 the atomic resonant frequency. When using the optical dipole force two different situations occur: (i) if $\delta > 0$, the laser is detuned towards the blue and the force acts repulsively from high intensity regions and (ii) for $\delta < 0$, the laser is red-detuned and the atom is attracted to high intensity regions.

Both, red-detuned and blue-detuned traps present advantages and drawbacks when applied to ultracold atoms. In red-detuned traps the atomic level structure suffers from different energy shifts depending on the specific state and intensity of the field, and moreover, some coherence losses appear caused by inhomogeneous differential light

shifts [192]. Blue-detuned traps are typically experimentally more demanding than red-detuned ones. However, they have some advantages such as a large reduction of photon scattering and of light-assisted losses, as atoms are placed in dark intensity regions.

In this thesis, we consider systems of ultracold atoms trapped in harmonic potentials of different dimensionalities and in ring potentials. Optical dipole potentials obtained by a focused light beam exhibit a Gaussian spatial profile. These potentials can be approximated by harmonic ones for the ground state of the system considering that, close to the center, the Gaussian intensity profile of the laser beam can be approximated by $e^{-x^2} \approx 1 - x^2$. Therefore, for simplicity harmonic-approximated potentials are typically created with red-detuned dipole traps [191, 193, 194], despite that there are also proposals to create them using a blue-detuned approach [195–199]. The generation of ring geometries is more involving, and has recently been investigated in the context of the emerging field of Atromtronics [23] and for applications to atomic interferometry [16]. Ring potentials are created using both, magnetic and dipole traps. Magnetic ring traps can be generated, for instance, with static magnetic fields [200–203], time-averaged magnetic fields [204–206], induction [207, 208] and radiofrequency adiabatic potentials [209]. Examples of red-detuned ring dipole traps include: optically plugging magnetic traps [210, 211], the use of static Laguerre-Gauss beams [212–216], painting potentials [183–185] and time averaged potentials [186, 187]. Blue-detuned ring traps have been performed using Laguerre-Gaussian (LG) beams generated with SLMs [217], amplitude masks [14, 218, 219] and the conical refraction phenomena [92] in which the region of minimum intensity is exactly zero due to interference. This last approach has the advantage of being an easy way to generate a toroidal dark trap, as a focused Gaussian beam undergoing the conical refraction phenomena in a biaxial crystal, makes the beam evolve in a double cone whose transverse intensity pattern at the focal plane is formed by a pair of concentric bright rings split by a dark intensity ring. It also provides the full conversion of the input power into the toroidal dark trap, in contrast to the previously reported methods which introduce losses due to diffraction in the generation of LG beams or due to the opaque regions of a mask. In addition it also presents a smooth intensity distribution, contrary to methods that use a limited number of pixels (SLMs).

2.5   Few-state model

In this section, we derive the few-state model. This model is able to describe the dynamics of systems formed by weakly tunnel-coupled multiple connected trapping potentials. First we focus on single atoms, however at the end of this section we discuss its application to other systems such as BECs.

We consider a single atom in a system formed by weakly tunnel-coupled subsystems

whose full dynamics is described by the Schrödinger equation (SE):

$$i\hbar\frac{\partial\Psi(\mathbf{r},t)}{\partial t} = \hat{H}_{SE}\Psi(\mathbf{r},t) = -\frac{\hbar^2}{2m}\nabla^2\Psi(\mathbf{r},t) + V(\mathbf{r})\Psi(\mathbf{r},t). \tag{2.28}$$

We assume that the dynamics of the total system can be enclosed within a subset of eigenstates of the individual subsystems and no excitations to other states occur. Let us define an orthogonal subset of eigenstates, $\{\Phi_1(\mathbf{r},t),...,\Phi_i(\mathbf{r},t),...,\Phi_n(\mathbf{r},t)\}$, of the individual subsystems, with $\Phi_i(\mathbf{r},t) = a_i(t)\psi_i(\mathbf{r})$, such that:

$$\int_{-\infty}^{\infty} d\mathbf{r}\,\psi_i(\mathbf{r})\psi_j(\mathbf{r}) = \delta_{i,j}. \tag{2.29}$$

By inserting $\Psi(\mathbf{r},t) = \sum_i^n \Phi_i(\mathbf{r},t)$ into Eq. (2.28) we find a set of n linearly coupled equations:

$$
\begin{aligned}
i\partial_t\phi_1(t) &= E_1 + J_{1,2}\phi_2 + ... + J_{1,n}\phi_n \\
i\partial_t\phi_2(t) &= J_{2,1}\phi_1 + E_2 + J_{2,3}\phi_3 + ... + J_{2,n}\phi_n \\
&\vdots \\
i\partial_t\phi_n(t) &= J_{n,1}\phi_1 + J_{n,3}\phi_3 + J_{n,4}\phi_3 + ... + E_n
\end{aligned}
\tag{2.30}
$$

with

$$
\begin{aligned}
E_i &= \int_{-\infty}^{\infty} d\mathbf{r}\,\psi_i^*(\mathbf{r})\hat{H}_{SE}\psi_i(\mathbf{r}) \\
J_{i,j} &= \frac{2}{\hbar}\int_{-\infty}^{\infty} d\mathbf{r}\,\psi_j^*(\mathbf{r})\hat{H}_{SE}\psi_i(\mathbf{r}),
\end{aligned}
\tag{2.31}
$$

where E_i is the eigenenergy of the ith subsystem eigenstate and $J_{i,j}$ is the coupling (or tunneling amplitude) between subsystem eigenstates i and j.

The previous set of linearly coupled equations can be written in matrix form, $i\hbar\partial_t\mathbf{a}(t) = \frac{\hbar}{2}\hat{H}_{FS}\boldsymbol{a}(t)$ with $\boldsymbol{a}(t) = (a_1(t), a_2(t), ..., a_n(t))^T$ with $\hat{H}_{FS}$ being the few-state Hamiltonian, as:

$$i\hbar\partial_t\begin{pmatrix} a_1(t) \\ a_2(t) \\ \vdots \\ a_n(t) \end{pmatrix} = \frac{\hbar}{2}\begin{pmatrix} E_1 & J_{1,2} & \cdots & J_{1,n} \\ J_{2,1} & E_2 & \cdots & J_{2,n} \\ \vdots & \vdots & \vdots & \vdots \\ J_{n,1} & J_{n,2} & \cdots & E_n \end{pmatrix}\begin{pmatrix} a_1(t) \\ a_2(t) \\ \vdots \\ a_n(t) \end{pmatrix}. \tag{2.32}$$

The above few-state model is able to describe the population dynamics of each subsystem eigenstate whenever the initial state lies within the manifold $\{\Phi_1(\mathbf{r},t),...,\Phi_i(\mathbf{r},t),...,\Phi_n(\mathbf{r},t)\}$ and the dynamics of the system does not introduce

excitations to states $\Phi_j(\mathbf{r}, t) \notin \{\Phi_1(\mathbf{r}, t), ..., \Phi_i(\mathbf{r}, t), ..., \Phi_n(\mathbf{r}, t)\}$. Note that, few-state models provide a state-like description of the dynamics, i.e. $|a_i(t)\rangle = \langle \mathbf{r}|\Phi_i(\mathbf{r}, t)\rangle$, where the information of the actual shape of the wavefunction is enclosed within the coupling parameter $J_{i,j}$.

Few-state models describing single atom dynamics have been successfully applied to spatial adiabatic passage (SAP)processes [59] to transport ultracold atoms between different types of traps and waveguides, to perform state filtering and also to build an interferometer in systems of 2D harmonic traps. In chapter 5, we derive a two- and a three-state model to describe the loading and the transport of a single ultracold atom in a system of cylindrically symmetric concentric traps by means of SAP.

Few-state models are mostly applied to spatially separated subsystem eigenstates, however, the model is not limited to that situation and can be applied to systems in which there are several eigenstates within the same subsystem, as long as they are orthogonal to each other. Examples are found when angular momentum states of a single atom trapped in 2D systems are considered. In this context, few-state models have been applied to the generation of angular momentum states [220] or in systems of 2D sided-coupled cylindrically symmetric potentials [63, 77]. This last case will be discussed in detail in chapters 6 and 7. In chapter 6, we use a few-state model to study the dynamics of angular momentum states for a single atom in systems of two and three tunnel-coupled rings. We demonstrate how the transport of orbital angular momentum states can be manipulated by means of geometrically engineering spatial dark states. In chapter 7 we propose a scheme to generate robust edge-like states of a single ultracold atom trapped in an optical ribbon [77]. In this chapter, a few-state model is used to characterize the manifold of local ground states and states carrying one unit of angular momentum spanned in the harmonic oscillators forming the ribbon.

Finally note that, few-state models can be generalized to nonlinear systems, and in particular they can be used to describe BECs in multiple trap systems. The main difference with respect to the linear case is that a nonlinear term appears in the diagonal of Eq. (2.32) that depends on the population of the subsystem eigenstate. For double well trapped BECs, where the model is known as two-state model or two-mode approximation, the model predicts Josephson-like dynamics [19, 60, 221, 222] and reproduces effects such as the macroscopic quantum self-trapping [19, 60] in which large amplitude coherent oscillations of the density are inhibited. A four state model has been applied to a BEC trapped in a double harmonic potential considering the ground state and first state of each well [223], having two subsystem eigenstates in each trap. The role of nonlinearity in SAP processes has also been explored within few-state models [59, 224].

Worth to mention is how few-state models have become a powerful and successful approach to untangle many complex effects observed in matter-wave systems. The main reason is that, within its limits of validity, they present an excellent agreement with the dynamics observed on their primitive equation of motion, either the SE or the GPE, as will be shown in chapters 5, 6 and 7 where we compare the results obtained with these

models with the numerical ones obtained by direct integration of the equation of motion describing the system.

Matter-wave bright soliton interferometer

In this chapter, we study the implementation of a matter-wave interferometer using bright solitons in 1D Bose–Einstein condensates (BECs) [48]. In particular, the interferometer here investigated consists of a harmonic potential trap with a potential barrier at its center on which an incident soliton collides and splits into two. Then, after a dipole oscillation in the harmonic potential, the two split solitons recombine at the position of the barrier. One of the key elements of this scheme is that, the number of particles at the two outputs gives a measure of the relative phase acquired by the two solitons undergoing the dipole oscillation.

Matter-wave interferometers make use of the wave character of the atoms in order to produce interference effects [16]. Inherent atomic properties, like mass or polarizability make atom interferometers ideal for high precision measurements of, for instance, inertia [225], rotations [226–229], accelerations [230–232], fundamental constants [233–237], testing general relativity [238–240] or gravitational waves [241, 242].

Atomic interferometers that use BECs may increase phase sensitivity since they present larger coherence length than single atom systems [135, 243, 244]. However, elastic collisions in BECs can produce phase diffusion which reduces the phase coherence [245–247]. Nonetheless, these limitations due to phase diffusion can be overcome using Feshbach resonances [248, 249] or introducing nonclassical correlations between the two arms of the interferometer [250, 251]. In addition, nonlinear interactions can give rise to squeezed states which allow to surpass the standard quantum limit [252–258]. Examples of BEC interferometers are: a three-path interferometer which have been used to measure h/m and the fine structure constant α [259], Michelson interferometer-like schemes [260, 261] or interferometers that use Bloch oscillations [248]. Other proposals explore the robustness against phase fluctuations in elongated BECs [262] and the

miniaturization of BEC interferometers [235, 263].

The use of matter-wave bright solitons [44] for interferometry was proposed by R. Hulet in [264], considering their potential to increase the phase sensitivity of atom interferometers even further due to their dispersionless coherent propagation which should allow for large interrogation times, localization, large visibility provided by the large number of atoms and robustness inherent to solitons [265]. These advantages have brought the attention of researchers leading to many theoretical proposals [71, 266–270] and experiments [104, 271].

One of the key elements in any interferometer is the splitting mechanism and, in matter-wave soliton interferometers it also plays a crucial role in their implementation. Thus, different methods have been reported to produce such splitting, for instance, applying a resonant $\pi/2$ pulse to an internal state transition of the atoms [267], using an accurate control of the scattering length in space or time [272], or using collisions with different potential barriers like square [49–51], narrow Gaussian [52, 56] and delta type [53–55, 57, 58] potential barriers.

In our case, we consider a finite width barrier known as Rosen–Morse barrier, similar to the ones used in experiments [104, 270]. We pay special attention to the splitting mechanism and how the phase difference between split solitons is affected by the collision process of the incident soliton with the potential barrier. In particular, we focus on the characterization of the equal-sized splitting, i.e., when the reflected and transmitted solitons have the same number of atoms. In general, it is assumed that the reflected soliton acquires an extra $\pi/2$ phase after the collision. However, our study indicates that, after the first collision, the soliton only acquires a $\pi/2$ phase for high incident velocities and very narrow barriers, otherwise the relative phase after the collision strongly depends on the nonlinearity, width of the barrier and incident velocity. Moreover, we also observe that the velocity of the reflected and transmitted solitons also depend on these parameters and, in general, the reflected soliton is slower than the transmitted one. Finally, we test the implementation of the full interferometer sequence by means of the phase imprinting method [70].

This chapter is organized in five sections. In the first section we describe the physical system under investigation. In Sec. 3.2 we study the dependencies of the transmission coefficient on the nonlinearity and width of the barrier. Section 3.3 is devoted to the analysis of the splitting process focusing on the equal-sized splitting case, i.e., when the reflected and transmitted solitons have exactly the same number of particles. Section 3.4 is dedicated to the recombination process and Sec. 3.5 to the conclusions.

3.1   Physical system

We consider a BEC at zero temperature in a tight transverse harmonic confinement such that the effective dynamics is 1D, and thus, it can be described within the mean field approximation using the 1D GPE (Eq. (2.16) derived in Sec. 2.1.1), in which the wavefunction was normalized to N. We will be considering negative scattering lengths, $a_s < 0$, corresponding to attractive interactions for which matter-wave bright soliton solutions appear. Nonetheless, recall that the bright soliton solution shown in Sec. 2.2, Eq. (2.22), is only valid in the homogeneous case, but it can still be used to describe the ground state of an attractive BEC in a quasi-one dimensional geometry for sufficiently weak axial confinement [273].

In the absence of external potential, the total energy of the soliton can be separated into three contributions [274]:

$$E_t = E_k^p + E_k^v + E_{int}, \tag{3.1}$$

where:

$$E_k^p = \frac{\hbar^2}{2m} \int dz \left| \frac{\partial |\Psi(z)|}{\partial z} \right|^2 = \frac{\alpha^2 \hbar^2}{6m}, \tag{3.2}$$

$$E_k^v = \frac{\hbar^2}{2m} \int dz \left| |\Psi(z)| \frac{\partial}{\partial z} \exp\left[i\varphi(z,t)\right] \right|^2 = \frac{m}{2} v^2, \tag{3.3}$$

$$E_{int} = -\frac{g_{1D}}{2} \int dz \, |\Psi(z)|^4 = -\frac{\alpha^2 \hbar^2}{3m}, \tag{3.4}$$

being E_k^p the quantum pressure term, E_k^v the kinetic energy given by the gradient of the phase of the soliton, and E_{int} the energy due to the nonlinearity.

For the implementation of this interferometer, first a matter-wave bright soliton is created in a harmonic external potential trap. Then, the potential trap is suddenly displaced a distance d in the z direction making the soliton acquire potential energy (Fig. 3.1 (a)). As we discussed in Sec. 2.2, in many situations, solitons can be described using particle models [46, 47, 275]; here we use this approach to estimate the kinetic energy of the soliton. The particle models suggests that the potential energy, given by the displacement, is fully converted into kinetic energy once the soliton reaches the center of the trap, therefore, $E_k^v = E_p = \frac{1}{2}m\omega_z^2 d^2$ with ω_z being the frequency of the axial confinement. At this time, a potential barrier on which the soliton will collide, is located at the center of the displaced harmonic trap.

Here we use a Rosen–Morse potential barrier, instead of the previously investigated narrow Gaussian [52, 56], delta [53–55, 57, 58] and square [49–51] potential barriers, which reads:

$$V_{RM} = V_b \operatorname{sech}^2 \left(\frac{z}{\sigma} \right) \tag{3.5}$$
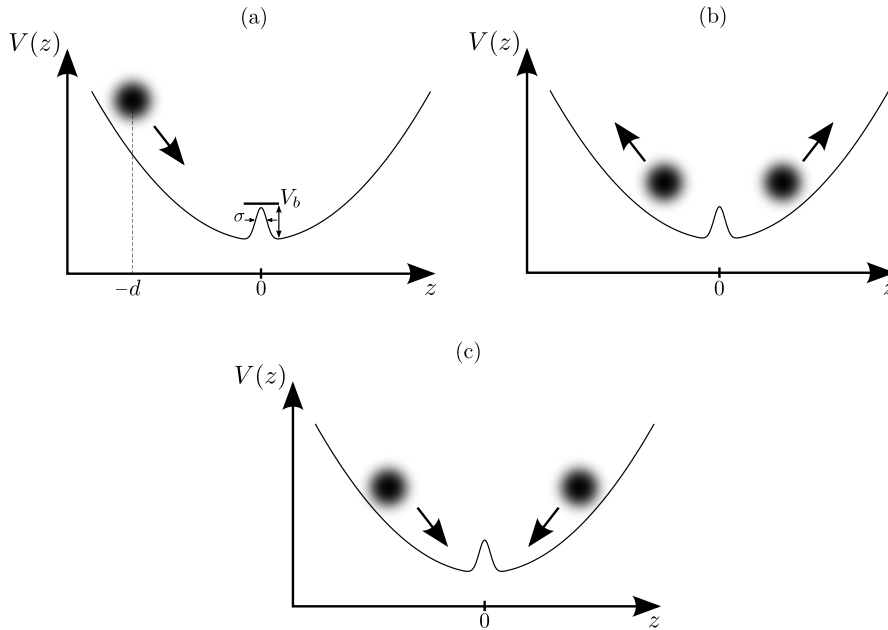
Figure 3.1: Schematics of the interferometer sequence: (a) the initial situation, in which the soliton is displaced with respect to the center of the harmonic potential trap by a distance d; (b) the two split solitons obtained after the collision with the barrier separate from each other and (c) the two solitons return to the position of the barrier and collide.

where V_b and σ are the strength and the width of barrier, respectively. This barrier is a sech-squared-shape potential that presents an analytical solution in the linear regime in the same fashion as the square and delta potential barriers do. However, the Rosen–Morse potential barrier provides a far better approximation of the potential created by a focused light beam by means of the dipole light force (Gaussian shape) [276–280]. Moreover, the absence of sharp edges in the Rosen–Morse barrier, contrarily to the delta and squared potentials, avoids sharp point effects [279] that can introduce errors when reproducing the behavior of realistic experimental barriers.

Therefore, the total potential used after the displacement d is given by:

$$V(z) = \frac{1}{2}m\omega_z^2 z^2 + V_b \operatorname{sech}^2\left(\frac{z}{\sigma}\right). \tag{3.6}$$

In the next step of the interferometer sequence the incident soliton splits into two solitons which propagate in opposite directions undergoing a dipole oscillation in the harmonic potential (Fig. 3.1 (b)). Finally, the two solitons recombine at the position of the barrier (Fig. 3.1 (c)) producing two outputs which number of particles provides a measure of the phase difference between the two arms of the interferometer.

3.2   Transmission coefficient

The first requirement for the implementation of a matter-wave bright soliton interferometer is to possess a mechanism to coherently split the incident soliton in two identical solitons. In our system, such a mechanism is provided by the interaction between the soliton and the Rosen–Morse potential barrier as described in Sec. 3.1.

In Fig. 3.2 we show the transmission coefficient as a function of the kinetic energy of the incident soliton, E_k^v, for different values of the nonlinear interaction term. E_k^v does not contain the quantum pressure term, i.e., it is only due to the gradient of the soliton phase as shown in Eq. (3.3). The transmission coefficient is defined as:

$$T = \int_0^\infty |\Psi(z, t = \pi/\omega_z)|^2 \, dz, \tag{3.7}$$

and it is obtained numerically at a time such that the two split solitons are well separated from each other $(t = \pi/\omega_z)$.
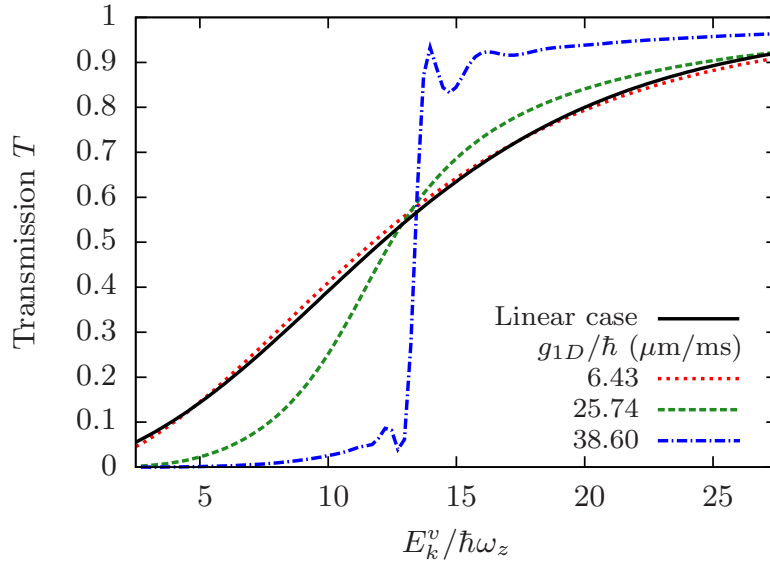
Figure 3.2: Transmission coefficient as a function of the kinetic energy of the incident soliton for different values of the nonlinear interaction term. The solid line corresponds to the analytical solution of the Rosen–Morse potential barrier obtained in the linear regime. The parameter values are: $V_b = 17.14\hbar\omega_z$, $\sigma = 0.67$ μm and $\omega_z = 2\pi \times 78$ Hz.

From Fig. 3.2, it can be seen that the nonlinearity dominates the behavior of the transmission coefficient. The kinetic energy of the incident soliton necessary to obtain a fixed value of the transmission coefficient decreases (increases) with the nonlinearity for $T > \overline{T}$ $(T < \overline{T})$, where $\overline{T}$ is a value around transmission coefficients of 0.5, being $\overline{T} = 0.57$ for the case shown in Fig. 3.2. Taking into account that the nonlinearity tends to hold all the atoms together, as g_{1D} increases, the shape of the transmission coefficient becomes

sharper, favoring the transmission (reflection) for $T > \overline{T}$ ($T < \overline{T}$). For large enough strength of the nonlinear interactions, the transmission coefficient exhibits a step-like behavior in which the incident soliton is either completely transmitted or completely reflected. This step-like behavior has also been reported for square barriers [281, 282] which resembles the classical particle behavior shown in Fig. 1.1. The analytical linear transmission coefficient of a Rosen–Morse potential of strength V_b and width σ when $\frac{8mV_b\sigma^2}{\hbar^2} > 1$ [283]:

$$T_{RM} = \frac{\sinh^2\left(\sigma\pi\sqrt{\frac{2mE_k^v}{\hbar^2}}\right)}{\operatorname{sech}^2\left(\sigma\pi\sqrt{\frac{2mE_k^v}{\hbar^2}}\right) + \cosh^2\left(\frac{\pi}{2}\sqrt{\frac{8mV_b\sigma^2}{\hbar^2} - 1}\right)}, \qquad (3.8)$$

is plotted also in Fig. 3.2 (solid line) for comparison, in good agreement with the numerical results in the limit of low nonlinearity.

A comparison of the transmission coefficients of a delta, square and Rosen–Morse potential barriers can be found in Appendix A.

3.3   Equal-sized splitting

In this section we focus on the case where the two split solitons have the same number of atoms, i.e., $T = 0.5$, reproducing the behavior of a 50-50 beam splitter.

First, we consider a fixed width of the barrier and fixed nonlinearity, and modify the potential strength, V_b, in such a way that we obtain the equal-sized splitting for different velocities of the incident soliton. We consider incident velocities and widths of the barrier achievable in current experiments [264] but also we study very high incident velocities and very narrow barriers to approach the limit of the delta potential barrier. In all the cases $E_k^v < V_b$, i.e., we ensure that the system remains in the tunneling regime.

For the analysis of the splitting mechanism we switch off the external harmonic potential trap in order to take into account only the effects produced by the interaction between the soliton and the barrier and we focus on three main issues: in Sec. 3.3.1 we calculate the area of the potential barrier required to obtain the equal-sized splitting; in Sec. 3.3.2 we study the difference between the velocity of the transmitted and reflected solitons and its relation with the velocity of the incident soliton; and in Sec. 3.3.3 we characterize the phase difference between the transmitted and reflected solitons.

3.3.1   Rosen–Morse vs. Delta barrier

In Fig. 3.3 we show the area of the Rosen–Morse potential barrier, $A = 2V_b\sigma$, required to obtain a fixed transmission coefficient of 0.5, as a function of the velocity of the incident soliton for different values of the width of the barrier and a fixed nonlinearity (Fig. 3.3 (a)) and for different values of the nonlinear interaction parameter and a fixed width of the barrier (Fig. 3.3 (b)).

For high velocities of the incident soliton and very narrow barriers (Fig. 3.3 (a)) the area of the barrier has approximately a linear dependence with the velocity of the
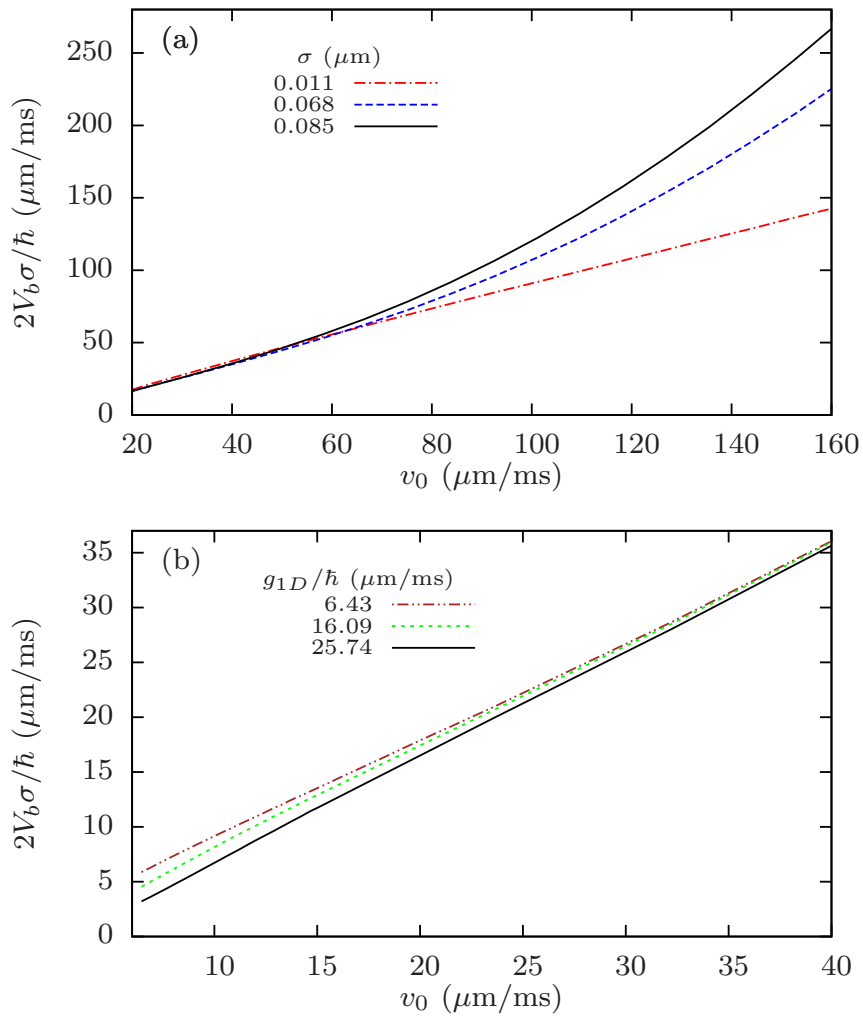

Figure 3.3: Area of the Rosen–Morse barrier as a function of the velocity of the incident soliton, while keeping the transmission coefficient fixed at $T = 0.5$, for different values of the width of the barrier and a fixed $g_{1D}/\hbar = 25.74$ μm/ms (a) and for different values of the nonlinear interactions and a fixed width of the barrier $\sigma = 0.085$ μm (b).

incident soliton. Thus, retrieving the behavior for a delta potential barrier, for which the transmission coefficient, Eq. (A.4), of a free particle as a function of the incident velocity reads [284]:

$$T_D = \frac{1}{1 + \frac{V_D^2}{\hbar^2 v_0^2}},$$ (3.9)

with V_D being the strength of the delta potential barrier and v_0 the velocity of the incident particle. From Eq. (3.9), in order to keep T_D equal to 0.5, the strength of the delta potential barrier must have a linear dependence with the incident velocity $V_D = \hbar v_0$. In the Rosen–Morse barrier for $T = 0.5$, we recover a linear dependence of the area with respect to the incident velocity only for $V_b \to \infty$ and $\sigma \to 0$ while keeping the product $V_b \sigma$ constant, but with a different slope than in the delta potential case that depends on the nonlinearity.

For wider barriers (Fig. 3.3 (a)), we have found an approximately quadratic behavior of the area of the Rosen–Morse potential barrier with respect to the incident velocity for a fixed width of the barrier and a fixed nonlinearity. We can also see that the growth of the area of the barrier with respect to the velocity of the incident soliton is steeper as the width of the barrier increases. Note that, we only take the limit of high incident velocities for very thin barriers as for wider barriers the incident soliton splits in more than two pieces.

In order to analyze the effects of the nonlinearity, in Fig. 3.3 (b) we study low incident velocities and we observe that as g_{1D} increases, for a fixed width of the barrier, the area of the barrier necessary to keep $T = 0.5$ decreases. This effect is consistent with the dependence on the nonlinearity of the transmission coefficient as a function of E_k^v (shown in Fig. 3.2). For a fixed E_k^v and for $T < \overline{T} = 0.57$, as g_{1D} increases, the transmission coefficient decreases. Thus, the potential strength of the barrier should decrease in order to maintain the equal-sized splitting. Note also that all these effects introduced by the nonlinearity decreases as the incident velocity increases.

3.3.2 Velocity of the split solitons

In this section we present an interesting effect that we have observed in the considered nonlinear system when the incident soliton undergoes the collision with the barrier. Even if the reflected and transmitted solitons have the same number of atoms after the splitting event, they do not behave symmetrically. In particular we observe that in general, the reflected soliton is slower than the transmitted one and the velocity difference between the two split solitons depend on the width of the barrier and on the strength of the nonlinear interaction.

Figure 3.4 shows the numerically calculated ratio between the absolute value of the velocity of the reflected (transmitted) soliton and the velocity of the incident soliton as a function of the velocity of the incident soliton, for different values of the width
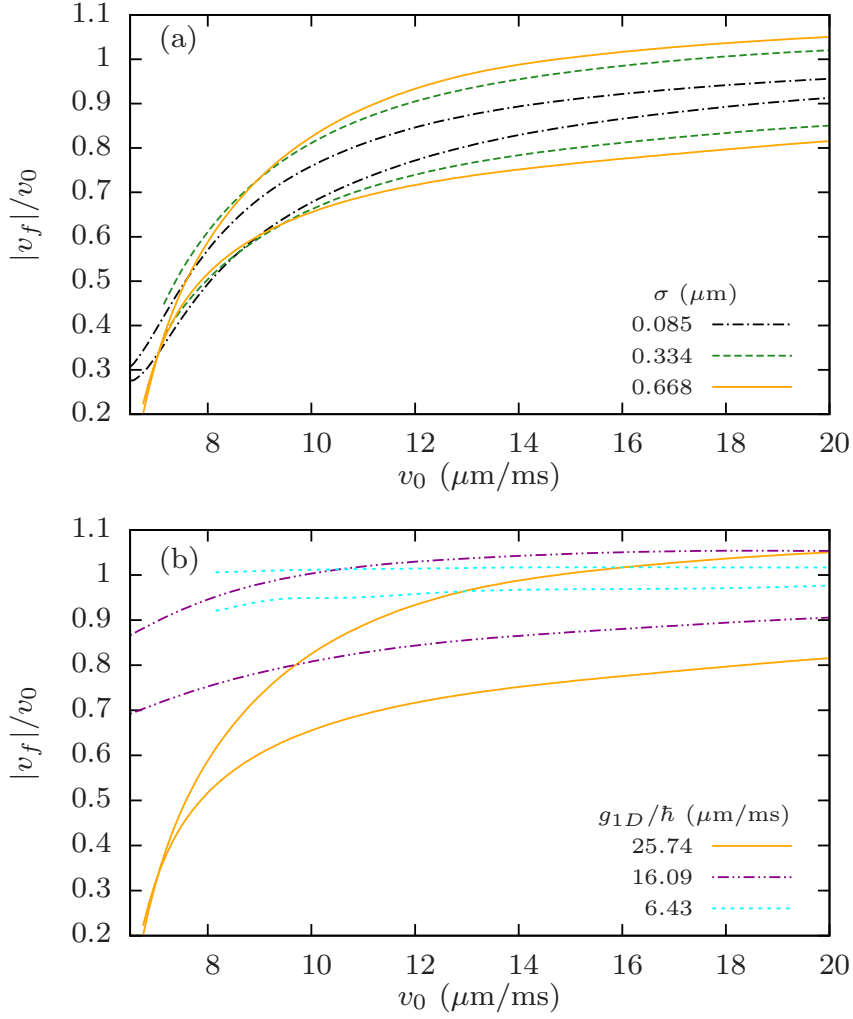
Figure 3.4: Ratio between the modulus of the velocity of the reflected (transmitted) soliton and the velocity of the incident soliton as a function of the velocity of the incident soliton for a fixed $T = 0.5$ for different values of the width of the barrier for a fixed $g_{1D}/\hbar = 25.74$ μm/ms (a) and for different values of the nonlinear interactions for a fixed width of the barrier $\sigma = 0.668$ μm (b). The velocities of the transmitted and reflected solitons are represented with the same line type, being in each case the velocity of the reflected soliton the lower curve.

of the barrier for a fixed g_{1D} (Fig. 3.4 (a)) and for different values of the nonlinearity for a fixed σ (Fig. 3.4 (b)). In each case, the lower curve corresponds to the reflected soliton. The difference between the absolute values of the velocities of the transmitted and reflected solitons increases as the width of the barrier increases (Fig. 3.4 (a)). We also observe that, for low velocities of the incident soliton, as the nonlinearity increases (Fig. 3.4 (b)), the split solitons are slowed down and eventually they become trapped

at the position of the barrier. This effect also appears in rectangular barriers [282] and limits the maximum value of the nonlinearity in order to maintain the 50-50 splitting.

Notice also that the mean of the absolute value of the velocities of the two split solitons, $\overline{\Delta v} = (|v_T| + |v_R|)/2$, is practically independent of the width of the barrier (Fig. 3.4 (a)) but it is strongly affected by the nonlinearity (Fig. 3.4 (b)). Also, $\overline{\Delta v}$ approaches the velocity of the incident soliton for high incident velocities i.e., the ratio $\overline{\Delta v}/v_0$ tends to one as the incident velocity increases. In Fig. 3.4 we can also see that the velocity of the transmitted soliton is, in some cases, higher than the velocity of the incident one. Nevertheless, the increase of velocity of the transmitted soliton is accompanied by a decrease of the velocity of the reflected soliton and therefore the total energy is conserved.

We recall that the difference in velocity of the split solitons introduces an accumulated phase difference between the two arms of the interferometer as they phase evolution due to the velocity is given by $e^{-i\frac{mv}{2\hbar}t}$, as we can see in Eq. (2.22). This effect does not reduce the sensitivity, but requires a calibration of the interferometer.

3.3.3   Phase difference

Here we analyze the phase difference introduced during the splitting process when the two split solitons have the same number of atoms. By performing a detailed analysis of the phase evolution during the splitting of a soliton colliding with a Rosen–Morse potential barrier, we are able to observe a strong dependence on the width of the barrier, velocity of the incident soliton and nonlinearity. These dependences go beyond the single soliton solution (Eq. (2.22) and Eq. (2.23)) of the GPE and requires to consider the n-soliton solution obtained by Zakharov and Shabat [119, 285], which shows that neighbor solitons make their presence felt through phase and position shifts:

$$\Psi(z,t) = \sum_{j=1}^{n} \Psi_j(z,t), \tag{3.10}$$

with:

$$\Psi_j(z,t) = A_j \sqrt{\frac{\alpha}{2}} \operatorname{sech}\left[A_j \alpha (z - z_{0j} - v_j t) + q_j\right] \tag{3.11}$$

$$\times \exp\left[i\left\{\frac{mv_j}{\hbar}\left((z - z_{0j}) - \frac{v_j t}{2}\right) + \frac{\hbar}{2m}A_j^2 \alpha^2 t + \theta_j + \psi_j\right\}\right],$$

where A_j corresponds to the amplitude of the jth soliton, q_j and ψ_j are the position and phase shift, respectively, which are given by [285]:

$$q_j + i\psi_j = \sum_{k \neq j} \pm \ln\left[\frac{A_j + A_k + i(v_j - v_k)m/2\hbar\alpha}{A_j - A_k + i(v_j - v_k)m/2\hbar\alpha}\right]. \tag{3.12}$$

In fact, we find that the phase difference introduced during the splitting of a matter-wave bright soliton into two solitons by colliding with a potential barrier arises from two

main sources: the interaction between the soliton and the barrier and the interaction between the reflected and transmitted solitons. The influence of this soliton-soliton interaction has been recently discussed [52] when two solitons collide at the position of a potential barrier.

High incident velocities

Figure 3.5 shows the phase difference between transmitted and reflected solitons for a fixed transmission coefficient, $T = 0.5$, as a function of the mean of the absolute values of the velocities of the two split solitons, $\overline{\Delta v}$, for high incident velocities and for different widths of the barrier and a fixed nonlinearity (Fig. 3.5 (a)) and for different nonlinearities and a fixed width of the barrier (Fig. 3.5 (b)). We compute the phase difference of the two split solitons when they are separated 10 μm in order to avoid the self-interferences that appear in the reflected soliton just after the splitting. We observe that the phase difference increases as $\overline{\Delta v}$ increases, and its growth depends on the width of the barrier (Fig. 3.5 (a)). For a fixed width of the barrier (Fig. 3.5 (b)), the phase difference introduced during the splitting process in the case of high incident velocities increases as the nonlinearity increases. Taking into account these dependences with the parameters of the system and the phase shift due to the presence of two neighboring solitons, we approximate the phase difference introduced during the splitting of a matter-wave bright soliton by interacting with a Rosen–Morse barrier for high velocities of the incident soliton (solid line of Fig. 3.5) as:

$$\Delta\phi(\overline{\Delta v}) = -2\arctan\left(\frac{g_{1D}}{2\hbar\overline{\Delta v}}\right) + C_1 + C_2\sqrt{\overline{\Delta v}} \qquad (3.13)$$

where C_i, with $i = 1, 2$, are independent of $\overline{\Delta v}$ but depend on the parameters of the system, and in our case have been adjusted numerically. The first term of the right hand side of Eq. (3.13) corresponds to the phase shift associated to the soliton-soliton interaction derived from Eq. (3.12)) and that is highly affected by g_{1D}. The second term provides a phase difference due to the interaction of the incident soliton with the barrier that does not depend on $\overline{\Delta v}$ but in general is strongly affected by the nonlinearity, growing as the nonlinearity increases. The third term depends on $\sqrt{\overline{\Delta v}}$, and its growth is determined by C_2 which is highly affected by the width of the barrier. Our results recover the analytical phase difference predicted for a delta potential barrier in the limit of $\sigma \to 0$ and very high incident velocities (see Fig. 3.5 (a) with $\sigma = 0.011$ μm). In this limit, the first term of Eq. (3.13) tends to zero due to its inverse dependence on $\overline{\Delta v}$, the last term, which depends on the width of the barrier, also tends to zero and only remains the term C_1 which tends to $\pi/2$ for high enough incident velocities. Thus, retrieving the delta potential barrier behavior [53, 286].

Figure 3.5: Phase difference between the transmitted and reflected solitons as a function of the mean of the absolute values of the velocities of the two split solitons for a fixed transmission coefficient of 0.5 and high velocities of the incident soliton for different values of the width of the barrier and a fixed $g_{1D}/\hbar = 25.74$ μm/ms (a) and for different values of the nonlinear interactions and a fixed $\sigma = 0.085$ μm (b). Solid lines correspond to the semi-analytical fit given by Eq. (3.13) with the parameters C_i (i=1,2) adjusted numerically.

Low incident velocities

Here we focus on velocities of the incident soliton and widths of the barrier compatible with the range of parameter values available in current experimental setups [264]. In this regime, we obtain similar general dependences with the width of the barrier and the nonlinearity as the ones described for high incident velocities, but with a considerable deviation with respect to the semi-analytical fit given by Eq. (3.13). This may be due to the increase of the interaction time between soliton and barrier for low velocities. As

for the case of high velocities of the incident soliton, the width of the barrier determines the growth of the phase difference with the mean of the absolute values of the velocities of the two split solitons (Fig. 3.6 (a)), while the nonlinearity affects mainly the arctangent dependence of the phase difference as shown in Fig. 3.6 (b). From Fig. 3.6 (b) we can also notice that the range of represented points is shifted to higher values of the mean of the absolute values of the split solitons as the nonlinearity decreases. This is related with the slowing down of the split solitons (discussed in Sec. 3.3.2) for large nonlinearities. Thus, the same velocity of the incident soliton, v_0, leads to different $\overline{\Delta v}$ for different nonlinearities.
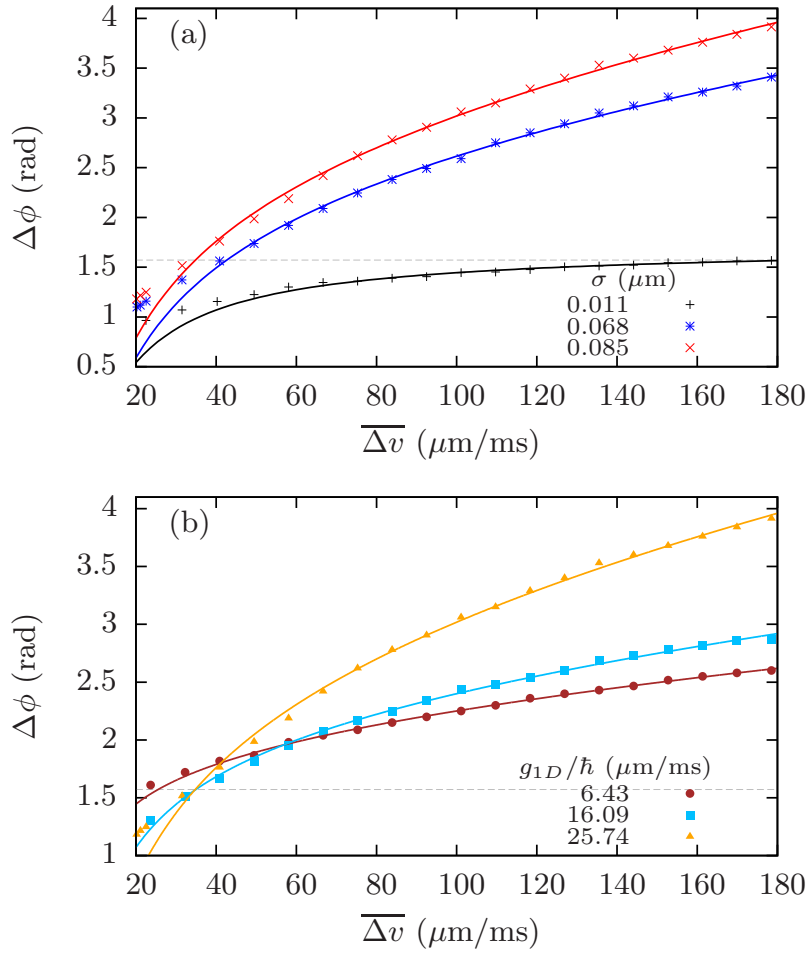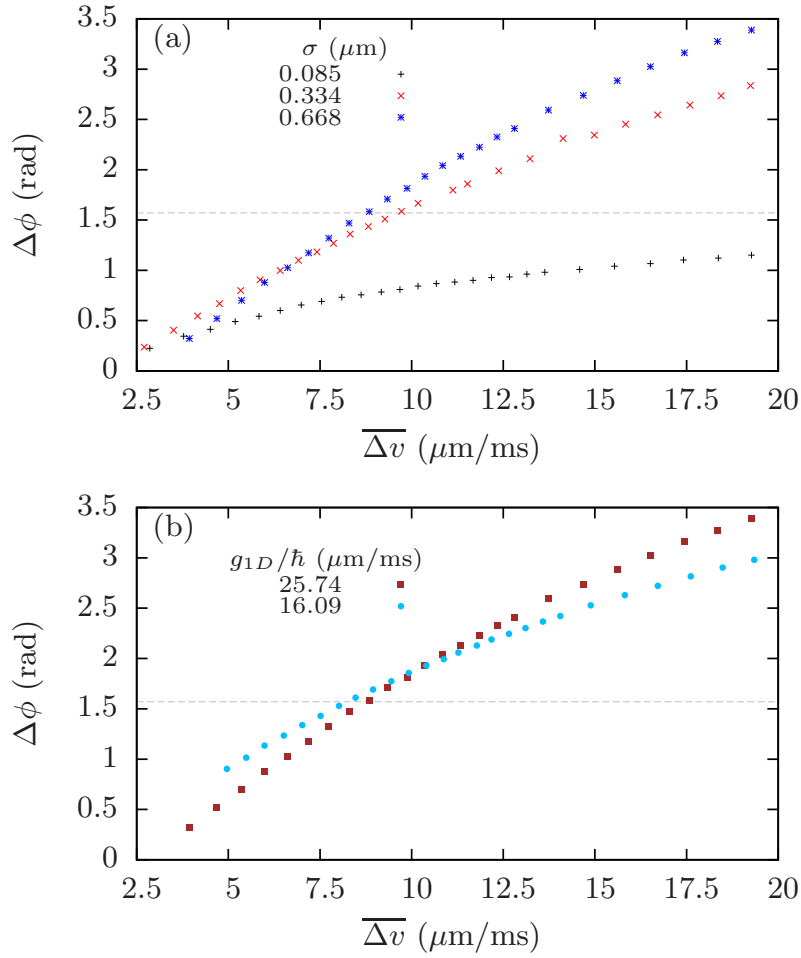

Figure 3.6: Phase difference between the transmitted and reflected solitons as a function of the mean of the absolute values of the velocities of the two split solitons for low velocities of the incident soliton, for a fixed transmission coefficient of 0.5, and for different values of the width of the barrier and a fixed $g_{1D}/\hbar = 25.74$ μm/ms (a) and for different values of the nonlinear interactions and a fixed width of the barrier $\sigma = 0.668$ μm (b).

3.4   Recombination

In this section we study the complete evolution of the interferometric sequence described in Fig. 3.1. Figure 3.7 shows the phase evolution of the incident soliton (solid line) and of the two equal-sized split solitons (dashed and dotted lines) as a function of time during the interferometric sequence: (i) the incident soliton (solid line) moves towards the potential barrier, during the first 2.8 ms of the evolution, converting its potential energy into kinetic energy; (ii) the soliton collides with the Rosen–Morse barrier (gray area between 2.8 and 3.7 ms) and splits into two solitons with different phases and different velocities (dashed and dotted lines); (iii) the two solitons perform a dipole oscillation in the trap for approximately 5.4 ms which provides an oscillatory behavior of the phase, different for each of the solitons due to their different velocities after the splitting (see Sec. 3.3.2); (iv) finally, the two solitons recombine at the position of the barrier (gray area starting at 9.1 ms) giving two output solitons.

The number of atoms at the two outputs of the interferometer depends on the phase difference between the transmitted and reflected solitons at the position of the barrier during the recombination process. We have tested the implementation of the interferometer by means of the phase imprinting method [70], modifying instantaneously the phase of one of the arms of the interferometer.

Figure 3.7: Phase evolution of a matter-wave bright soliton of ^{7}Li with 4×10^3 atoms (solid line) and the two split solitons (dashed and dotted lines) as a function of time during the complete interferometric sequence. The parameter values are: $V_b = 16.09\hbar\omega_z$, $\omega_z = 2\pi \times 78$ Hz, $\sigma = 0.67$ μm, $\omega_r = 2\pi \times 800$ Hz, $d = -20$ μm and $a_s = -0.16$ nm

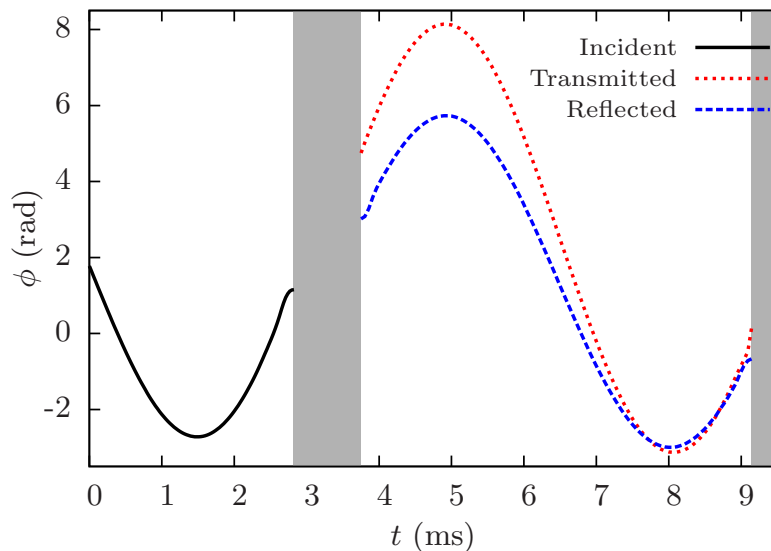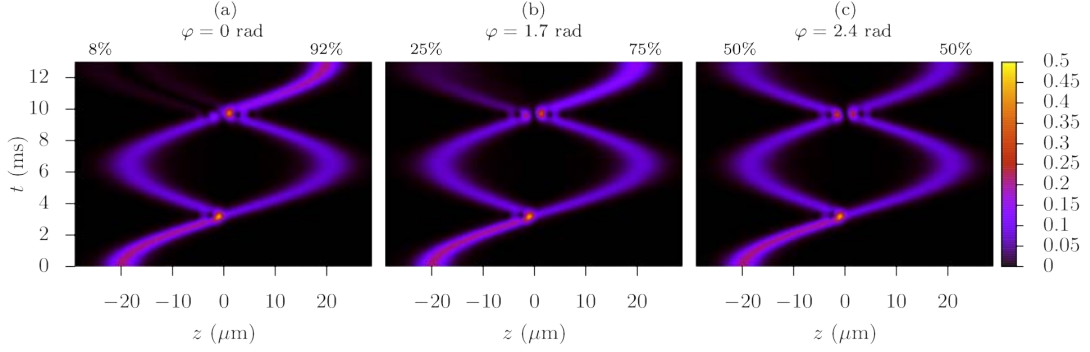Figure 3.8: Contour plot of the atomic density, $|\psi(z,t)|^2$, during the splitting and recombination processes for an incident soliton of ^{7}Li with 4×10^3 atoms and $a_s = -0.16$ nm centered at $d = -20$ μm in a harmonic external potential with $\omega_z = 2\pi \times 78$ Hz, $\omega_r = 2\pi \times 800$ Hz and a Rosen-Morse barrier with height $V_b = 16.09\hbar\omega_z$ and width $\sigma = 0.67$ μm. We plot three different imprinted phases: (a) $\varphi = 0$ rad, (b) $\varphi = 1.7$ rad, (c) $\varphi = 2.4$ rad, which produce 92%, 75% and 50% of the initial number of atoms at the right output, respectively.

Figure 3.8 (a) shows the density evolution of the incident and split solitons without any imprinted phase. Figure 3.8 (b) and (c) correspond to the cases of imprinted phases of $\varphi = 1.7$ rad and $\varphi = 2.4$ rad, respectively. Clearly, the number of atoms at the outputs of the interferometer is dominated by the phase difference between the two solitons in the recombination stage.

3.5   Conclusions

In this chapter we have studied the implementation of a matter-wave bright soliton interferometer composed of a harmonic external potential trap with a Rosen–Morse potential barrier at its center. We have focused on the analysis of the splitting process for the case where the two split solitons have exactly the same number of atoms. First, we have shown that the area of the Rosen-Morse barrier necessary to obtain the equal-sized splitting retrieves the delta behavior for very thin barriers and very high incident velocities. Otherwise, a quadratic behavior of the area of the barrier with the velocity of the incident soliton appears. We have also reported that the velocities of the reflected and transmitted solitons are strongly affected by the nonlinearity being both solitons slowed down, and eventually trapped at the position of the barrier, for high enough nonlinearities. In addition, we have found that, in general, the reflected soliton is slower than the transmitted one. We have also characterized the phase difference between the two split solitons. For high velocities of the incident soliton we have derived a semi-analytical fit that reproduces the main dependences on the velocity, width of the

barrier and nonlinearity for the equal-sized splitting, recovering the delta behavior in the limit of high incident velocities and extremely thin barriers. Finally, we have analyzed the recombination process, studying first the phase evolution in the full interferometric sequence, and then we have tested the performance of the interferometer, introducing a phase difference between its two arms by means of the phase imprinting method [70] showing that the number of atoms at each of the outputs is strongly affected by the relative phase of the two arms of the interferometer.

Density profiles of a miscible two-component Bose-Einstein condensates

In this chapter, we investigate the density profile of a harmonically trapped two-component Bose–Einstein condensate (TCBEC) within the miscible phase [173]. We develop an analytical formulation that is able to describe the boundary regions of each component beyond the Thomas–Fermi approximation (TFA) using a universal equation in 1D, 2D and 3D trapped systems. We also present a general procedure to solve the TFA for all three spatial dimensionalities and find the frontier that separates the two different regimes existing within the miscible phase, the coexisting and spatially separated regimes.

Many theoretical studies have addressed the density profiles of TCBECs depending on the ratio between the intra- and inter-species interaction strengths [154, 156, 168, 287, 288]. However, most of these theoretical studies are numerical or based on the TFA [116, 117]. The Thomas–Fermi (TF) approach neglects the kinetic energy term in the time independent Gross–Pitaevskii equation (GPE), on the grounds that its contributions are, to a significant extent, dominated over by those due to the nonlinear interaction term (see Sec. 2.1.2 for further details on this approximation). Thus, it can give good approximations of, for instance, the condensate chemical potential or the order parameter near its maximum value, however, close to the order parameter boundaries, where the atomic densities are low, the TFA can no longer provide the condensate density profile. Knowing the wavefunction of the condensate around these boundaries is very important to characterize, for instance, the actual kinetic energy [72, 73], the tunneling rate across a potential barrier [73, 289, 290], dynamics where the two components coexist [291], characterizing the transition between miscibility and immiscibility in trap systems [171], or in the case of immiscible TCBECs, the penetration of one component

into the other [168], which has been reported to be highly relevant when characterizing physics at the interface [165, 169, 292] and Wetting phase transitions [293, 294].

Several works have proposed new analytical approximations beyond the TFA for single component BECs [72, 73, 295–299], and for the two component case in the immiscible phase [165, 168, 292] as well as for the miscible, in spin-1 and spin-2 BECs [300]. In this chapter, we present a new analytical approach to study the density profile of a miscible TCBEC around the regions where the TFA fails, by deriving a universal equation that generalizes to two components the approach presented in [72, 73] for single component BECs. We also introduce a general procedure to solve the TFA of TCBECs in 1D, 2D and 3D, and we provide an analytical formula that determines the frontier between the different regimes of the system [154]. In addition, we have observed that the 1D and 3D TF approximated density profiles, within the spatially separated regime, can not be solved analytically, thus, we provide a formulation that reduces the complexity of the numerical inversion required in the solution [158, 288].

This chapter is organized in five sections. In Sec. 4.1, we present the time-independent two-component Gross–Pitaevskii equation (TCGPE) and the general form of the two-component TFA. In Sec. 4.2, we derive a universal equation governing the behavior of the density profile close to the different boundaries of the system. Section 4.3 is dedicated to the development of a procedure to solve the two-component TFA in the case of isotropic harmonic potentials in 1D, 2D and 3D. We compare our approach, for each dimensionality, with the numerical solution of the coupled Gross–Pitaevskii equation in Sec. 4.4, and present our conclusions in Sec. 4.5.

4.1 Ground-state of a two-component Bose–Einstein condensate

The ground state of a TCBEC at zero temperature within the mean-field approximation is well described by the time-independent TCGPE (see Sec. 2.3 for the time dependent TCGPE):

$$\left(-\frac{\hbar^2 \nabla^2}{2m_s} + V_s + \tilde{g}_s N_s |\Psi_s|^2 + \tilde{g}_{12} N_{3-s} |\Psi_{3-s}|^2 - \mu_s \right) \Psi_s = 0 \,, \qquad (4.1)$$

where $s = 1$ or 2 refers to each component of the BEC, whilst m_s, N_s, $V_s(\mathbf{r})$ and μ_s are the mass, number of atoms, external potential and chemical potential of the s component, respectively. The intra- and inter-species interaction coefficients are given by $\tilde{g}_s$ and $\tilde{g}_{12}$, respectively. In this chapter we consider repulsive intra-species interactions for both components, i.e., $\tilde{g}_s > 0$. For simplicity, we also assume that the TCBEC under consideration is formed by atoms of the same species in two different spin states [146–153]. This means that we can set $m_1 = m_2 = m$. Similarly, we consider equal trapping potentials $V_1(\mathbf{r}) = V_2(\mathbf{r}) = V(\mathbf{r})$, which in our case will be isotropic and harmonic. Nevertheless, our results can be straightforwardly generalized for cases with $m_1 \neq m_2$

and for $V_1(\mathbf{r}) \neq V_2(\mathbf{r})$. At this stage it is useful to redefine the interaction coefficients as $g_s = \tilde{g}_s N_s$ and $g_{12} = \tilde{g}_{12}\sqrt{N_1 N_2}$, obtaining a TCGPE of the form:

$$\left(-\frac{\hbar^2 \nabla^2}{2m} + V + g_s|\Psi_s|^2 + g_{12}\Pi^{s-3/2}|\Psi_{3-s}|^2 - \mu_s\right)\Psi_s = 0 , \qquad (4.2)$$

with $\Pi = N_1/N_2$.

By considering the TF limit, which neglects the kinetic energy terms ($\nabla^2\Psi_s = 0$) when compared with the nonlinear interaction terms, we are able to write down density profiles for either component. Adopting this limit the TCGPE, Eq. (4.2), become:

$$\left(V + g_s n_s + g_{12}\Pi^{s-3/2}n_{3-s} - \mu_s\right)\Psi_s = 0 , \qquad (4.3)$$

where we define $n_s(\mathbf{r}) = |\Psi_s(\mathbf{r})|^2$ for $s = 1$ and 2. Then, by solving the two coupled equations (Eq. (4.3)), one obtains the general form of the TF density profile for each component in the region where both components coexist, i.e. $n_s \neq 0$, for both values of s:

$$n_s(\mathbf{r}) = \frac{(g_{12}\Pi^{s-3/2} - g_{3-s})V(\mathbf{r}) + \mu_s g_{3-s} - \mu_{3-s}g_{12}\Pi^{s-3/2}}{g_1 g_2 - g_{12}^2}. \qquad (4.4)$$

Note that in order to have positive-definite solutions within the TFA the denominator in Eq. (4.4), $g_1 g_2 - g_{12}^2$, must be positive [301]. A system fulfilling this condition is commonly said to be in the miscible phase, otherwise it is in the immiscible phase (see Sec. 2.3). Throughout all this chapter, we will only consider intra- and inter-species interaction coefficients such that the system remains miscible.

In the regions where one component is absent ($n_s = 0$ for $s = 1$ or 2), the density profile of the other component, within the TFA, reads:

$$n_s(\mathbf{r}) = \frac{\mu_s - V(\mathbf{r})}{g_s}. \qquad (4.5)$$

4.1.1 Boundaries within the Thomas–Fermi approximation

In a TCBEC, the external potential and the interaction parameters determine the density distributions of the two components. In the following, we consider an isotropic harmonic potential $V(\mathbf{r}) = V(r) = m\omega_r^2 r^2/2$, where ω_r is the associated angular frequency. With such a potential we can observe two different regimes: (i) the coexisting regime, where one of the components occurs only in coexistence with the other Fig. 4.1(a,b); and (ii) the spatially separated regime where both components occur partly in coexistence with each other and partly in isolation Fig. 4.1(c). In general, we will denote the component with largest support (meaning the component with the largest spatial extent) with the subscript s. Within the TFA, we can distinguish two cases, when $g_{3-s} > g_{12}\Pi^{s-3/2}$ (equivalently $\tilde{g}_{3-s} > \tilde{g}_{12}$) in which case both components have their density maxima at the center of the trap Fig. 4.1(a), or otherwise, when $g_{3-s} < g_{12}\Pi^{s-3/2}$ in which case component $3 - s$ has its maximum of density at

the center of the trap while component s has it at a certain distance from the center Fig. 4.1(b,c). One can then note that if $n_s(0) > 0 \ (= 0)$ we are in the coexisting regime Fig. 4.1(a,b) (spatially separated regime Fig. 4.1(c)). The condition separating these two regimes is derived in Sec. 4.3.

The Thomas–Fermi limit, as introduced above, can provide us with a handle on the relative extent of each component. As such, we define the TF radii R_s, R_{3-s} and $\tilde{R}_s$ of a TCBEC trapped in an external harmonic potential by imposing $n_s(R_s) = 0$,
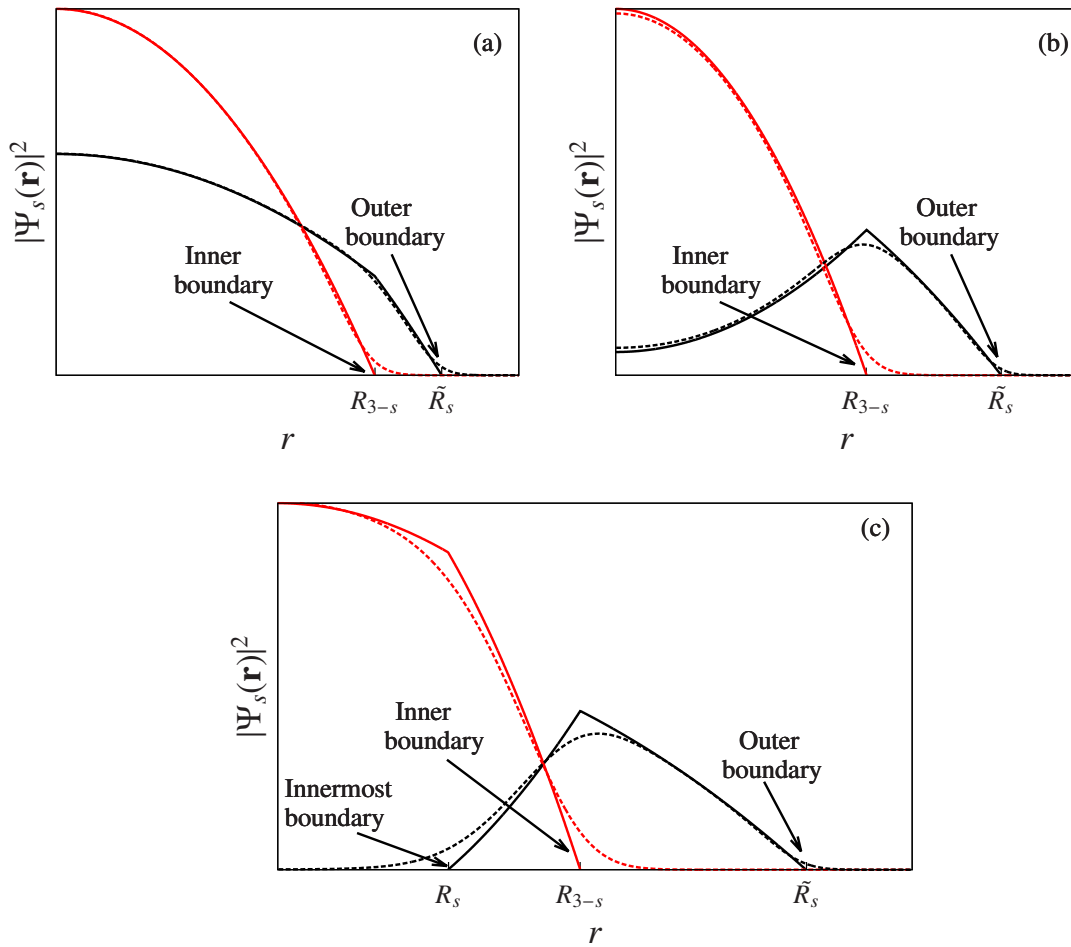

Figure 4.1: Different density distributions obtained within the TFA (solid lines) from Eqs. (4.4) and (4.5) and by numerically integrating (dotted lines) the TCGPE, Eq. (4.2), for the coexisting (a,b), and spatially separated (c) regimes. The different boundaries obtained in the TFA, Eqs. (4.6), are highlighted. In this plot we assume $g_s > g_{3-s}$ with $\Pi = 1$.

$n_s(R_{3-s}) = 0$ in Eqs. (4.4) and $n_s(\tilde{R}_s) = 0$ in Eq. (4.5), respectively:

$$R_s^2 = \frac{2}{m\omega_r^2} \frac{g_{12}\Pi^{s-3/2}\mu_{3-s} - g_{3-s}\mu_s}{g_{12}\Pi^{s-3/2} - g_{3-s}}, \tag{4.6a}$$

$$R_{3-s}^2 = \frac{2}{m\omega_r^2} \frac{g_{12}\mu_s - g_s\Pi^{s-3/2}\mu_{3-s}}{g_{12} - g_s\Pi^{s-3/2}}, \tag{4.6b}$$

$$\tilde{R}_s^2 = \frac{2}{m\omega_r^2}\mu_s. \tag{4.6c}$$

In Fig. 4.1 we plot the density profiles of the TCBEC within the TFA and indicate the three boundaries given in Eq. (4.6); the outer boundary $(\tilde{R}_s)$ that gives the maximum extent of the BEC, and the inner (R_{3-s}) and innermost (R_s) boundaries delimiting the regions where the two components coexist. Note that the innermost boundary appears only when $n_s(0) = 0$ (i.e. R_s is only defined when the system is in the spatially separated regime). Figure 4.1 also shows the numerical solution of the TCGPE, Eq. (4.2), in all the discussed cases, demonstrating that the TF approach cannot accurately describe the density profiles close to the boundaries. Next section is devoted to develop an analytical approach beyond the TFA and, thus, enabling an improvement on the approximated analytical profiles close to the boundaries.

4.2 Universal equation

In this section, we derive a universal equation that describes the density profile of a TCBEC around the outer, inner, and innermost boundaries, generalizing to TCBECs the method developed in [73] for the single component case. This generalization will require additional approximations for the inner and innermost boundaries, beyond those for the one component case. Note that in all the expressions shown in this section the subscript s refers to the component with largest support.

4.2.1 Outer boundary

First we focus on the outer boundary, $\tilde{R}_s$ (present in both coexisting and spatially separated regimes), where TCBECs behave effectively as single component BECs do. Therefore, we can follow the lines of [73] where the analytical description of the outer boundary is obtained by linearizing the harmonic potential around $\tilde{R}_s$:

$$V(r) \simeq V(\tilde{R}_s) + m\omega_r^2\tilde{R}_s(r - \tilde{R}_s) + O((r - \tilde{R}_s)^2). \tag{4.7}$$

We then introduce this linearization into Eq. (4.2) with $\Psi_{3-s} = 0$, obtaining:

$$\left[-\frac{\hbar^2}{2m}\frac{\partial^2}{\partial r^2} + m\omega_r^2\tilde{R}_s(r - \tilde{R}_s) + g_s|\Psi_s|^2 \right]\Psi_s = 0, \tag{4.8}$$

where we have used that $\mu_s = V(\tilde{R}_s)$ (see Eq. (4.5)), and we have only kept the second derivative term of the radial part of the Laplacian, i.e., in two (three) dimensions we

impose $r^{-1}\partial\Psi/\partial r \ll \partial^2\Psi/\partial r^2$ $(2r^{-1}\partial\Psi/\partial r \ll \partial^2\Psi/\partial r^2)$. This approximation applies for values of $\tilde{R}_s$ much larger than the thickness of the boundary given by Eq. (4.10), as discussed in [73].

Finally, by defining the dimensionless variable

$$\tilde{\xi}_s = \frac{r - \tilde{R}_s}{\tilde{d}_s}, \tag{4.9}$$

with

$$\tilde{d}_s = \left(\frac{\hbar^2}{2m^2\omega_r^2\tilde{R}_s}\right)^{1/3}, \tag{4.10}$$

and the dimensionless wavefunction ϕ_s through

$$\Psi_s(r) = \frac{\hbar}{\tilde{d}_s\sqrt{2mg_s}}\phi_s(\tilde{\xi}_s), \tag{4.11}$$

we obtain the following universal equation describing the density profile of the outer boundary [73]:

$$\phi_s'' - (\tilde{\xi}_s + \phi_s^2)\phi_s = 0. \tag{4.12}$$

4.2.2   Inner and innermost boundaries

Around the inner and innermost boundaries, R_s and R_{3-s}, respectively [see Fig. 4.1(c)], both components coexist, and we must therefore consider the full coupled Eqs. (4.2). Thus, in order to obtain the density profile around the s component boundary (the innermost boundary) we linearize the potential around R_s:

$$V(r) \simeq V(R_s) + m\omega_r^2 R_s(r - R_s) + O((r - R_s)^2). \tag{4.13}$$

Introducing this linearization into Eqs. (4.2), one obtains the following two coupled equations for the s and $3 - s$ component, respectively:

$$\left[-\frac{\hbar^2}{2m}\frac{\partial^2}{\partial r^2} + \frac{g_{12}\Pi^{s-3/2}(\mu_{3-s} - \mu_s)}{g_{12}\Pi^{s-3/2} - g_{3-s}} + m\omega_r^2 R_s(r - R_s) + g_s|\Psi_s|^2 + g_{12}\Pi^{s-3/2}|\Psi_{3-s}|^2\right]\Psi_s = 0\,, \tag{4.14a}$$

$$\left[-\frac{\hbar^2}{2m}\frac{\partial^2}{\partial r^2} + \frac{g_{3-s}(\mu_{3-s} - \mu_s)}{g_{12}\Pi^{s-3/2} - g_{3-s}} + m\omega_r^2 R_s(r - R_s) + g_{3-s}|\Psi_{3-s}|^2 + g_{12}\Pi^{3/2-s}|\Psi_s|^2\right]\Psi_{3-s} = 0\,, \tag{4.14b}$$

where the term $V(R_s)$ in both equations has been rewritten using the expression (4.6a). As for the outer boundary, we only keep the second derivative term of the Laplacian. The influence of the first derivative is much less than that of the second derivative in the limit of large R_s. Thus, this approximation will not be valid in the cases for which R_s is close to the origin. Specifically, R_s must be larger than the thickness of the boundary Eq. (4.17) [73], or, in other words, the relationship between the nonlinear parameters

has to be such that the system is far from the crossover condition between the coexisting and spatially separated regimes, for which $R_s = 0$ (the analytical expression is shown in Sec. 4.3).

In order to solve the two coupled Eqs. (4.14) for the s component, we use the TFA for the $3 - s$ component by assuming that, close to R_s, the density of component $3 - s$ is large enough to ignore the kinetic energy terms, i.e., we impose $\partial^2 \Psi_{3-s}/\partial r^2 = 0$ in Eq. (4.14b). Two limiting cases where this assumption cannot be applied exist: (i) when $R_{3-s} - R_s = O(\epsilon)$, which occurs when $g_{12} \to \sqrt{g_1 g_2}$, because the TF approach is at the limit of its applicability and (ii) when $\tilde{R}_s - R_{3-s} = O(\epsilon)$, which occurs for $g_{12} \to 0$, because there is no interaction between components and the system reduces to two noninteracting BECs.

Then, by combining the TF form of Eq. (4.14b) with Eq. (4.14a), one obtains:

$$\left[-\frac{\hbar^2}{2m} \frac{\partial^2}{\partial r^2} + m\omega_r^2 R_s \left(1 - \frac{g_{12} \Pi^{s-3/2}}{g_{3-s}} \right)(r - R_s) + \left(g_s - \frac{g_{12}^2}{g_{3-s}} \right) |\Psi_s|^2 \right] \Psi_s = 0 . \quad (4.15)$$

By following a similar procedure, the equivalent equation for the $3 - s$ component around R_{3-s} at which $n_{3-s}(R_{3-s}) = 0$ can be found. The resulting equation has the same form as Eq. (4.15) but with $3 - s$ and s exchanged. In order to solve the innermost and inner boundaries we first define the dimensionless variable:

$$\xi_s = \pm \frac{r - R_s}{d_s}, \quad (4.16)$$

with d_s given by

$$d_s = \left[\frac{\hbar^2}{\pm 2m^2 \omega_r^2 R_s \left(1 - g_{12} \Pi^{s-3/2}/g_{3-s} \right)} \right]^{1/3}, \quad (4.17)$$

and the dimensionless wavefunction ϕ_s defined through

$$\Psi_s(r) = \frac{\hbar}{d_s \sqrt{2m \left(g_s - g_{12}^2/g_{3-s} \right)}} \phi_s(\xi_s). \quad (4.18)$$

In Eqs. (4.16) and (4.17) the $+$ $(-)$ sign applies for the inner (innermost) boundary, and for the inner boundary s has to be interchanged by $3 - s$ and $3 - s$ by s.

Finally, one obtains the same universal equation derived in Sec. 4.2.1 (Eq. (4.12)) for both boundaries:

$$\phi_s'' - (\xi_s + \phi_s^2)\phi_s = 0, \quad (4.19)$$

where the s $(3 - s)$ applies for the innermost (inner) boundary.

Summarizing, in this section we have obtained the universal Eqs. (4.12) and (4.19) that describe the density profiles at the boundaries of a TCBEC trapped in a harmonic potential. Note that we obtain the same universal equation for the three boundaries, however, they require different transformations, Eqs. (4.9) and (4.11) for the outer boundary and Eqs. (4.16) and (4.18) for the inner and innermost boundaries, in order to retrieve the actual wavefunction at each boundary.

4.2.3   Universal equation solution

One can recognize Eqs. (4.12) and (4.19) in the literature [302, 303] as being a Painlevé type-II equation, which for positive defined solutions with no divergences or sinusoidal behaviors has a Hastings–McLeod (HM) solution[1] [302] with the following asymptotics:

$$\phi_{\text{HM}}(\xi) \sim \begin{cases} \sqrt{2}\text{Ai}(\xi) & \text{for } \xi \to +\infty, \\ \sqrt{-\xi} & \text{for } \xi \to -\infty, \end{cases} \tag{4.20}$$

where $\text{Ai}(\xi)$ is the Airy function.

Here, we are interested in the $\xi \to +\infty$ limit, where the density is small and the TF approach is not applicable. Equation (4.20) shows that, for $\xi \to +\infty$ the wavefunction takes the form of $\sqrt{2}\text{Ai}(\xi)$, whose asymptotic formula reads:

$$\phi(\xi \to +\infty) \simeq \sqrt{2}\text{Ai}(\xi) \simeq \frac{1}{\sqrt{2\pi}\xi^{1/4}} e^{-2\xi^{3/2}/3}. \tag{4.21}$$
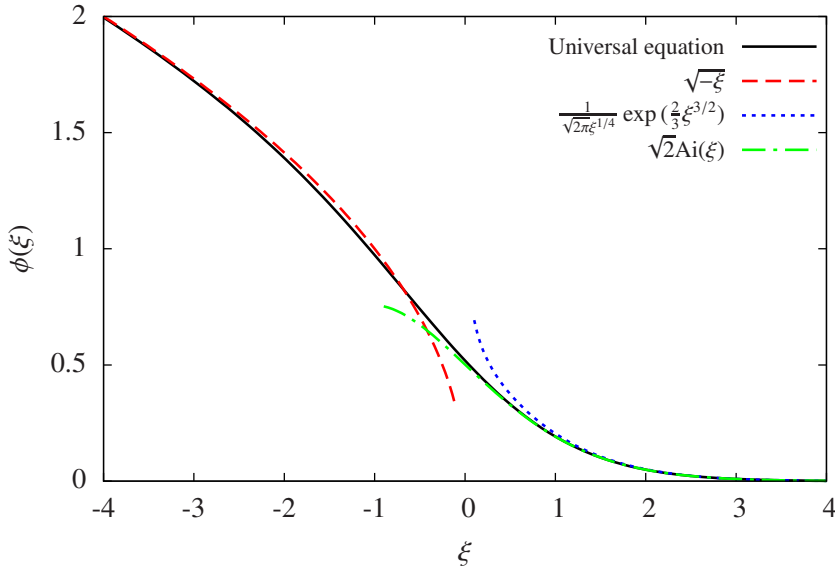
Figure 4.2: Numerical solution of the universal equation, Eq. (4.12) and Eq. (4.19), (black solid line), and the two asymptotic behaviors given by the Hastings–McLeod solution Eq. (4.20)): the Airy function (green dotted dashed line), and $\sqrt{-\xi}$ (red dashed line). We also plot the asymptotic behavior of the Airy function Eq. (4.21) for $\xi \to +\infty$ (blue dotted line).

---

[1]Note that the Painlevé type-II equation has a factor two in front of the nonlinear term that makes the prefactor in front of the Hastings–McLeod solution equal to 1 instead of $\sqrt{2}$.

Figure 4.2 shows the asymptotic forms of the HM solution, Eq. (4.20), and the numerical solution of Eq. (4.12) or Eq. (4.19) for comparison. We also plot the asymptotic behavior of the Airy function, Eq. (4.21). Even though the approximation given by Eq. (4.21), is obtained at $\xi \rightarrow +\infty$, the two functions coincide even for low values of ξ, which makes this asymptotic approximation very useful as an analytical expression to describe the universal equation for $\xi > 0$. It remains for us to find appropriate expressions for the TF boundaries in order to complete the transformations to retrieve the actual wavefunctions near each boundary.

4.3 Thomas–Fermi solutions

In this section, we present a general procedure to obtain the TF radii and chemical potentials within the TFA of a TCBEC trapped in an isotropic harmonic potential in 1D, 2D and 3D. We study both the coexisting and the spatially separated regimes, and we determine the frontier between them for each dimensionality.

The TF solution, in either the coexisting or in the spatially separated regime, can be found by following three general steps (a similar procedure was presented in [154], extending to two components the single component case discussed in Sec. 2.1.2): (i) normalization of the density using the proper limits of integration, (ii) isolation of the chemical potential of each of the components, μ_s and μ_{3-s}, as a function of the parameters of the system from the normalization integrals, and (iii) insertion of μ_s and μ_{3-s} into Eq. (4.4) (Eq. (4.5)) for the coexisting (non-coexisting) region, to obtain the density profile.

In some cases these steps can be laborious, and in particular step (iii) may not be possible to do analytically. Specifically, we have found that in the 1D and 3D cases the chemical potentials cannot be inverted analytically within the spatially separated regime. Thus, here we show how to reduce the two coupled algebraic equations to a single equation, reducing the complexity of the numerical problem [158, 288]. In all other cases, fully analytical expressions can be found.

4.3.1   Coexisting regime

The coexisting regime can be solved in a fully analytical fashion for all three dimensionalities. In this case, the normalization conditions for the s and $3 - s$ components read:

$$\int\limits_0^{R_{3-s}} \left(\zeta_s + \eta_s r^2 \right) d^D r + \int\limits_{R_{3-s}}^{\tilde{R}_s} \left(\lambda_s + \kappa_s r^2 \right) d^D r = 1, \tag{4.22a}$$

$$\int\limits_0^{R_{3-s}} \left(\zeta_{3-s} + \eta_{3-s} r^2 \right) d^D r = 1, \tag{4.22b}$$

where $D = 1$, 2 or 3 depending on the dimensionality. The $d^D r$ differential represents the volume element for each case: $d^1 r = 2dr$, $d^2 r = 2\pi r dr$, $d^3 r = 4\pi r^2 dr$, (note that in the 1D case we add a factor 2 due to the fact that r should go from $-\infty$ to ∞). We assume cylindrically and spherically isotropic configurations in the 2D and 3D harmonic potentials, respectively, and λ_s, κ_s, ζ_s and η_s are given by:

$$\lambda_s = \frac{\mu_s}{g_s}, \qquad \zeta_s = \frac{\mu_s g_{3-s} - \mu_{3-s} g_{12} \Pi^{s-3/2}}{g_1 g_2 - g_{12}^2}, \tag{4.23}$$
$$\kappa_s = -\frac{m\omega_r^2}{2g_s}, \qquad \eta_s = \frac{m\omega_r^2}{2} \frac{g_{12} \Pi^{s-3/2} - g_{3-s}}{g_1 g_2 - g_{12}^2}.$$

By carrying out the integrations in Eq. (4.22a) and Eq. (4.22b) we reach:

$$\Omega_D R_{3-s}^{D+2} + \epsilon_D \tilde{R}_s^{D+2} = 1, \tag{4.24a}$$

$$\beta_D R_{3-s}^{D+2} = 1, \tag{4.24b}$$

where Ω_D, ϵ_D and β_D read:

$$\beta_D = -\Delta_D \frac{2m\omega_r^2}{3} \frac{g_{12} \Pi^{3/2-s} - g_s}{g_1 g_2 - g_{12}^2},$$

$$\Omega_D = \Delta_D \frac{2m\omega_r^2}{3} \frac{g_{12}}{g_s} \left(\frac{g_{12} - g_s \Pi^{s-3/2}}{g_1 g_2 - g_{12}^2} \right), \tag{4.25}$$

$$\epsilon_D = \Delta_D \frac{2m\omega_r^2}{3} \frac{1}{g_s},$$

and where the scaling factors

$$\Delta_1 = 1, \qquad \Delta_2 = \frac{3\pi}{8}, \qquad \Delta_3 = \frac{6\pi}{15}, \tag{4.26}$$

account for the different dimensionalities. Note that β_D is related to Ω_D through $\beta_D = -(g_s/g_{12}\Pi^{s-3/2})\Omega_D$.

Then, using Eqs. (4.24) and the definitions of Eqs. (4.6) we obtain:

$$\mu_s = \frac{m\omega_r^2}{2\epsilon_D^{2/(D+2)}} \left(1 - \Omega_D/\beta_D\right)^{2/(D+2)}, \tag{4.27a}$$

$$\mu_{3-s} = \frac{g_{12}\mu_s}{\Pi^{s-3/2}g_s} + \frac{m\omega_r^2}{2} \left(\frac{g_s - \Pi^{3/2-s}g_{12}}{g_s}\right) \beta_D^{-2/(D+2)}. \tag{4.27b}$$

Finally, by introducing these two chemical potentials into Eq. (4.4) and Eq. (4.5) one finds the solution of the TF density profile of a TCBEC in the coexisting regime.

The analytical expression, within the TFA, of the frontier between the coexisting and spatially separated regimes, can be found by using the fully analytical expression of the density profile obtained by inserting Eq. (4.27a) and Eq. (4.27b) into Eq. (4.4) and setting $n_s(0) = 0$:

$$g_{3-s} = \frac{g_{12}^2}{g_s} - g_{12}(g_{12} - \Pi^{s-3/2}g_s) \left(\frac{g_s + \Pi^{s-3/2}g_{12}}{g_s^{-D/2}\Pi^{s-3/2}g_{12}}\right)^{-2/D}. \tag{4.28}$$

Note that Eq. (4.28) gives the condition that separates coexisting, Fig. 4.1(a,b), and spatially separated, Fig. 4.1(c), regimes as a function only of the nonlinear parameters and ratio of the number of particles. All the calculations shown in this subsection are valid for $D = 1$, 2 and 3.

4.3.2 Spatially separated regime

As mentioned previously, the full solution of the two chemical potentials in the spatially separated regime cannot be found analytically in the one and three dimensional cases. Here we present a procedure to reduce the complexity of this numerical problem. We start by using the normalization conditions for the s and $3 - s$ components, respectively:

$$\int\limits_{R_s}^{R_{3-s}} \left(\zeta_s + \eta_s r^2\right) d^D r + \int\limits_{R_{3-s}}^{\tilde{R}_s} \left(\lambda_s + \kappa_s r^2\right) d^D r = 1, \tag{4.29a}$$

$$\int\limits_{0}^{R_s} \left(\lambda_{3-s} + \kappa_{3-s} r^2\right) d^D r + \int\limits_{R_s}^{R_{3-s}} \left(\zeta_{3-s} + \eta_{3-s} r^2\right) d^D r = 1, \tag{4.29b}$$

where λ_s, κ_s, ζ_s and η_s are defined in Eq. (4.23). After integrating Eqs. (4.29) and rearranging the terms, we obtain the two coupled equations:

$$\gamma_D R_s^{D+2} + \Omega_D R_{3-s}^{D+2} + \epsilon_D \tilde{R}_s^{D+2} = 1, \tag{4.30a}$$

$$\alpha_D R_s^{D+2} + \beta_D R_{3-s}^{D+2} = 1, \tag{4.30b}$$

where α_D and γ_D read:

$$\alpha_D = -\Delta_D \frac{2m\omega_r^2}{3} \frac{g_{12}}{g_{3-s}} \left(\frac{g_{12} - g_{3-s}\Pi^{3/2-s}}{g_1 g_2 - g_{12}^2} \right),$$

$$\gamma_D = \Delta_D \frac{2m\omega_r^2}{3} \frac{g_{12}\Pi^{s-3/2} - g_{3-s}}{g_1 g_2 - g_{12}^2}, \tag{4.31}$$

with the scaling factors accounting for the different dimensionalities given in Eq. (4.26), and where Ω_D, ϵ_D and β_D are defined as in Eq. (4.25).

In the 1D and 3D cases the chemical potentials of both components cannot be obtained analytically from Eqs. (4.30), therefore in order to reduce the two coupled equations into a single equation we rewrite R_s^{D+2} and R_{3-s}^{D+2} from Eq. (4.30) as:

$$R_s^{D+2} = \frac{g_{3-s}}{(g_1 g_2 - g_{12}^2)\gamma_D} \left(g_s N' + g_{12}\Pi^{s-3/2} \right), \tag{4.32a}$$

$$R_{3-s}^{D+2} = \frac{g_{12}}{(g_{12}^2 - g_1 g_2)\Omega_D} \left(g_{12} N' + g_{3-s}\Pi^{s-3/2} \right), \tag{4.32b}$$

where $N' = 1 - \epsilon_D \tilde{R}_s^{D+2}$. Introducing Eqs. (4.32) into the relation between the TF radii obtained from Eqs. (4.6) yields

$$\tilde{R}_s^2 = \frac{g_s(g_{3-s} - g_{12}\Pi^{s-3/2})}{g_1 g_2 - g_{12}^2} R_s^2 + \frac{g_{12}(g_s\Pi^{s-3/2} - g_{12})}{g_1 g_2 - g_{12}^2} R_{3-s}^2, \tag{4.33}$$

and one obtains a single equation that only depends on μ_s and on the parameters of the system. This equation has two roots that need to be inverted numerically in order to find μ_s (the root power depends on the dimensionality). By using the expression for R_{3-s} from Eqs. (4.32a) and (4.6a) we find an analytical formulation for μ_{3-s} as a function of μ_s. Once we have the two chemical potentials, we introduce them into the densities [Eqs. (4.4) and (4.5)], obtaining the TF solution of a TCBEC in D dimensions in the spatially separated regime.

In the 2D case, however, Eqs. (4.30) can be solved analytically using the definitions of α, β, γ, Ω and ϵ from Eq. (4.25), Eq. (4.26) and Eq. (4.31) for $D = 2$. In this case, using the expressions of the TF radii from Eq. (4.6) we obtain:

$$\mu_{3-s}^{(2D)} = \sqrt{\frac{m\omega_r^2 g_{3-s}(\Pi^{3-2s} + 1)}{\pi}}, \tag{4.34a}$$

$$\mu_s^{(2D)} = \mu_{3-s} + \sqrt{\frac{m\omega_r^2(\Pi^{s-3/2}g_s - g_{12})(\Pi^{s-3/2}g_{12} - g_{3-s})}{\pi\Pi^{2s-3}g_{12}}}, \tag{4.34b}$$

and by substituting into Eq. (4.4) and Eq. (4.5) we get the density profiles of the TCBEC in 2D in the spatially separated regime.

Figure 4.3: Comparison between the results of the density profiles obtained through the universal equation, Eqs. (4.12) and (4.19), the TFA (Sec. 4.3) and the numerical solution of the TCGPE, Eq. (4.2) for a 1D TCBEC. In (a) we show the TF density profile (blue dotted line) and the numerical solution of the TCGPE (solid lines) of a TCBEC in the spatially separated regime for the 1D case and for two different values of g_2. We also plot a magnification around R_1 (b), R_2 (c) and $\tilde{R}_1$ (d) where we include the asymptotic approximation of the universal equation $\sqrt{2}\mathrm{Ai}(r)$ (dotted-dashed line) derived in Sec. 4.2. The parameter values used are: $\chi = 0.985$, $g_2 = 200$ (black lines) and $g_2 = 1000$ (red/gray lines). Note that the magnifications only include the component under study. For a complete description of the dimensionless parameters and scalings see the text.
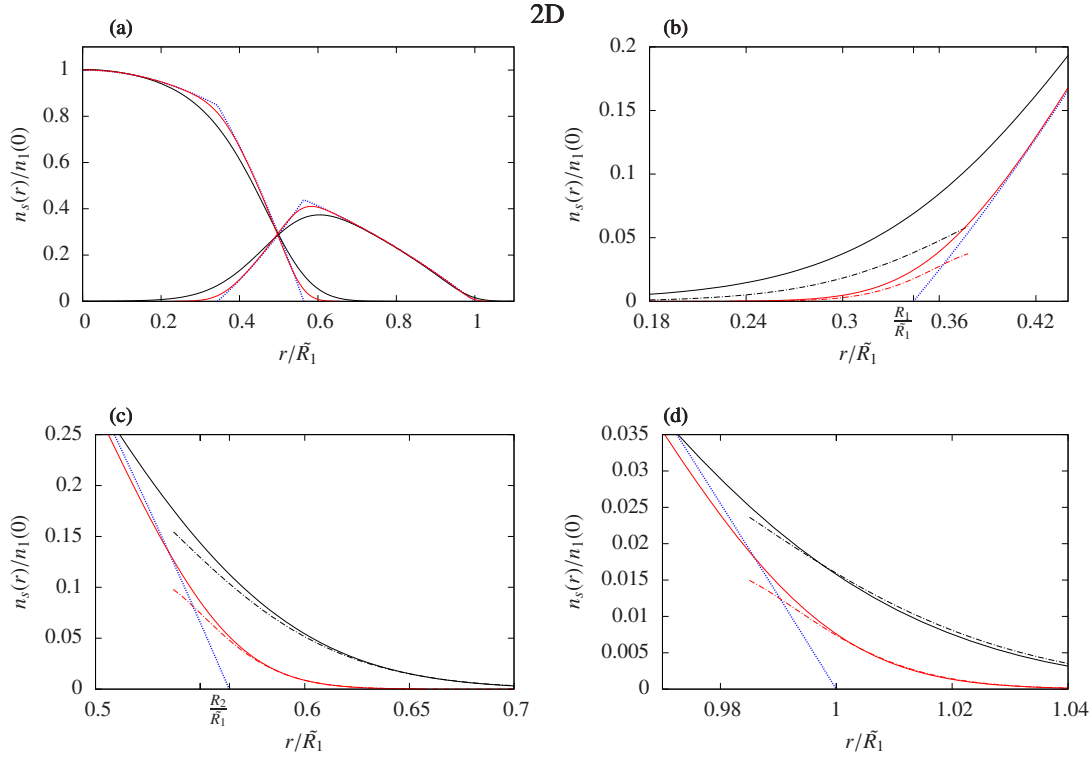
Figure 4.4: Comparison between the results of the density profiles obtained through the universal equation, Eqs. (4.12) and (4.19), the TFA (Sec. 4.3) and the numerical solution of the TCGPE, Eq. (4.2) for a 2D TCBEC. In (a) we show the TF density profile (blue dotted line) and the numerical solution of the TCGPE (solid lines) of a TCBEC in the spatially separated regime for the 2D case and for two different values of g_2. We also plot a magnification around R_1 (b), R_2 (c) and $\tilde{R}_1$ (d) where we include the asymptotic approximation of the universal equation $\sqrt{2}\text{Ai}(r)$ (dotted-dashed line) derived in Sec. 4.2. The parameter values used are: $\chi = 0.9$, $g_2 = 1000$ (black lines) and $g_2 = 10000$ (red/gray lines). Note that the magnifications only include the component under study. For a complete description of the dimensionless parameters and scalings see the text.
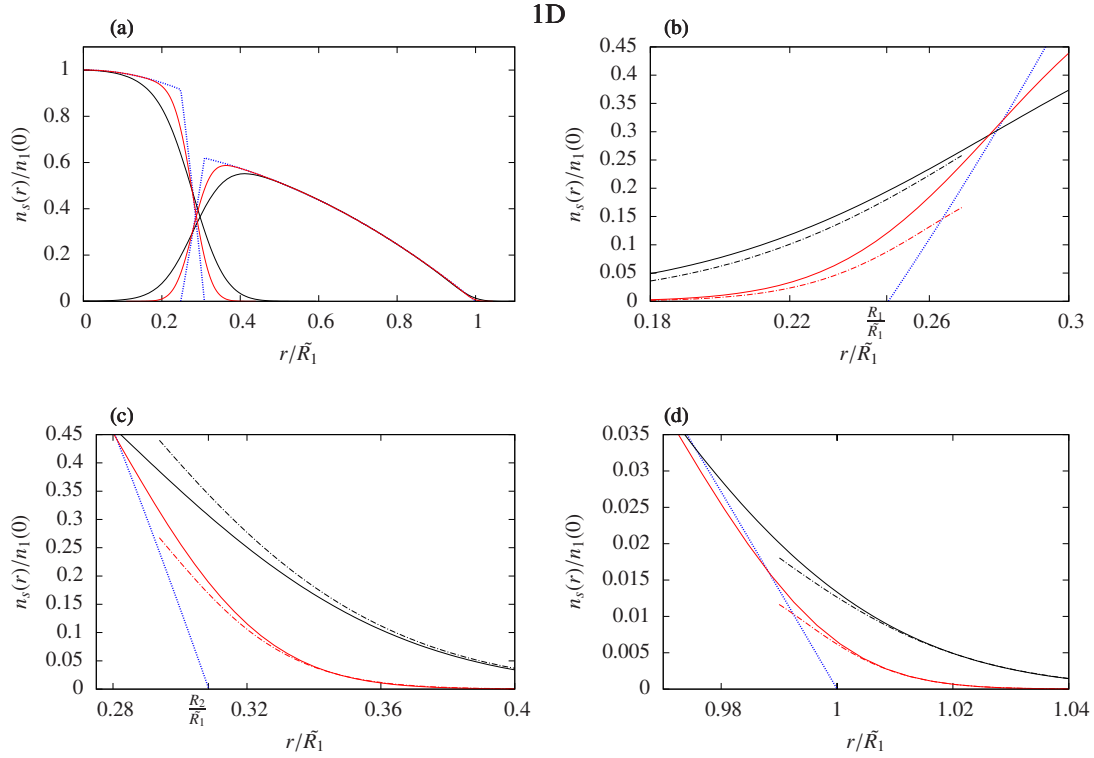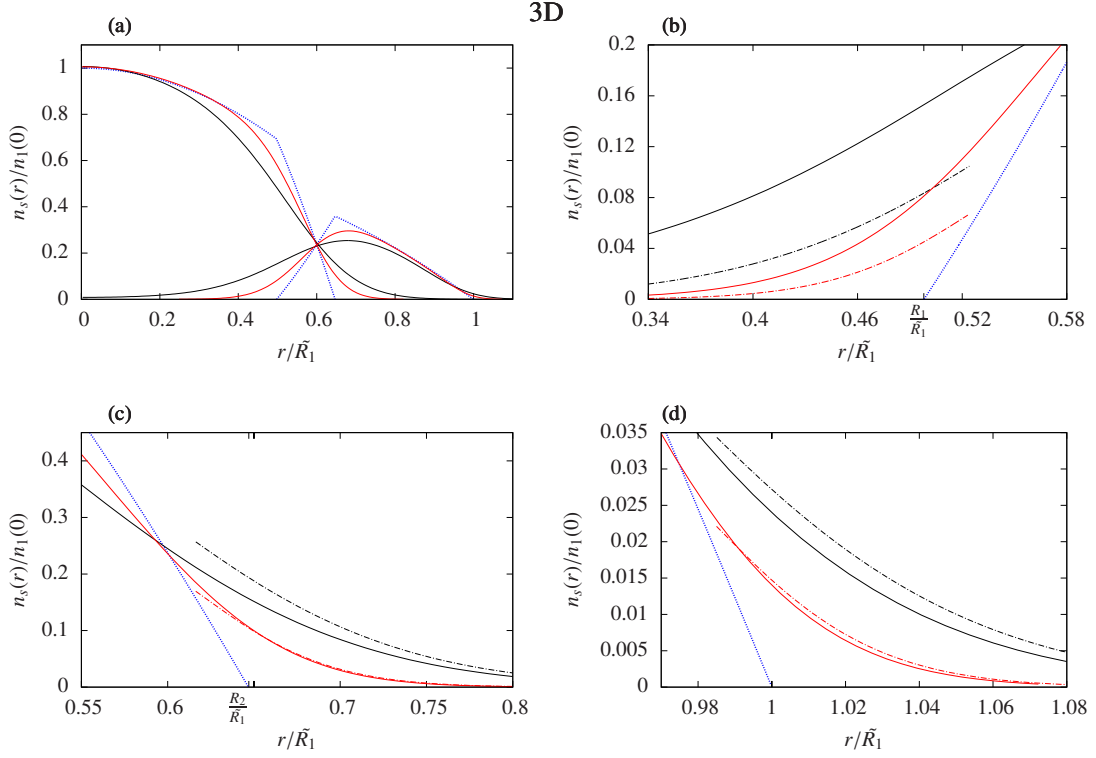
Figure 4.5: Comparison between the results of the density profiles obtained through the universal equation, Eqs. (4.12) and (4.19), the TFA (Sec. 4.3) and the numerical solution of the TCGPE, Eq. (4.2) for a 3D TCBEC. In (a) we show the TF density profile (blue dotted line) and the numerical solution of the TCGPE (solid lines) of a TCBEC in the spatially separated regime for the 3D case and for two different values of g_2. We also plot a magnification around R_1 (b), R_2 (c) and $\tilde{R}_1$ (d) where we include the asymptotic approximation of the universal equation $\sqrt{2}\mathrm{Ai}(r)$ (dotted-dashed line) derived in Sec. 4.2. The parameter values used are: $\chi = 0.9$, $g_2 = 1000$ (black lines) and $g_2 = 10000$ (red/gray lines). Note that the magnifications only include the component under study. For a complete description of the dimensionless parameters and scalings see the text.

4.4   Density profiles around the boundaries

In this section, we present the comparison between the density profiles in 1D, 2D and 3D of a TCBEC around the boundaries defined in Eq. (4.6) obtained: (i) within the TFA (Sec. 4.3), (ii) using the universal equation derived in Sec. 4.2 and (iii) by numerically integrating the TCGPE (Eq. (4.2)) for the spatially separated regime. To reduce the parameter phase space we consider the same number of atoms for both components, i.e., $\Pi = 1$, $g_{12} = \sqrt{\chi g_1 g_2}$ and $g_s = 2g_{3-s}$, in such a way that the parameter χ determines the ratio between the different TF radii (Eq. (4.6)) and g_{3-s} determines the strength of the nonlinear interactions. In addition, we rescale the densities of both components to the maximum value of the density of the $3 - s$ component at the origin (considering the s component to be that with largest support) and the r coordinate to the maximum extension of the TCBEC ($\tilde{R}_s$). We also use harmonic oscillator units, which is equivalent to setting $\hbar = m = \omega_r = 1$. These settings allow us to compare the behavior, graphically, of the density profiles close to the boundaries for different values of the nonlinearity on the same axis scale.

In order to have some reference values of the strength of the considered nonlinear interactions (g_{3-s}) we compare our rescaled nonlinear parameters with typical experimental values. We consider a TCBEC of ^{87}Rb trapped in a harmonic potential with a radial trapping frequency $\omega_r = 2\pi \times 20$ Hz, transverse trapping frequency $\omega_\perp = 2\pi \times 150$ Hz (for the one and two dimensional cases) and $a_s = 100a_0$, with a_0 and a_s being the Bohr radius and the s-wave scattering length, respectively. In the 1D case, $g_{3-s} \simeq 200$ corresponds to a BEC with $N_s = N_{3-s} \simeq 1 \times 10^4$ particles, while in the 2D and 3D cases, $g_{3-s} = 1000$ corresponds to an approximate value of $N_s = N_{3-s} \simeq 5 \times 10^4$ particles.

Figures 4.3, 4.4 and 4.5 show the density profile of a 1D, 2D and 3D TCBEC trapped in an isotropic harmonic potential in the spatially separated regime using the TFA (Eqs. (4.30)–(4.33)), the universal equation (Eqs. (4.12) and (4.19)) and the results of the TCGPE (Eq. (4.2)) for different nonlinearities. Note that we have fixed $s = 1$ for the component with largest support.

We observe that in 1D (Fig. 4.3) the asymptotic behavior of the universal equation at the different boundaries is in excellent agreement with the numerical solution of the TCGPE, even for values of g_2 corresponding to a relatively small number of particles in a typical experimental TCBEC.

In 2D (Fig. 4.4) we can see that the universal equation around the boundaries (Sec. 4.2) gives a good insight of the numerical solution of the TCGPE in a fully analytical way for $g_2 = 1 \times 10^4$. However, for relatively small nonlinearities ($g_2 \sim 1000$), the universal equation close to the innermost boundary cannot describe the density of the TCBEC, as discussed in Sec. 4.2.

In 3D (Fig. 4.5) we see that the outer and inner boundaries are in very good agreement for both nonlinearities, showing that this approximation can be used to describe the density of a TCBEC around the boundaries provided that the conditions mentioned

in Sec. 4.2 are fulfilled. The universal equation close to the innermost boundary, on the other hand, hardly reproduces the density of the TCBEC for low values of g_2, however, the approximation appears to have broad validity for values of g_2 above 10000.

4.5   Conclusions

In this chapter, we have presented an analytical approximation to the ground state density profiles of a TCBEC trapped in an isotropic harmonic potential within the mean field approximation around the boundaries of each component, where the TFA is no longer valid. We have derived universal equations that provide a good estimation of the behavior of the density profile at the boundaries of each species, softening the sharp edges produced by the TFA. We have compared our analytical results with the numerically integrated TCGPE, obtaining an excellent agreement between them. The method we have proposed also offers the possibility to calculate analytically, as proposed in [72, 73] for single component systems, the kinetic energy of the system, tunneling between double well potentials and other possibilities such as calculating an equivalent *healing length* in a TCBEC in the miscible phase, similarly to the penetration depth defined in the immiscible phase by [168]. Moreover, this approach can be easily extended to different species (i.e. different masses), and also, due to its generality, the procedure may be extended to other trapping potentials.

We have also studied the TFA for 1D, 2D and 3D. We have shown that the coexisting regime can be treated analytically in all three cases. However, the spatially separated regime only has analytical solution in 2D. In 1D and 3D we can decrease the complexity of the numerical inversion required by reducing the resulting system of two coupled equations to a single one. Finally, within the TFA, we have determined, analytically, the frontier between the coexisting and spatially separated regimes.

Transport of ultracold atoms between concentric traps via spatial adiabatic passage

In this chapter, we study the transport of a single ultracold atom in cylindrically symmetric concentric potentials [74]. Specifically, we use 2D spatial adiabatic passage (SAP) techniques to obtain a robust and high fidelity loading from a harmonic trap to a ring potential and for the transport between two ring potentials using the matter-wave analogue of the rapid adiabatic passage (RAP) process [75]. The matter-wave analogue of the stimulated Raman adiabatic passage (STIRAP) [76, 304] in systems of three concentric rings is also investigated for the transport of localized ground states and of orbital angular momentum (OAM) states between the innermost and outermost rings. The dynamics of the RAP-like and STIRAP-like processes is described using few-state models (see Sec. 2.5), obtaining an excellent agreement with the numerical simulations of the corresponding 2D Schrödinger equation.

We focus on toroidal trapping potentials [92, 183, 185, 194, 211, 305–313] for ultracold atoms which are essential in many quantum metrology implementations, e.g., for matter-wave Sagnac interferometry [71, 314], and as elementary building blocks in the emerging field of Atomtronics [24, 315–319]. In fact, ring potentials constitute the simplest nontrivial closed-loop circuits and offer unique features to investigate, for instance, superfluidity and persistent currents [25, 320–326]. Angular momentum in such systems can be transferred to the atoms using either light [324] or by rotating a tunable weak link [25]. The latter has been one of the key elements that has opened the possibility to study matter-wave analogues of superconducting quantum interference devices (SQUIDs) [12–15, 327–329]. Recently, hysteresis, which is a basic ingredient in electronics, has been observed experimentally between quantized circulation states of a Bose–Einstein condensates (BEC) trapped in a ring [330].

In this context, the development of techniques allowing for a high fidelity and robust transport between ring potentials is a topical issue and it is the main purpose of this chapter, where we provide mechanisms to load, and transport ultracold atoms in ring potentials. SAP processes [59] have been proposed for the transport of single atoms [331–338], electrons [339], and BECs [340–343] between the outermost traps of in-line triple-well potentials. Moreover, 2D SAP processes for three tunnel-coupled harmonic wells in a triangular configuration have recently been discussed for matter-wave interferometry [344], and for the generation of atomic states carrying orbital angular momentum [220]. It is also worth to highlight that SAP has already been experimentally demonstrated for light beams propagating in three evanescently coupled optical waveguides [345–348], and recently discussed for the manipulation of sound propagation in sonic crystals [349].

Both SAP processes studied here rely on the ability to vary the frequencies and radii of the trapping potentials. For optically generated potentials, the frequency can be modified by varying the laser intensity that produces the potential [92, 194], and the radius of the ring can be changed dynamically using time-averaged adiabatic techniques [312, 313].

This chapter is structured as follows. The physical systems under investigation are introduced in Sec. 5.1. Section 5.2 is devoted to the transport of a single atom between two concentric cylindrically symmetric potentials by means of the matter-wave RAP technique, whereas Sec. 5.3 focuses on the transport of an atom between the innermost and outermost traps of a triple-ring potential through the matter-wave STIRAP technique. Section 5.4 presents the conclusions.

5.1   Concentric traps

We consider a single atom trapped in 2D cylindrically symmetric external potentials formed by different concentric combinations of harmonic and harmonic ring potentials as the ones shown in Fig. 5.1. Figure 5.1(a) corresponds to the total potential used to study the loading of an atom from a harmonic potential centered at the origin to a concentric harmonic ring potential. Figure 5.1(b) shows the system where we study the transport between two concentric ring potentials. In both cases we use the matter-wave analogue of the RAP process by varying the trapping frequency and the radius of the outer ring potential, which allow us to adjust the tunneling rate and energy bias in such a way that the atom adiabatically follows the ground states of the localized traps. In Fig. 5.1(c) we show a system of three concentric ring potentials in which the STIRAP-like protocol have been used to transport a single atom between the innermost and outermost rings. In particular, in the STIRAP protocol we keep the same radial trapping frequencies for the three harmonic rings and modify the rings separations in order to achieve the transport.

Using cylindrical coordinates (r, ϕ), the harmonic potential with trapping frequency
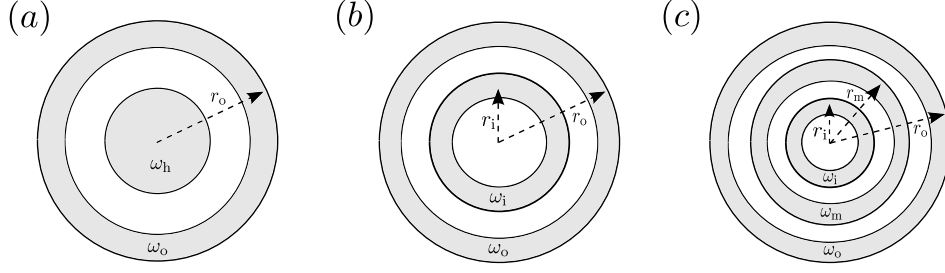
Figure 5.1: Sketch of the trapping geometries formed by the combination of concentric (a) harmonic and harmonic ring potentials; and (b) two and (c) three harmonic ring potentials. Transport will always take place from the innermost trap to the outermost one. The top row shows three-dimensional representations of the trapping potentials. The bottom row shows 2D schematics of the three configurations, with traps represented in gray, and including labels for trap frequencies and radii. ω_h is the radial trapping frequency of the harmonic potential; r_j and ω_j with $j = i, m, o$ are the radii and radial trapping frequencies of the inner, middle, and outer rings, respectively.

ω_h for an atom of mass m reads

$$V_h(r) = \frac{1}{2}m\omega_h^2 r^2, \tag{5.1}$$

and its ground state wavefunction is

$$\Psi_h(r) = \sqrt{\frac{m\omega_h}{\pi\hbar}} e^{-\frac{m\omega_h}{2\hbar}r^2}. \tag{5.2}$$

The harmonic ring potentials of trapping frequencies ω_j and radii r_j are given by

$$V_{r,j}(r) = \frac{1}{2}m\omega_j^2(r - r_j)^2, \tag{5.3}$$

with $j = i, m, o$ labeling the inner, middle and outer rings, respectively, as shown in Fig. 5.1. In order to obtain the lowest energy eigenstate of a single atom in a harmonic ring potential, we use a variational approach with the ansatz

$$\Psi_{r,j}(r) = N_j e^{-\alpha_j(r - \beta_j r_j)^2}, \tag{5.4}$$

where α_j and β_j are the variational parameters, and N_j is fixed by the normalization condition $2\pi \int_0^\infty |\Psi_{r,j}(r)|^2 r\,dr = 1$, which leads to

$$N_j = \sqrt{\frac{2\alpha_j/\pi}{e^{-2\alpha_j\beta_j^2 r_j^2} + \beta_j r_j\sqrt{2\pi\alpha_j}\left(\text{erf}\left(\beta_j r_j \sqrt{2\alpha_j}\right) + 1\right)}}. \tag{5.5}$$

The joint potentials $V_T(r)$ sketched in Fig. 5.1 are modeled as piecewise combinations of the corresponding potentials given by Eq. (5.1) and Eq. (5.3), and are truncated at

the points where they coincide (see Eqs. (5.14), (5.16) and (5.17)). Truncated harmonic potentials have shown to give qualitatively similar results for SAP as smooth Gaussian [338], Pöschl–Teller potentials [335], or atom-chip systems [336]. Moreover, they allow to use a simple ansatz for the localized ground states such as the ones given in Eqs. (5.2) and (5.4).

The dynamics of a single atom trapped in these concentric potentials is governed by the 2D Schrödinger equation

$$i\hbar\frac{\partial}{\partial t}\Psi(r,\phi,t) = H\Psi(r,\phi,t), \tag{5.6}$$

where the Hamiltonian is

$$H = -\frac{\hbar^2}{2m}\left(\frac{\partial^2}{\partial r^2} + \frac{1}{r}\frac{\partial}{\partial r} + \frac{1}{r^2}\frac{\partial^2}{\partial\phi^2}\right) + V_T(r). \tag{5.7}$$

Note that the azimuthal dependence ϕ in Eq. (5.6) does not play any role in the dynamics if they are restricted to the ground states of the harmonic and harmonic ring potentials for which $\Psi(r,\phi,t) = \Psi(r,t)$. In the following, we will focus mainly on these states, although states carrying OAM (and thus having an azimuthal phase dependence) will be addressed at the end of Sec. 5.3.

Throughout this chapter, we will express all variables in dimensionless harmonic oscillator (h.o) units with respect to V_h ($m = \hbar = \omega_h = 1$).

5.2 Spatial Adiabatic Passage between two concentric potentials

In this section, we use the matter-wave analogue of the RAP to study the loading of an atom between a harmonic potential to a ring and the transport between two concentric rings. In both cases the transport is from the localized ground state of the inner potential to the ground state of the outer one. Therefore, we can use the few-state model approach, introduced in Sec. 2.5, to describe the dynamics of these two systems. In both cases we first derive the corresponding few-state model and then study the SAP process using both the model and the numerical simulations of the 2D SE.

5.2.1 Two-state model

In this section, we introduce the two-state model for the trapping configurations shown in Figs. 5.1(a) and (b). Let us assume that at any time the total atomic wavefunction can be written as a superposition of the two orthonormalized localized states of each individual potential as

$$\Psi_{2S}(r,t) = a_i(t)\widetilde{\Psi}_i(r) + a_o(t)\widetilde{\Psi}_o(r), \tag{5.8}$$

where a_i (a_o) is the probability amplitude for the atom to be in the inner (outer) potential.

Introducing the ansatz Ψ_{2S} into the Schrödinger equation (Eq. (5.6)), one obtains the two-state model,

$$i\hbar\frac{d}{dt}\begin{pmatrix} a_i \\ a_o \end{pmatrix} = \hbar\begin{pmatrix} 0 & -J/2 \\ -J/2 & \Delta \end{pmatrix}\begin{pmatrix} a_i \\ a_o \end{pmatrix},\qquad(5.9)$$

where

$$J = \frac{4\pi}{\hbar}\int_0^\infty \widetilde{\Psi}_i^*(r)H\widetilde{\Psi}_o(r)\,rdr,\qquad(5.10\text{a})$$

$$\Delta = \frac{2\pi}{\hbar}\left(\int_0^\infty \widetilde{\Psi}_o^*(r)H\widetilde{\Psi}_o(r)\,rdr - \int_0^\infty \widetilde{\Psi}_i^*(r)H\widetilde{\Psi}_i(r)\,rdr\right),\qquad(5.10\text{b})$$

are the tunneling rate and energy bias, respectively. The values of J and Δ used in the two-state model simulations are obtained by performing these integrals numerically with the corresponding wavefunctions. The states $\widetilde{\Psi}_j$ for $j = i, o$ are obtained by orthonormalizing the states Ψ_h and $\Psi_{r,o}$ for the configuration in Fig. 5.1(a) or $\Psi_{r,i}$ and $\Psi_{r,o}$ for the configuration in Fig. 5.1(b).

The eigenvalues of the standard two-state Hamiltonian in Eq. (5.9) are

$$E_\pm = \frac{\hbar}{2}\left(\Delta \pm \sqrt{\Delta^2 + J^2}\right),\qquad(5.11)$$

with corresponding eigenstates

$$\Psi_+(\theta) = \sin(\theta)\widetilde{\Psi}_i - \cos(\theta)\widetilde{\Psi}_o,\qquad(5.12\text{a})$$

$$\Psi_-(\theta) = \cos(\theta)\widetilde{\Psi}_i + \sin(\theta)\widetilde{\Psi}_o,\qquad(5.12\text{b})$$

where the mixing angle θ is given by

$$\tan(2\theta) = \frac{J}{\Delta}.\qquad(5.13)$$

5.2.2 RAP-like protocol

The RAP-like protocol can be understood in terms of the previously derived two-state model. By adiabatically following either Ψ_+ or Ψ_-, Eqs. (5.12), a single atom initially loaded into the localized ground state of the inner potential can be efficiently and robustly transferred to the outer one. Let us assume that initially, at $t = t_0$, one has $\Delta < 0$ with $|\Delta| \gg J$, such that the mixing angle in Eq. (5.13) is given by $\theta(t_0) = \pi/2$ and, according to Eq. (5.12a), $\Psi_{2S}(t_0) = \Psi_+(t_0) = \widetilde{\Psi}_i$. To transfer the atom to the outer potential by adiabatically following Ψ_+, one needs to slowly modify the energy bias and the tunneling rate such that at the end of the process, at $t = t_f$, $\Delta > 0$ and $|\Delta| \gg J$, which, in turn, means $\theta(t_f) = 0$ and $\Psi_{2S}(t_f) = \Psi_+(t_f) = -\widetilde{\Psi}_o$. To

avoid diabatic transitions and keep the atom in the energy eigenstate Ψ_+ for the whole dynamics, it is important to reach significant tunneling rates when the sign of the energy bias is reversed such that even at this moment the energies of the two eigenstates are substantially different, see Eq. (5.11).

First, let us consider the transfer of a single atom trapped in a harmonic potential into a harmonic ring, see Fig. 5.1(a). In this case, the joint potential profile reads:

$$V_T(r) = \begin{cases} V_h(r) & \text{for } r < \bar{r}_{hr}, \\ V_{r,o}(r) & \text{for } r \geq \bar{r}_{hr}, \end{cases} \tag{5.14}$$

with $\bar{r}_{hr} = r_o \omega_o / (\omega_h + \omega_o)$.

Therefore in our system in order to investigate the RAP-like process we modify the ring trapping frequency ω_o and radius r_o according to (see Figs. 5.2(a) and (b))
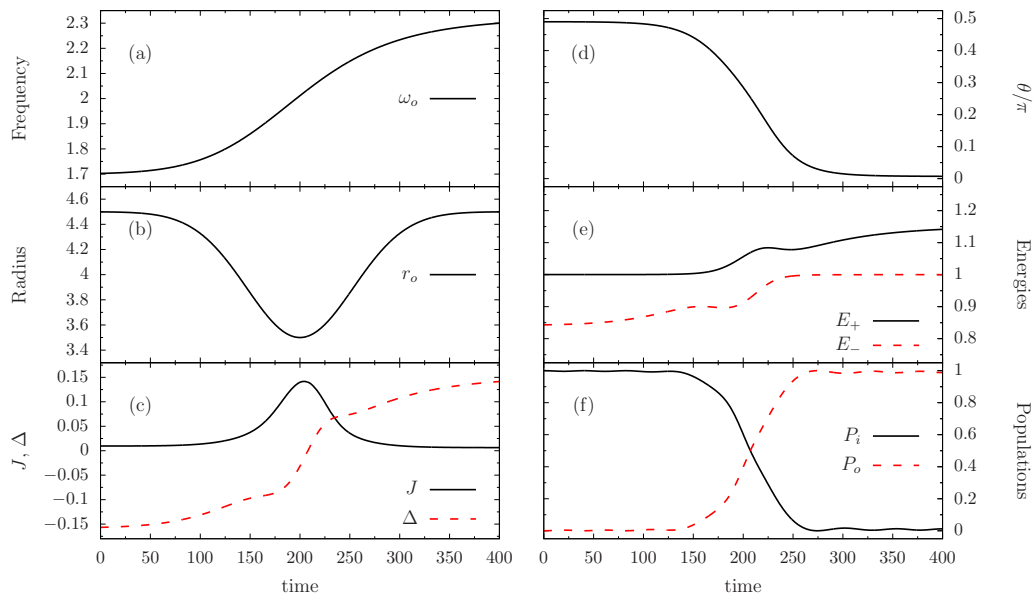
Figure 5.2: Numerical simulations using the two-state model. Matter-wave RAP process to transport a single atom from the localized ground state of a harmonic potential to the ground state a harmonic ring one, see Fig. 5.1(a). As a function of time: (a) trapping frequency ω_o and (b) radius of the harmonic ring potential r_o; (c) tunneling rate J (black solid line) and energy bias Δ (red dashed line); (d) mixing angle θ; (e) eigenvalues $E_\pm$ of the energy eigenstates Ψ_+ (black solid line) and Ψ_- (red dashed line); and (f) populations $P_i = |a_i|^2$ (black solid line) and $P_o = |a_o|^2$ (red dashed line) of the harmonic and harmonic ring potentials. All variables are expressed in h.o. units with respect to the potential V_h.

$$\omega_o(t) = \quad \omega_0 + \delta_\omega \frac{1+\left(\frac{2}{3}\right)^a}{1+\left(\frac{t}{t_f}+\frac{1}{2}\right)^{-a}}, \tag{5.15a}$$

$$r_o(t) = \quad R_0 + \delta_R e^{-\frac{\left(\frac{t}{t_f}-\frac{1}{2}\right)^2}{2\sigma^2}}, \tag{5.15b}$$

with the parameter values $t_f = 400$, $R_0 = 4.5$, $\delta_R = -1$, $\omega_0 = 1.7$, $\delta_\omega = 0.6$, $a = 8$, and $\sigma = 2/15$. These modifications of the potential yield the temporal variations of the energy bias and tunneling shown in Fig. 5.2(c), calculated with Eqs. (5.10).

The temporal evolution of the mixing angle is plotted in Fig. 5.2(d), while Fig. 5.2(e) shows the evolution of the energy eigenvalues (Eq. (5.11)), revealing the existence of an energy gap during the whole dynamics. The populations of the harmonic and harmonic ring potentials are shown in Fig. 5.2(f), which demonstrate the high fidelity of the transport protocol. Let us comment here that, as in all adiabatic protocols, the exact time dependence of the parameters is not crucial for the technique to succeed, and even withstands some noise [337, 338]. We have chosen this particular time dependence as it allows for shorter total times t_f of the protocol with respect to other simpler temporal variations of the parameters.

To check the validity of the two-state model we have also performed numerical sim-
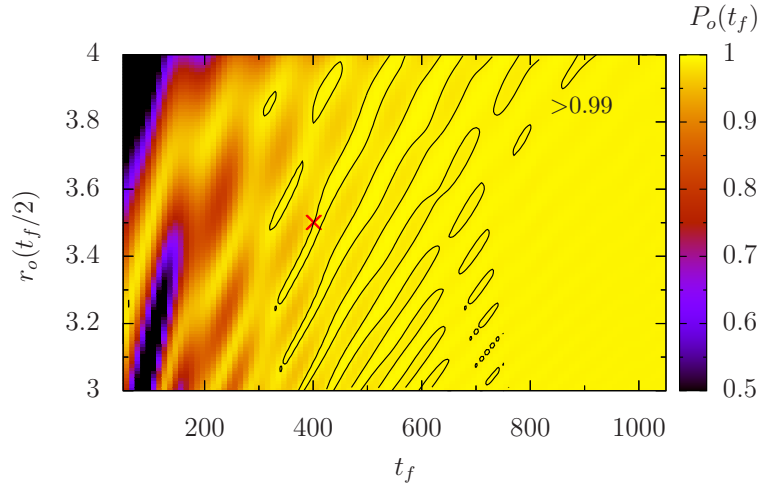
Figure 5.3: Numerical integration of the 2D Schrödinger equation. Final population transferred to the harmonic ring trap from the inner harmonic trap as a function of the total time of the process and the minimum radius of the ring trap during the process. All other parameters are as in Fig. 5.2. Black lines correspond to contours at $P_o(t_f) = 0.99$ and the cross indicates the parameter values that were chosen in the two-state simulations shown in Fig. 5.2. All variables are expressed in h.o. units with respect to the harmonic potential V_h.

ulations of the RAP-like protocol using the 2D Schrödinger equation (Eq. (5.6)) for the same parameters as in Fig. 5.2. Fig. 5.3 shows the final population transferred from the harmonic inner potential to the outer ring, P_o, as a function of the total time of the process and the minimum radius of the ring during the process. A population transfer above 99% is achieved for a broad range of parameter values evidencing the fidelity and robustness of the process. The parameters corresponding to the transport protocol investigated within the two-state model above are marked with a cross in Fig. 5.3.

The previously described RAP-like technique can also be applied to the configuration shown in Fig. 5.1(b) corresponding to two concentric harmonic ring potentials described by the potential

$$V_T(r) = \begin{cases} V_{r,i}(r) & \text{for } r < \bar{r}_{io} \\ V_{r,o}(r) & \text{for } r \geq \bar{r}_{io} \end{cases} \tag{5.16}$$

with $\bar{r}_{io} = (r_i \omega_i + r_o \omega_o)/(\omega_i + \omega_o)$.

As shown in Figs. 5.4(a) and (b), we change the frequency and radius of the outer
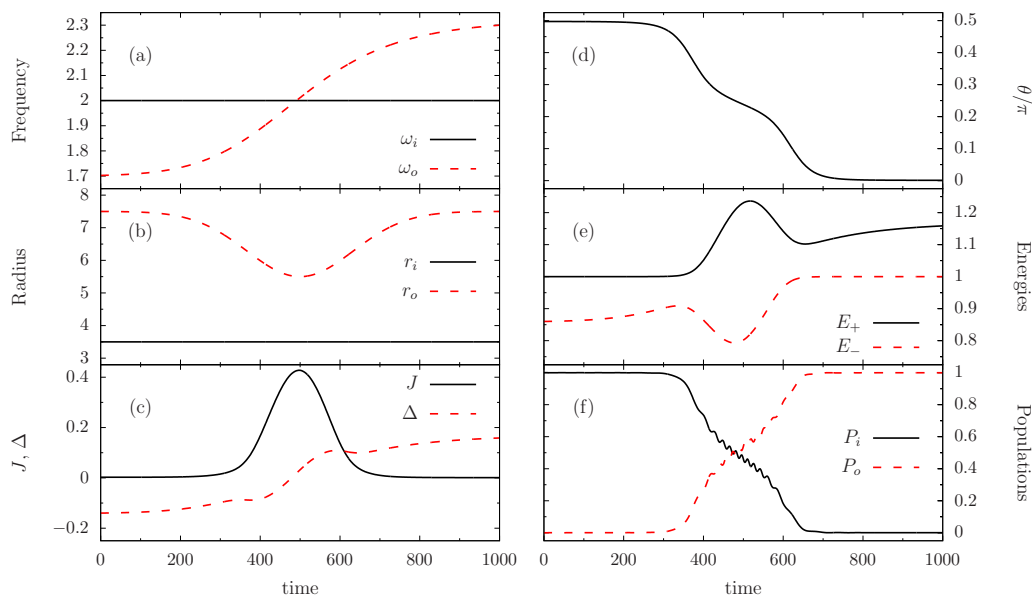
Figure 5.4: Numerical simulations using the two-state model. Matter-wave RAP process to transport a single atom between two concentric ring potentials, see Fig. 5.1(b). As a function of time: (a) trapping frequencies ω_i (black solid line) and ω_o (red dashed line) of the inner and outer rings; (b) radii r_i (black solid line) and r_o (red dashed line) of the inner and outer rings; (c) tunneling rate J (black solid line) and energy bias Δ (red dashed line); (d) mixing angle θ; (e) eigenvalues $E_{\pm}$ of the energy eigenstates Ψ_+ (black solid line) and Ψ_- (red dashed line); (f) populations $P_i = |a_i|^2$ (black solid line) and $P_o = |a_o|^2$ (red dashed line) of the inner and outer rings. All variables are expressed in h.o. units with respect to the harmonic potential V_h.

ring in time following Eqs. (5.15) with parameters $\omega_0 = 1.7$, $\delta_\omega = 0.6$, $R_0 = 7.5$, and $\delta_R = 2$, while leaving the inner ring fixed with radius $r_i = 3.5$ and frequency $\omega_i = 2$. Then, the temporal profiles of the energy bias and the tunneling rate, see Fig. 5.4(c), are such that the mixing angle θ evolves from $\pi/2$ to 0, see Fig. 5.4(d). In this case, the followed eigenstate Ψ_+ is transformed from initially being the inner ring ground state to finally being the outer ring one. Therefore, the single atom is transported from the inner ring to the outer one with very high fidelity, see Fig. 5.4(f).

5.3 Spatial Adiabatic Passage between three concentric potentials

In this section we consider three concentric ring potentials to study the transport between the innermost ring to the outermost one following the STIRAP-like protocol. In particular, we transport a localized eigenstate state of the inner ring to a degenerate (or quasi degenerate) localized eigenstate of the outer one. As in the previous section, we can again use the few-state model approach introduced in Sec. 2.5 to describe the dynamics in terms of localized eigenstates of the rings. Few-state models and the numerical simulations of the 2D SE are both compared in the two cases investigated here, obtaining excellent agreement.

5.3.1 Three-state model

We now consider the trapping configuration depicted in Fig. 5.1(c) consisting of three concentric ring potentials, constructed from truncated harmonic potentials

$$
V_T(r) = \begin{cases} V_{r,i}(r) & \text{for } r \leq \bar{r}_{im} \\ V_{r,m}(r) & \text{for } \bar{r}_{im} < r < \bar{r}_{mo} \\ V_{r,o}(r) & \text{for } r \geq \bar{r}_{mo} \end{cases} \tag{5.17}
$$

with $\bar{r}_{im} = (r_i \omega_i + r_m \omega_m)/(\omega_i + \omega_m)$ and $\bar{r}_{mo} = (r_m \omega_m + r_o \omega_o)/(\omega_m + \omega_o)$.

In analogy with the previous section, we assume that the total atomic wavefunction can be written at all times as a superposition of the three orthonormalized localized ground states of each individual potential as

$$
\Psi_{3S}(r,t) = a_i(t)\widetilde{\Psi}_i(r) + a_m(t)\widetilde{\Psi}_m(r) + a_o(t)\widetilde{\Psi}_o(r). \tag{5.18}
$$

The equations of motion for the probability amplitudes a_i, a_m, a_o of the inner, middle, and outer ring potentials, respectively, read

$$
i\hbar \frac{d}{dt} \begin{pmatrix} a_i \\ a_m \\ a_o \end{pmatrix} = \hbar \begin{pmatrix} \Delta_i & -J_{im}/2 & 0 \\ -J_{im}/2 & 0 & -J_{mo}/2 \\ 0 & -J_{mo}/2 & \Delta_o \end{pmatrix} \begin{pmatrix} a_i \\ a_m \\ a_o \end{pmatrix}, \tag{5.19}
$$

where we have taken the energy of the ground state of the middle ring as the energy origin, and the definitions of the tunnelling rates and energy biases are obtained analogously to Eqs. (5.10) with the corresponding localized wavefunctions.

For $\Delta_i = \Delta_o = 0$, the eigenstates of the Hamiltonian read:

$$E_+ = \frac{1}{2}\sqrt{J_{im}^2 + J_{mo}^2}, \tag{5.20}$$

$$E_- = -\frac{1}{2}\sqrt{J_{im}^2 + J_{mo}^2}, \tag{5.21}$$

$$E_d = 0, \tag{5.22}$$

with eigenstates:

$$\Psi_+(\Theta) = \frac{1}{\sqrt{2}}\left(\sin\Theta\widetilde{\Psi}_i + \widetilde{\Psi}_m + \cos\Theta\widetilde{\Psi}_o\right), \tag{5.23}$$

$$\Psi_-(\Theta) = \frac{1}{\sqrt{2}}\left(\sin\Theta\widetilde{\Psi}_i - \widetilde{\Psi}_m + \cos\Theta\widetilde{\Psi}_o\right), \tag{5.24}$$

$$\Psi_d(\Theta) = \cos\Theta\widetilde{\Psi}_i - \sin\Theta\widetilde{\Psi}_o, \tag{5.25}$$

where $\Psi_d(\Theta)$ is the so-called spatial dark state, which involves only the localized ground states of the inner and outer rings, with:

$$\tan\Theta = \frac{J_{im}}{J_{mo}}. \tag{5.26}$$

5.3.2 STIRAP-like protocol

In this chapter we introduce the matter-wave analogue of the STIRAP protocol in terms of the three-state model presented in the previous section. This SAP process for a single atom being transfered between the innermost and outermost rings can be achieved by adiabatically following Ψ_d (Eq. (5.25)). Starting with the atom in the inner ring, $\Psi_{3S}(t_0) = \Psi_d(t_0) = \widetilde{\Psi}_i$, and employing a temporal variation of the tunneling rates such that Θ, see Eq. (5.26), slowly changes from 0 to $\pi/2$, one obtains $\Psi_{3S}(t_f) = \Psi_d(t_f) = -\widetilde{\Psi}_o$ at the end of the process. Note that this temporal variation of the mixing angle means to favor first tunneling between the middle and outer rings and later on, and with an appropriate temporal delay, tunneling between the inner and middle rings.

Fig. 5.5(a) shows the specific temporal variation of the inner and outer rings radii that has been used to achieve the proper variation of the tunneling rates, shown in Fig. 5.5(b). In this case, the time dependences of the radii are described as in the previous cases by Eq. (15b), with $R_0 = 3, \delta_R = 2$ for the inner ring and $R_0 = 12, \delta_R = -2$ for the outer one. The middle ring has a fixed radius $r_m = 7.5$, and, since no detuning is necessary, all ring trapping frequencies are kept constant and equal to $\omega_i = \omega_m = \omega_o = 2$. The parameter

setting chosen implies that the orthonormal localized ground states are not fully resonant during the whole dynamics, see Fig. 5.5(c). However, since $|\Delta_o - \Delta_i| \ll J_{im}, J_{mo}$ in the time window where tunneling is non-negligible, it is possible to follow Ψ_d from $\Theta = 0$ to $\Theta = \pi/2$ in this interval, as depicted in Fig. 5.5(d). This adiabatic following results in a high fidelity single atom transport from the inner ring to the outer one, with an almost negligible population in the middle one for the whole dynamics, see Fig. 5.5(f).
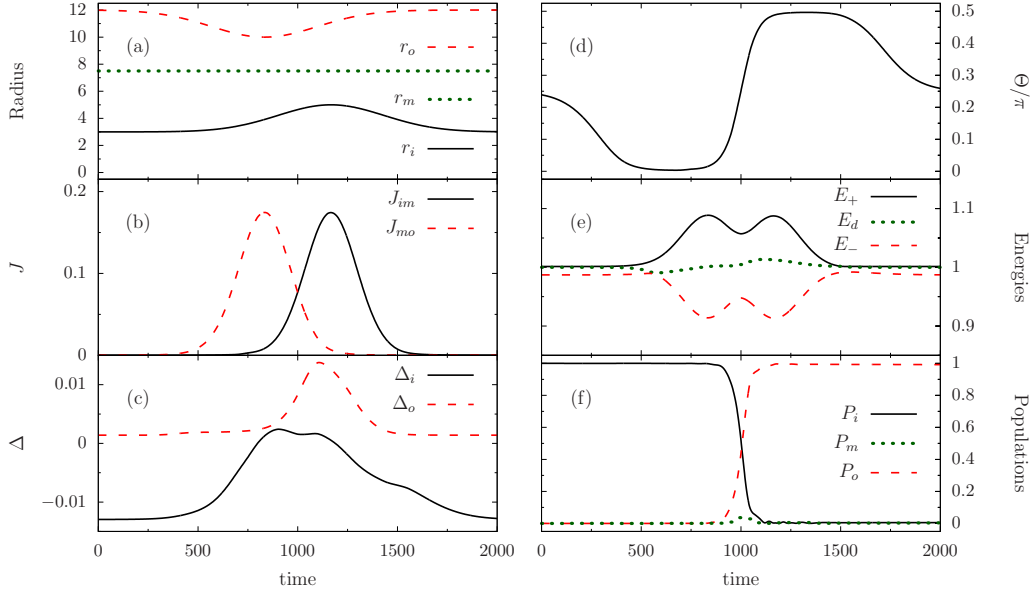
Figure 5.5: Numerical simulations using the three-state model. Matter-wave STIRAP process to transport a single atom from the innermost to the outermost potential of three concentric rings, see Fig. 5.1(c). As a function of time: (a) radii r_i (black solid line), r_m (green dotted line) and r_o (red dashed line) of the inner, middle and outer rings; (b) tunneling rates J_{im} (black solid line) and J_{mo} (red dashed line); (c) energy bias Δ_i (black solid line) and Δ_o (red dashed line) of the inner and outer rings with respect to the middle one; (d) mixing angle Θ; (e) eigenvalues of the energy eigenstates Ψ_+ (black solid line), Ψ_d (green dotted line), and Ψ_- (red dashed line); (f) populations $P_i = |a_i|^2$ (black solid line), $P_m = |a_m|^2$ (green dotted line), and $P_o = |a_o|^2$ (red dashed line) of the inner, middle, and outer rings. All variables are expressed in h.o. units with respect to the harmonic potential V_h.

Fig. 5.6(a) shows the temporal evolution of the populations in the inner, middle, and outer rings, respectively, obtained from the numerical integration of the corresponding 2D Schrödinger equation for the same parameter values as used for Fig. 5.5, and where the initial ground state is obtained via imaginary time evolution. The fidelity of the SAP process is above 99%. Fig. 5.6 (c) shows snapshots of the 2D probability density for the three different times indicated in the temporal evolution. The same protocol applied to a state with OAM is plotted in Figs. 5.6(b) and (d). The initial ground state
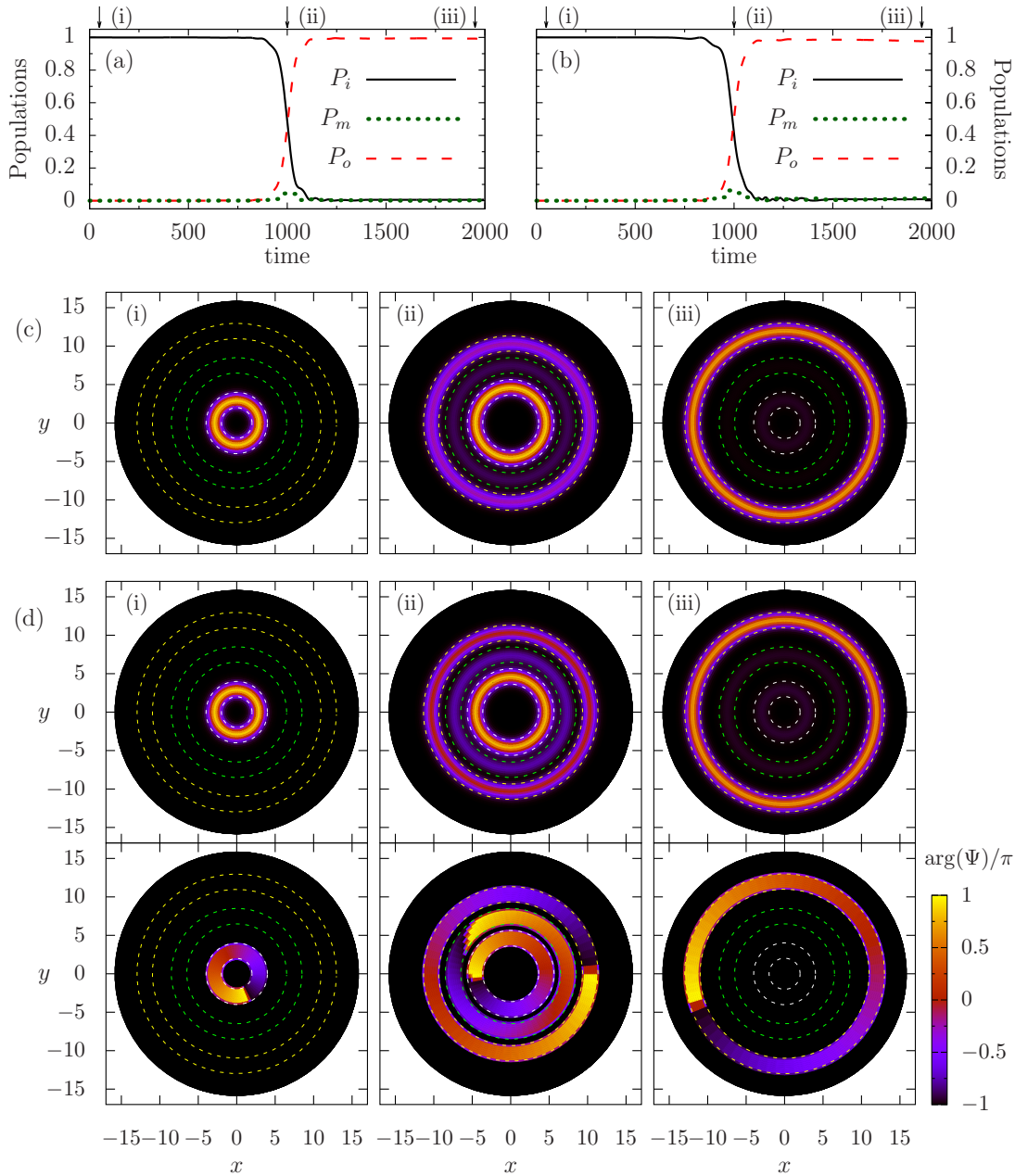
Figure 5.6:   Numerical integration of the 2D Schrödinger equation to simulate the matter-wave STIRAP process to transport a single atom from the innermost to the outermost potential of three concentric rings, see Fig. 5.1(c). Time evolution of the populations of the inner, middle and outer rings when the initial state (obtained from imaginary time evolution) (a) does not posses OAM or (b) carries one unit of OAM. (c) Snapshots of the 2D atomic probability density for the three times indicated in (a). (d) Snapshots of the 2D atomic probability density (top row) and phase distribution (bottom row) for the three times indicated in (b). Parameters are the same as in Fig. 5.5.

is taken to be the one obtained via imaginary time evolution with an added azimuthal phase $\exp(i\phi)$, and thus with a winding number of one. The time evolution of the populations from the 2D Schrödinger equation in Fig. 5.6(b) shows a final fidelity above 97%. Moreover, Fig. 5.6 (d) shows snapshots for the three different times indicated in the temporal evolution of both the 2D probability density (top row) and the corresponding phase distribution (bottom row). Note, comparing the phase distribution in (d,i) with that in (d,iii), that initial and final states have the same OAM winding number. This is because the joint trapping potential consists of three concentric rings and, therefore, cylindrical symmetry is preserved during the whole dynamics.

5.4 Conclusions

We have investigated SAP processes for the transport of a single-atom from an inner trap to an outer one in three different configurations of cylindrically symmetric concentric potentials. The energy eigenstates followed, have been transformed from the localized ground states of the inner potentials to the localized ground states of the outer rings by manipulating the trapping frequencies and/or the radii of the rings. In particular, we have studied the matter-wave analogues of the RAP and STIRAP techniques. In the latter case, we have also investigated the possibility to use SAP processes between three concentric ring potentials to transport OAM states. Such transport can play a very important role in future atomtronic devices, where OAM states are one of the building blocks to study SQUIDs [12, 13, 15, 327–330]. While in 1D systems the energy biases are only affected by the difference in frequencies of the traps, in 2D SAP systems, the energies also depend on their radii and thus, coupling and detuning cannot be treated as independent parameters. This is more evident for OAM states where extra degrees of freedom are present. Nevertheless, here we have shown, with an example, that OAM states of an ultracold atom can still be transported using the STIRAP protocol.

Time-averaged adiabatic potentials would be ideal systems to perform these techniques because of their strong confinements on the order of kHz, their possibility of realising trapping lifetimes on the order of up to one minute [313] and their ability to dynamically change the radius of the traps [312]. Our estimations show that the techniques presented in this chapter can be implemented in these systems with a total process time on the order of seconds. Similar total times can be expected for the painted potentials [183, 185].

We have demonstrated the high efficiency of these SAP processes by means of simple two- and three-state models. Additionally, we have checked the accuracy of these models by comparing their predictions with the numerical integration of the corresponding 2D Schrödinger equation. Moreover, the fidelity and robustness of the RAP process has also been investigated, showing that SAP techniques are not subject to specific temporal variations of the parameters as long as the considered eigenstate of the system is followed in an adiabatic way.

Geometrically induced complex tunnelings for ultracold atoms carrying orbital angular momentum

In this chapter, we investigate the dynamics of angular momentum states for a single ultracold atom trapped in 2D systems of sided-coupled ring potentials [63]. By using the symmetries of the system, we show that tunneling amplitudes between different ring states with variation of the winding number are complex. This is particularly interesting considering that the complex character of the tunneling appears naturally in these systems. In a triangular ring configuration, complex tunneling amplitudes allow us to geometrically engineer spatial dark states to manipulate the transport of orbital angular momentum states via quantum interference. The dynamics of these systems is described using few-state models whose comparison with numerical simulations of the 2D Schrödinger equation (SE) give an excellent agreement.

As discussed in the introduction of this thesis, tunneling is one of the paradigms of quantum mechanics and, the tunneling control in the context of ultracold neutral atoms has been a subject of intense research in recent years. Pioneering experiments demonstrated dynamical tunneling suppression for a single-particle in a strongly driven double-well potential [350] and for a Bose-Einstein condensate (BEC) in a strongly driven optical lattice [351]. The dynamical modification of tunneling rates allowed experimentally realizing [352] the driving-induced superfluid-Mott insulator transition [353, 354] and, by independently tuning the coupling rates in different directions of a triangular lattice, simulating a large variety of magnetic phases and different types of phase transitions [355].

The generation of artificial vector gauge potentials for ultracold atoms in 1D optical lattices has been demonstrated by inducing controllable complex tunneling amplitudes. These effective complex couplings can be realized, for instance, by a suitable forcing

of an optical lattice [61] or by a combination of radio frequency and optical Raman coupling fields [62]. In 2D optical lattices, the engineering of complex tunnelings has lead to the generation of staggered fluxes [64, 65], the implementation of the Hofstadter Hamiltonian and the observation of large homogeneous artificial magnetic fields [66], as well as the realization of the topological Haldane model [67] and of the Harper and Weyl Hamiltonians [68, 69].

In this chapter, we demonstrate that complex tunneling amplitudes appear naturally in the dynamics of orbital angular momentum states for a single ultracold atom trapped in 2D systems of sided coupled cylindrically symmetric identical traps. We focus on ring shaped potentials, which are currently implemented for ultracold atoms by means of the optical dipole force (see Sec. 2.4) or magnetic trapping. Techniques for the first case include optically plugging magnetic traps [210, 211], the use of static Laguerre-Gauss beams [212–216], painting potentials [183–185], time averaged potentials [186, 187] and conical refraction [92]. Alternatively, magnetic ring traps can be implemented using static magnetic fields [200–203], time-averaged magnetic fields [204–206], by induction [207, 208] and using radiofrequency adiabatic potentials [209]. The importance of ring traps for ultracold atoms comes from the fact that they are one of the simplest geometries that lead to non-trivial loop circuits in the emerging field of Atomtronics [24, 356], which explores the use of neutral atoms to build analogues of electronic circuits and devices. Specifically, BECs in a ring trap with one [12, 25, 330, 357] or two [13, 14, 358] weak links have been shown to resemble the physical behaviour of superconducting quantum interference devices (SQUIDs). Atomic SQUIDs in a ring lattice have also been proposed [15, 359].

In particular, the present chapter considers the dynamics of the angular momentum states of a single atom trapped in two 2D in-line ring potentials (Sec. 6.1) and three 2D rings in a triangular configuration (Sec. 6.2). In Sec. 6.1 we show that the full dynamics Hilbert space consists of a set of decoupled manifolds spanned by ring states with identical vibrational and orbital angular momentum quantum numbers. By recalling basic geometric symmetries of the system, we demonstrate that the tunneling amplitudes between different ring states, named *cross-couplings*, with (without) variation of the winding number, are complex (real) and that a complex *self-coupling* between states with opposite winding number within a ring, arises due to the breaking of cylindrical symmetry induced by the presence of additional rings. In Sec. 6.2 we show that, although for two in-line rings the complex cross-coupling contribution gives a non-physically relevant phase, in a triangular ring configuration it leads to the possibility of engineering spatial dark states, allowing the manipulation of the transport of angular momentum states via quantum interference.

6.1   Two in-line ring potentials

We consider a single atom trapped in a 2D system consisting of two in-line ring potentials of radius r_0 separated by a distance d, see Fig. 6.1(a). We define the radial coordinate r_j and the azimuthal angle ϕ_j with respect to the center of each ring, where $j = L,\ R$ accounts for the left and right potentials, respectively. The angular momentum eigenstates of each individual ring potential read:

$$\Psi_{j,m}^{n}(r_j, \phi_j) = \langle \vec{r} | j, m, n \rangle = \frac{1}{\sqrt{N}} \psi_m(r_j) e^{in(\phi_j - \phi_0)}, \qquad (6.1)$$

where $j = L,\ R$; $n = \pm l$ is the winding number with $l \in \mathbb{N}^0$ being the orbital angular momentum quantum number, $\psi_m(r_j)$ with $m \in \mathbb{N}^0$ is the radial part of the wave function for the m transverse vibrational state, ϕ_0 is a free phase parameter, defined with respect to the x axis, which sets the azimuthal phase origin, and N is a normalization constant.
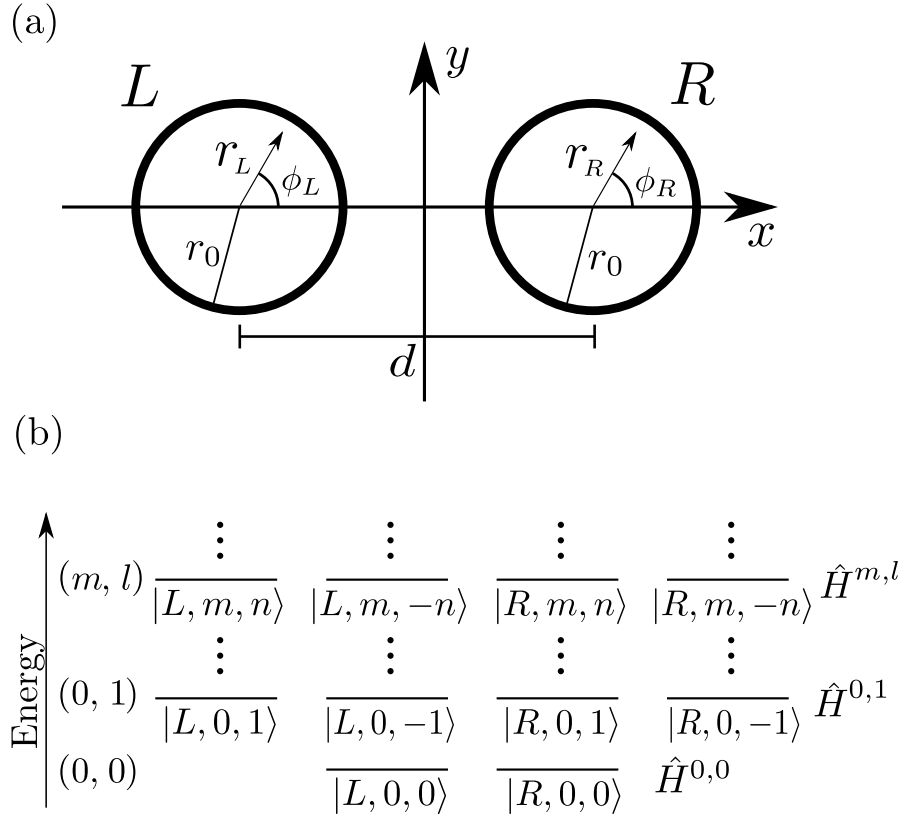
Figure 6.1: (a) Schematic figure of two in-line ring potentials. (b) Sketch of the energy spectrum of the angular momentum eigenstates $|j, m, n\rangle$ for a single atom trapped in each of the two in-line rings, where $j = L,\ R$ indicates the ring, m the transverse vibrational state, $n = \pm l$ the winding quantum number, and l the orbital angular momentum. The Hamiltonian corresponding to the (m, l) manifold is indicated by $\hat{H}^{m,l}$.

Without loss of generality, we assume $\psi_m(r_j)$ to be real and, thus, the phases of
the, in general, complex tunneling amplitudes will be only determined by ϕ_0. To obtain
these phases, we recall that two identical in-line rings present two symmetries, the x
and the y mirrors defined as:

$$\hat{M}_x: \quad (x, \, y) \longrightarrow (x, \, -y), \tag{6.2a}$$

$$\hat{M}_y: \quad (x, \, y) \longrightarrow (-x, \, y), \tag{6.2b}$$

respectively. The effects of such transformations on the angular momentum eigenstates,
Eq. (6.1), are:

$$\hat{M}_x|j,m,n\rangle = e^{-2in\phi_0}|j,m,-n\rangle, \tag{6.3a}$$

$$\hat{M}_y|j,m,n\rangle = e^{-2in\phi_0}e^{in\pi}|k,m,-n\rangle \text{ for } j \neq k. \tag{6.3b}$$

Assuming $\sigma_m \ll r_0 \ll d$, where σ_m is the radial width of the atom in the m vibra-
tional state of any of the two rings, the total Hamiltonian of the system reads:

$$\hat{H}_T = \sum_{m\geq 0} \hat{H}^{m,0} + \sum_{m\geq 0}\sum_{l>0} \hat{H}_{FS}^{m,l}, \tag{6.4}$$

where $\hat{H}^{m,0}$ accounts for the two-state Hamiltonian associated to $|L,m,0\rangle$ and $|R,m,0\rangle$,
and $\hat{H}_{FS}^{m,l}$ corresponds to the four-state Hamiltonian (FSH) for each (m,l) combination
with $l \neq 0$, whose basis is formed by four degenerate angular momentum eigenstates
$|L,m,\pm n\rangle$, $|R,m,\pm n\rangle$, see Fig. 6.1(b):

$$\hat{H}_{FS}^{m,l} = \frac{\hbar}{2}\sum_{j,k=L,R}\sum_{n=\pm l} \left(J_{j,n}^{k,n}(m)|j,m,n\rangle\langle k,m,n|+ \right.$$
$$\left. J_{j,n}^{k,-n}(m)|j,m,n\rangle\langle k,m,-n| \right), \tag{6.5}$$

where $(\hbar/2)J_{j,n}^{j,n}(m)$ are the eigenenergies of a single atom in an uncoupled ring, $J_{j,n}^{j,-n}(m)$
are the self-coupling tunnelings, and $J_{j,n}^{k,-n}(m)$ and $J_{j,n}^{k,n}(m)$ with $j \neq k$ are the cross-
coupling tunnelings.

The Hamiltonian describing this system is invariant under $\hat{M}_x$ and $\hat{M}_y$ transforma-
tions and, consequently, under parity $\hat{P} = \hat{M}_x\hat{M}_y$. Using the symmetry transformations
acting on the angular momentum states, Eqs. (6.3), we obtain that:

$$\hat{M}_x: \qquad\qquad J_{j,n}^{k,n} = J_{j,-n}^{k,-n}, \tag{6.6a}$$

$$e^{-2in\phi_0}J_{j,n}^{k,-n} = e^{2in\phi_0}J_{j,-n}^{k,+n}, \tag{6.6b}$$

$$\hat{M}_y: \qquad J_{j,n}^{k,n} = J_{k,-n}^{j,-n}, \quad J_{j,n}^{j,n} = J_{k,-n}^{k,-n} \text{ for } j \neq k, \tag{6.6c}$$

$$e^{-2in\phi_0}J_{j,n}^{k,-n} = e^{2in\phi_0}J_{k,-n}^{j,n} \text{ for } j \neq k, \tag{6.6d}$$

$$e^{-2in\phi_0}J_{j,n}^{j,-n} = e^{2in\phi_0}J_{k,-n}^{k,n} \text{ for } j \neq k, \tag{6.6e}$$

These relations between the couplings along with the Hermiticity of the Hamiltonian, reduce the parameter space to only three different couplings: a real coupling $J_{L,n}^{R,n}$ and two complex ones $J_{L,n}^{L,-n} = |J_{L,n}^{L,-n}|e^{2in\phi_0}$ and $J_{L,n}^{R,-n} = |J_{L,n}^{R,-n}|e^{2in\phi_0}$. For two rings, we can fix ϕ_0 to any arbitrary value. Thus, for $\phi_0 = 0$ all couplings become real and the four-state Hamiltonian $\hat{H}_{FS}^{m,l}$ reads:

$$\hat{H}_{FS}^{m,l} = \frac{\hbar}{2} \begin{pmatrix} 0 & J_{L,n}^{L,-n} & J_{L,n}^{R,n} & J_{L,n}^{R,-n} \\ J_{L,n}^{L,-n} & 0 & J_{L,n}^{R,-n} & J_{L,n}^{R,n} \\ J_{L,n}^{R,n} & J_{L,n}^{R,-n} & 0 & J_{L,n}^{L,-n} \\ J_{L,n}^{R,-n} & J_{L,n}^{R,n} & J_{L,n}^{L,-n} & 0 \end{pmatrix}, \tag{6.7}$$

where we have subtracted the common energy from the diagonal. In fact, the complex nature of the self-couplings and cross-couplings with winding number exchange does not play any physical role in the two in-line ring configuration. However, as detailed in Sec. 6.2, it will become crucial when studying the dynamics of more than two coupled rings. Note also that, although for a single ring $J_{j,n}^{j,-n} = 0$, in the case of two in-line coupled rings a non null coupling appears between opposite winding number states in the same ring. This coupling emerges due to the breaking of cylindrical symmetry in the system [360], produced by the presence of the second ring.

To numerically investigate the free dynamics of a single atom of mass M in two in-line rings, Fig. 6.1(a), we consider two truncated harmonic ring potentials of frequency ω:

$$V(x,y) = \begin{cases} \frac{1}{2}M\omega^2(\sqrt{x^2 + y^2} - r_0)^2 & \text{for } x \leq d/2 \\ \frac{1}{2}M\omega^2(\sqrt{(x-d)^2 + y^2} - r_0)^2 & \text{for } x > d/2 \end{cases}. \tag{6.8}$$

The atom is initially trapped in state $|L, 0, 1\rangle$. The distance between rings is kept fixed during the dynamics at $d = 14$ and $r_0 = 5$, all in 1D radial harmonic oscillator (h.o.) units.

Fig. 6.2(a) shows the temporal evolution of the populations of the four angular momentum states of the $(0, 1)$ manifold by using the FSH, Eq. (6.7), and the numerical integration of the full 2D SE (see appendix C for the specifics of the numerical methods). The perfect agreement has been achieved by taking $J_{L,1}^{R,1} = 3.06 \times 10^{-3}$, $J_{L,1}^{R,-1} = 3.28 \times 10^{-3}$ and $J_{L,1}^{L,-1} = -4.06 \times 10^{-4}$ in the FSH, in h.o. units. These values of the tunneling amplitudes for the FSH have been obtained by numerically constructing the eigenstates basis of the total system. Then, by taking states with angular momentum $n = \pm 1$, that are degenerate in the basis $|j, 0, \pm 1\rangle$ (with $j = L, R$), we are able to build a FSH whose diagonalization gives rise to a simple relation between the eigenenergies of the total system and the tunneling amplitudes of the mentioned FSH (for further details see appendix B).

The dynamics shows that the population is being initially transferred from $|L, 0, 1\rangle$ to states $|R, 0, \pm 1\rangle$ to come back again (B in Fig. 6.2(a)) to the left trap but mostly
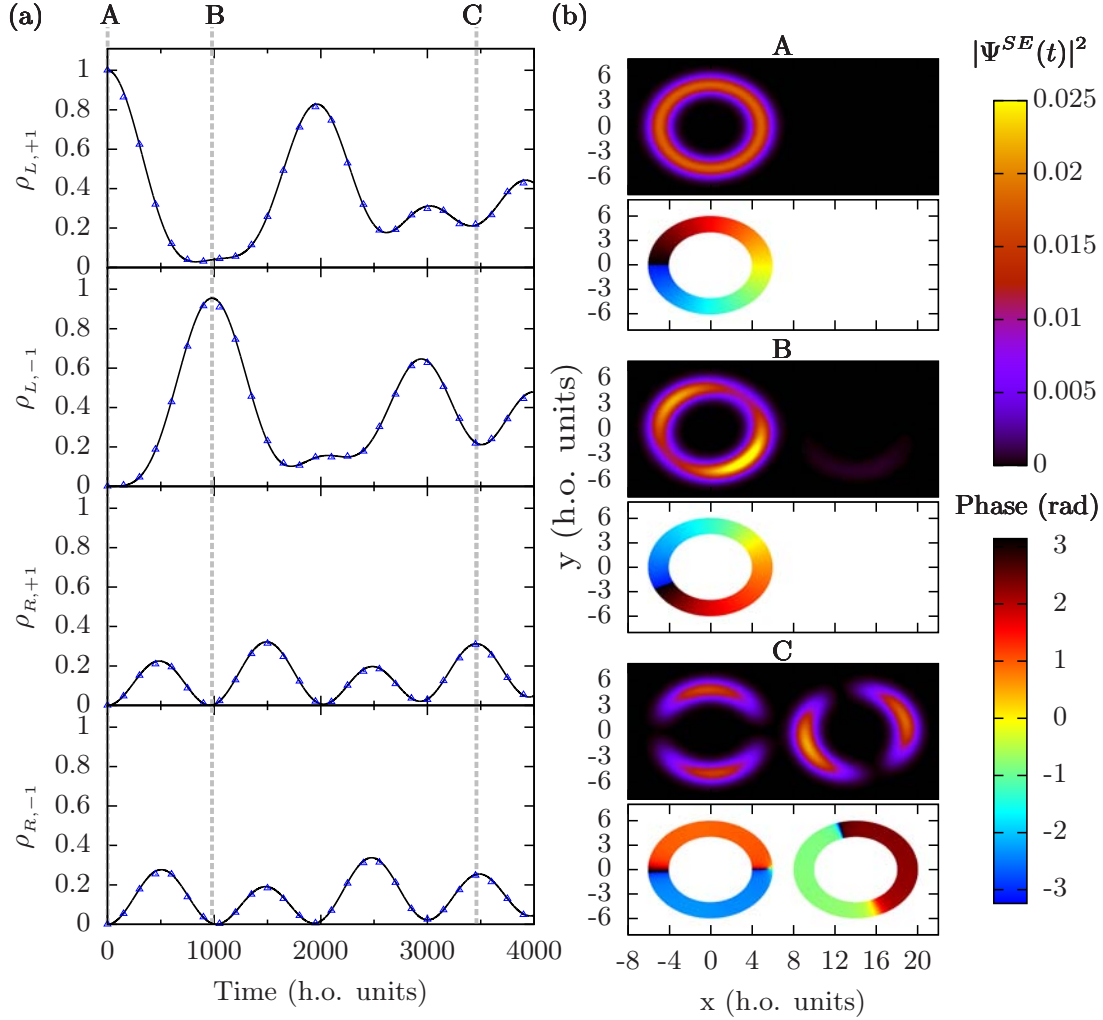
Figure 6.2: (a) Temporal evolution of the population of each angular momentum state involved in the dynamics, $\rho_{j,\pm1} = |\langle\Psi(t)|j,0,\pm1\rangle|^2$, where $j = L, R$, using the numerically integrated 2D SE (points) and the FSH, Eq. (6.7), (lines). (b) Atomic probability density (upper plots) and phase distribution (lower plots) of the state of the system at times A, B, C in Fig. 6.2(a). The phase is only plotted where the probability density is non negligible. For the parameters see text.

with opposite winding number, i.e., to state $|L, 0, -1\rangle$. From the FSH numerical simulations, we have checked that there are no complete population oscillations between states $|L, 0, 1\rangle$ and $|L, 0, -1\rangle$ due to the self-coupling contribution $J_{L,1}^{L,-1}$. Note that since the self-coupling appears due the asymmetry of the system and the cross-coupling has two contributions, the asymmetry and the tunneling through the kinetic energy term between the two rings, the tunneling amplitude of the self-coupling is in general smaller than the cross-coupling. In particular, in our example the self-coupling is roughly one order of magnitude smaller than the cross-couplings (see Fig. B.1).

From the integration of the 2D SE, Fig. 6.2(b) shows the atomic probability density and the phase distribution at times A, B and C in Fig. 6.2(a). A corresponds to the initial state $|L, 0, 1\rangle$. In B, we observe the appearance of two minima in the left ring probability density produced by the coexistence of states $|L, 0, 1\rangle$ and $|L, 0, -1\rangle$. Finally, C corresponds to the state formed by an approximately equally weighted superposition of the four states of the $(0, 1)$ manifold. Accordingly, two density nodes appear in each ring.

6.2 Triangular configuration

We consider now three identical ring potentials (labeled L, C, R from left, central and right) of radius r_0 in a triangular configuration with distances between their centers $d_{CL} = d_{CR} \equiv d$ and $d_{LR} = 2d \sin(\Theta/2)$, see Fig. 6.3.

Considering the angular momentum eigenstates of each ring, Eq. (6.1), the bare energy spectrum of a single atom trapped in any of the three ring potentials is formed by a set of manifolds of six degenerate angular momentum states, for each (m, l) combination with $l \neq 0$, $|L, m, \pm n\rangle$, $|C, m, \pm n\rangle$ and $|R, m, \pm n\rangle$ plus manifolds of three degenerate states of null orbital angular momentum $|L, m, 0\rangle$, $|C, m, 0\rangle$ and $|R, m, 0\rangle$. Following the procedure developed for the two in-line ring configuration, the total Hamiltonian of the system can be written as a direct sum of the three-state Hamiltonians with $l = 0$, plus six-state Hamiltonians (SSH) for each (m, l) combination with $l \neq 0$.

When assuming that the rings L and R are decoupled, i.e., $d_{LR} \gg d$, we can describe the system as two sets of two in-line coupled rings (C-L and C-R). By setting the free phase parameter $\phi_0 = 0$ with respect to the C-L axis, we can use Eqs. (6.6) with $\phi_0 = 0$ and $j, k = L, C$ to determine the C-L couplings, which will be real. Similarly, the relations between the C-R couplings can be obtained using Eqs. (6.6) with $\phi_0 = \Theta$ and $j, k = R, C$. Thus, by means of the geometrical parameter Θ one can manipulate the phases of the complex tunnelings. Using the $\hat{M}_y$ symmetry of the triangular configuration we find an additional relation:

$$e^{-in\Theta} J_{L,n}^{L,-n} = e^{in\Theta} J_{R,-n}^{R,n}, \tag{6.9}$$

which relates the two sets of two in-line systems C-L and C-R. Considering the full system L-C-R, one can see that the central self-coupling can be regarded as a com-

bination of the self-couplings of the two sets of systems, C-L and C-R, therefore, the
central self-coupling can be written as $J_{L,+n}^{L,-n} + J_{R,+n}^{R,-n} = J_{L,+n}^{L,-n}(1 + e^{2in\Theta})$. Note that
setting $\Theta = \pi$ in Fig. 6.3 would correspond to three in-line ring potentials for which
$J_{C,n}^{C,-n} = 2|J_{L,n}^{L,-n}|$, while $\Theta = \pi/2$, the case investigated here, corresponds to an isosce-
les triangle configuration with $d_{LR} = \sqrt{2}d$, and $J_{C,n}^{C,-n} = 0$, which is described by the
following SSH:

$$
\hat{H}_{SS}^{m,l} = \frac{\hbar}{2}
\begin{pmatrix}
0 & J_{L,n}^{L,-n} & J_{L,n}^{C,n} & J_{L,n}^{C,-n} & 0 & 0 \\
J_{L,n}^{L,-n} & 0 & J_{L,n}^{C,-n} & J_{L,n}^{C,n} & 0 & 0 \\
J_{L,n}^{C,n} & J_{L,n}^{C,-n} & 0 & 0 & J_{L,n}^{C,n} & J_{L,n}^{C,-n}e^{-i\pi} \\
J_{L,n}^{C,-n} & J_{L,n}^{C,n} & 0 & 0 & J_{L,n}^{C,-n}e^{i\pi} & J_{L,n}^{C,n} \\
0 & 0 & J_{L,n}^{C,n} & J_{L,n}^{C,-n}e^{-i\pi} & 0 & J_{L,n}^{L,-n}e^{-i\pi} \\
0 & 0 & J_{L,n}^{C,-n}e^{i\pi} & J_{L,n}^{C,n} & J_{L,n}^{L,-n}e^{i\pi} & 0
\end{pmatrix}, \quad (6.10)
$$

when taking $\phi_0 = 0$ with respect to the C-L axis. Recall that this specific choice
implies that $J_{L,n}^{L,-n}$, $J_{L,n}^{C,n}$ and $J_{L,n}^{C,-n}$ are real and $J_{R,n}^{C,-n} = J_{L,n}^{C,-n}e^{-2in\Theta}$, $J_{R,n}^{C,n} = J_{L,n}^{C,n}$ and
$J_{R,n}^{R,-n} = J_{L,n}^{L,-n}e^{-2in\Theta}$.

To numerically study the free dynamics of a single atom trapped in a three ring
configuration, Fig. 6.3, we consider three harmonic ring potentials of frequency ω cen-
tered at the vertices of an isosceles triangle with $\Theta = \pi/2$. In Fig. 6.4(a) we plot the
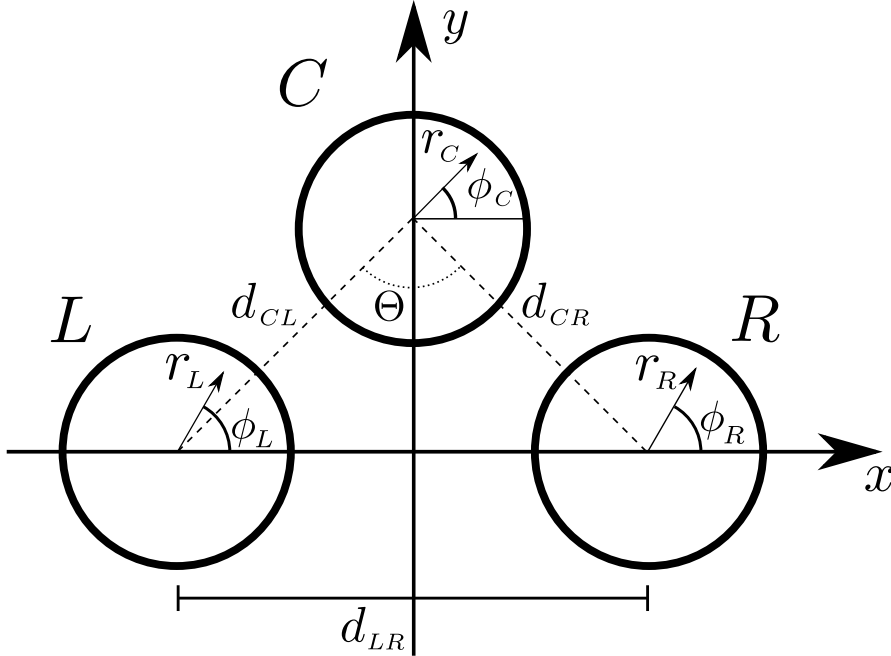
Figure 6.3: Schematic figure of three ring potentials in an isosceles triangular configu-
ration.
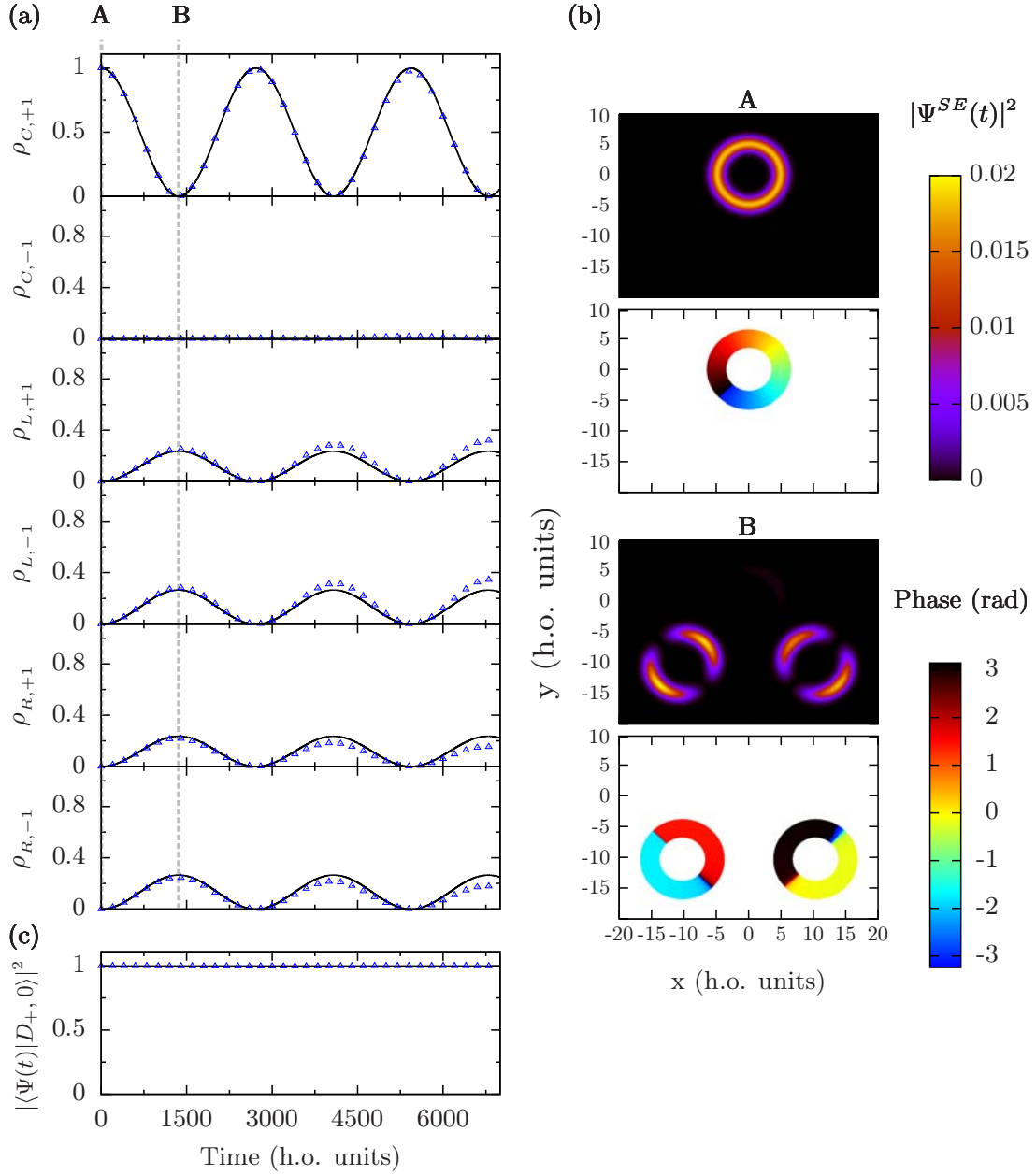
Figure 6.4: (a) Temporal evolution of the population of each angular momentum state involved in the dynamics, $\rho_{j,\pm 1} = |\langle \Psi(t)|j,0,\pm 1\rangle|^2$, where $j = C, \ L, \ R$, using the numerically integrated 2D SE (points) and the SSH (lines) when the initial state of the system is $|C,0,1\rangle$. (b) Probability density (upper plots) and phase distribution (lower plots) of the state of the system at times A and B in Fig. 6.4(a). (c) Temporal evolution of the population of the dark state $|D_+,0\rangle$ using the numerically integrated SE (points) and the SSH (lines) when the system is initialized in this state. Phase is only plotted where the probability density is non negligible. For the parameters see text.

temporal evolution of the populations of the angular momentum states $|j, 0, \pm 1\rangle$, with $j = L, C, R$, using the SSH (Eq. (6.10)) and the numerical integration of the full 2D SE, with the atom being initially in $|C, 0, 1\rangle$. We observe, that the population oscillates between states $|C, 0, 1\rangle$ and an equally weighted combination of $|L, 0, \pm 1\rangle$ and $|R, 0, \pm 1\rangle$. The values of the couplings in the SSH are $J_{L,1}^{C,1} = 1.12 \times 10^{-3}$, $J_{L,1}^{C,-1} = 1.18 \times 10^{-3}$ and $J_{L,1}^{L,-1} = -7.76 \times 10^{-5}$ and we fix $r_0 = 5$ and $d = 14.5$, in h.o. units. Note that the ratio between the self-coupling of the lateral rings and the cross-coupling tunneling amplitudes in this triangular configuration is smaller than for the two-ring case. This simply occurs since we are considering a larger distance and the exponential decay of the self-coupling is faster than for the cross-coupling (see Appendix B). Note that, as discussed after Eq. (6.9), for this particular triangular geometry the self-coupling contribution of the middle ring is completely suppressed.

Fig. 6.4(b) shows the density and phase snapshots at times A and B in Fig. 6.4(a). A corresponds to the initial state $|C, 0, 1\rangle$. In B we can see that the initial state has been fully transferred to an equally weighted combination of $|L, 0, \pm 1\rangle$ and $|R, 0, \pm 1\rangle$, as given in Eq. (6.13), which corresponds to an almost equally weighted combination of the four states $|L, 0, \pm 1\rangle$ and $|R, 0, \pm 1\rangle$.

6.2.1 Spatial dark states

In chapter 5, we already introduced the concept of spatial dark state when studying a system of three concentric ring potentials (see Eq. (5.25)). We saw that the system presented an eigenstate with no contribution of the middle ring, which allowed us to use the matter-wave analogue of the stimulated Raman adiabatic passage [76, 304] to study the transport of an ultracold atom between concentric ring traps (see Sec. 5.3.2 for further details). Here we show that the manifold of angular momentum states of sided-coupled ring potentials in a triangular configuration also present dark states in which the central ring has no contribution.

First, by taking into account that the self-coupling tunneling amplitudes of the left and right rings are one order of magnitude smaller than the cross-couplings and that by taking $\Theta = (2s + 1)\pi/2n$, with $s \in \mathbb{N}$, the central ring self-coupling of each six-state manifold is suppressed due to quantum interference, all angular momentum states within each six-state manifold are coupled only through the cross-couplings (see first row of Fig. 6.5). By performing a change of basis from the localized angular momentum states $|j, m, \pm n\rangle$ with $j = L, R, C$ to the symmetric and antisymmetric base

$$|S, m, \pm n\rangle = \frac{1}{\sqrt{2}} \left(|L, m, \pm n\rangle + |R, m, \pm n\rangle \right), \tag{6.11a}$$

$$|A, m, \pm n\rangle = \frac{1}{\sqrt{2}} \left(|L, m, \pm n\rangle - |R, m, \pm n\rangle \right), \tag{6.11b}$$
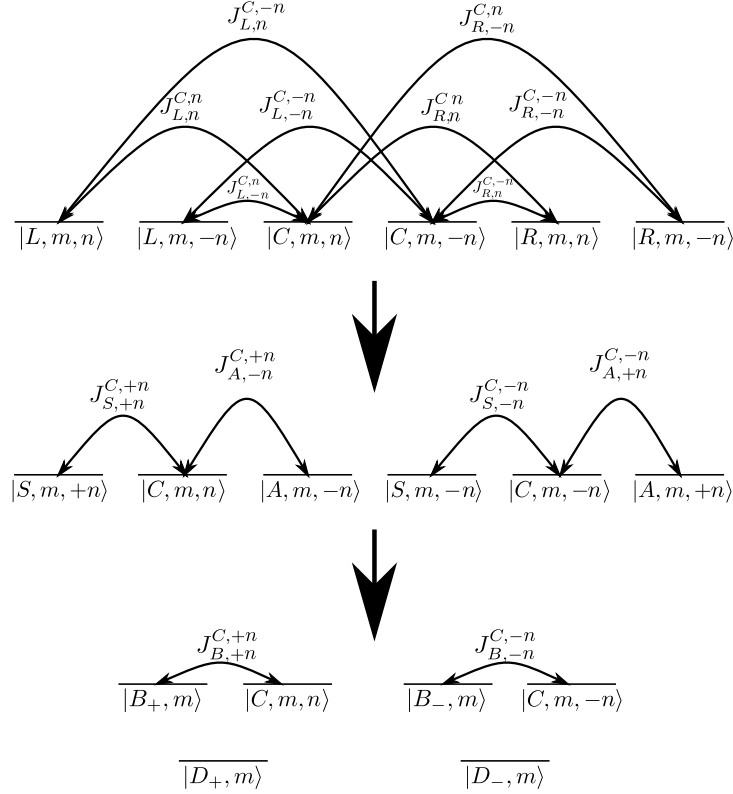
Figure 6.5: First row shows the $|j, m, \pm n\rangle$ states with $j = L, R, C$ that form the localized basis. By defining a symmetric and antisymmetric basis, Eq. (6.11), the previous manifold can be mapped two decoupled three level systems as shown in second row. Third row shows that these two three level systems can be written in a bright-dark basis obtaining two two-level systems plus two spatial dark states decoupled from the dynamics.

while keeping the $|C, m, \pm n\rangle$ states unchanged, the system can be mapped to two decoupled three level systems (second row of Fig. 6.5). These two subsystems can then be diagonalized, following a similar procedure as the one shown in Sec. 5.3.1, finding two eigenstates corresponding to spatial dark states:

$$|D_\pm, m\rangle \equiv \frac{1}{J} \left(J_{L,n}^{C,-n} |S, m, \pm n\rangle - J_{L,n}^{C,n} |A, m, \mp n\rangle \right). \tag{6.12}$$

plus two spatial bright states:

$$|B_\pm, m\rangle \equiv \frac{1}{J} \left(J_{L,n}^{C,n} |S, m, \pm n\rangle + J_{L,n}^{C,-n} |A, m, \mp n\rangle \right), \tag{6.13}$$

with $J = \sqrt{|J_{L,n}^{C,n}|^2 + |J_{L,n}^{C,-n}|^2}$. This change of basis results in two two-level systems $|C, m, n\rangle \leftrightarrow |B_+, m\rangle$ and $|C, m, -n\rangle \leftrightarrow |B_-, m\rangle$ plus two dark states completely decoupled from the dynamics (see last row of Fig. 6.5). In particular,

from these definitions, it is straightforward to check that: $\langle C, m, n|\hat{H}^{m,l}|D_+, m\rangle =$ $\langle C, m, -n|\hat{H}^{m,l}|D_-, m\rangle = 0$ and that the only remaining couplings are: $\langle C, m, n|\hat{H}^{m,l}|B_+, m\rangle = \langle C, m, -n|\hat{H}^{m,l}|B_-, m\rangle = \sqrt{2}J$.

In Fig. 6.4(c), we demonstrate the existence of spatial dark states, Eq. (6.12), by using both the SSH and the numerically integrated 2D SE. Specifically, we select as initial state $|D_+, 0\rangle$ and let the system evolve freely. We observe that the dark state remains decoupled from the dynamics and, therefore, states $|C, 0, \pm 1\rangle$ are never populated.

6.3   Conclusions

We have studied the dynamics of the angular momentum states of a single ultracold atom trapped in 2D systems of sided coupled identical ring traps. We have demonstrated that the couplings between states of different rings with different winding number are complex and that the breaking of the cylindrical symmetry induced by the presence of the neighboring rings produces a complex self-coupling between angular momentum states with opposite winding number within the same ring. Worth to highlight, the results here derived are solely based in the mirror symmetries that exhibit sided coupled cylindrically symmetric identical potentials carrying angular momentum atomic states. Thus, they could be applied not only to rings but also, for instance, to 2D identical isotropic harmonic traps (see chapter 7). On the other hand, although this study has been focused on the single atom case, it would be interesting to extend our results to BECs trapped in ring potentials to investigate the role of the non-linearity in the self and cross-coupling tunneling amplitudes. Note that, even though most of current experimental setups consider ring radii larger than those discussed here, one of the main experimental short-term goals in atomtronics is to build-up smaller rings. For instance, rings with radii of $4\,\mu$m were used to build and investigate a SQUID in [13]. The ring radius of our examples shown here would correspond to approximately $5.6\,\mu$m when using the same radial trapping frequency as in [13].

In a triangular ring configuration, we have demonstrated that the complex nature of the couplings between angular momentum states yields spatial bright and dark states that depend on the geometry of the system. Thus, these complex couplings could be used in 2D trapping configurations, e.g., 2D optical lattices, of cylindrically symmetric identical traps to manipulate the dynamics of ultracold atoms by means of the constructive (destructive) quantum interference associated with spatial bright (dark) states. Note also that the particular dynamical evolutions induced by the complex tunnelings may be inferred through density measurements in current experimental setups [185, 313, 330, 359].

Note that the two few-state models (Sec. 2.5) used to describe the dynamics of the angular momentum states of a single atom in two in-line rings and three rings in a tridiagonal configuration have given, in both cases, excellent results when compared to the numerical integration of the full 2D SE.

Single atom edge-like states via quantum interference

This chapter presents how quantum interference leads to the appearance of robust edge-like states (ELS) of a single ultracold atom trapped in an optical ribbon [77]. First, we investigate ELS within the manifold of local ground states of the sites forming the ribbon. In the same ribbon configuration, we also consider the angular momentum states of the atom for which, as we saw in chapter 6, complex tunneling amplitudes between orbital angular momentum (OAM) states appear naturally. In both cases we analyze the robustness of ELS under relative phase variations in the initial states. Finally, we also analyze other geometries where ELS can appear and explore the possibility to regard the angular momentum states within each site as synthetic dimensions.

Ultracold atoms in optical lattices provide an ideal playground for studying condensed matter phenomena in a highly controlled and tunable manner [361, 362]. In recent years, the realization of artificial gauge fields [363–372] in optical lattices has opened the possibility to explore physics of strong magnetic fields [66, 68, 373–377]. In particular, edge states predicted in the context of the quantum Hall effect have been observed both with bosons [376] and fermions [377] in 1D optical lattices extended in a synthetic dimension by taking profit of the internal atomic degrees of freedom [378]. The robustness of these states makes them useful for instance for quantum information purposes [379, 380].

Here, we propose a scheme to generate robust ELS in 2D arrangements of discrete sites without the need to create synthetic gauge fields. The method is based on the use of spatial dark states (SDS), which appear on tunneled-coupled three-site systems due to quantum interference [337] and are the basis for some matter-wave spatial adiabatic passage techniques [59], which have been investigated in chapter 5 for the transport of single atoms in systems formed by two and three cylindrically symmetric concentric

potentials. In this chapter we focus on single atoms or non-interacting Bose-Einstein condensates.

SDS can be realized using states carrying OAM $l \in \mathbb{Z}$ (see chapter 6, Sec. 6.2). Particularly, here we focus on the use of states with $l = 0$ and $l = 1$. When using the manifold of local ground states, $l = 0$, quantum interference is based on the phase differences between the local states of the sites, allowing to create ELS in a large variety of geometrical configurations. These arrangements of sites could be realized using, for instance, painting potentials [183, 185, 187, 309] or spatial light modulators [381, 382]. When considering states with one unit of angular momentum, $l = 1$, quantum interference is produced by the complex character of the tunneling amplitudes, whose phases are modulated by the relative orientation between sites [63] (chapter 6). The manifold of $l = 1$ states [383] offers the additional possibility of using the winding number as a synthetic dimension. This could open the door to the quantum simulation of non-trivial topologies [384, 385], with the advantage that complex tunneling amplitudes appear naturally.

In Sec. 7.1 we introduce the physical system investigated in this chapter, a 2D optical ribbon. Section 7.2 is devoted to the generation of ELS using the local ground states of the sites forming the ribbon. The quantum interference conditions required to implement ELS with $l = 0$ are very flexible, thus, we also explore other geometrical configurations that could hold ELS. Section 7.3 presents an alternative method for the implementation of ELS; the use of angular momentum states for which different quantum interference conditions are required. Moreover, we also discuss how angular momentum may be associated to a synthetic dimension, which may open the possibility to use the system investigated here as a quantum simulator of certain 3D solid state systems that exhibit complex tunneling. Finally in Sec. 7.4 we present the conclusions.

7.1 Two dimensional optical ribbon

We consider a 2D ribbon constructed by placing side by side five-site cells consisting of a square with a site at each corner plus a central site laying at a distance d from the other four (Fig. 7.1). Thus, a lattice with n cells has a total of $N = 3n + 2$ sites. We assume that sites are formed by harmonic traps of identical frequency ω. Considering that sites are separated enough, their local eigenfunctions can be used as a basis of the total Hilbert space associated to the lattice (see Sec. 2.5 for further details). Moreover, the total set of eigenstates can be split into manifolds of total OAM l, each containing $N \cdot (l + 1)$ degenerate states corresponding to the eigenstates with z component of the OAM $m = -l, -l + 2, ..., l - 2, l$ in each site. Therefore, under this assumption the dynamics of the system can be studied separately for each OAM manifold, leading to a total Hamiltonian

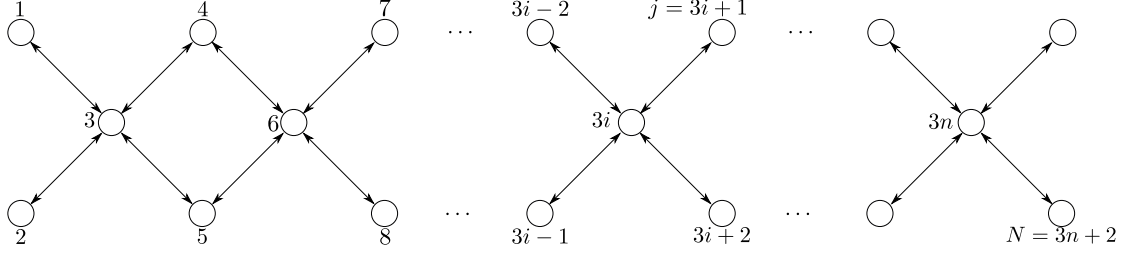$$\hat{H}_{\text{ribbon}} = \sum_{l=0}^{\infty} \hat{H}_l, \tag{7.1}$$

Figure 7.1: Sketch of the considered 2D optical ribbon, with circles representing its sites. The index $i = 1, ..., n$ refers to individual cells, which are squares with one site laying at each of their corners plus a central site placed at an equal distance d from the outer ones. The sites are labelled with the index $j = 1, ..., N$; with $N = 3n + 2$. As indicated by the double arrows, we only consider the central sites to be tunneled-coupled to their four nearest neighbour sites.

where $\hat{H}_l$ is a few-state Hamiltonian describing the tunneling dynamics within the manifold of OAM l.

7.2 Edge-like states within the manifold of local ground states

Let us consider the $l = 0$ manifold whose basis is formed by the set of local ground states of each site, which we denote as $\{|j\rangle\}$, where the index $j = 1, ..., N$ labels the sites according to Fig. 7.1 and where $\langle \vec{r}|j\rangle \approx \Psi(r_j)$ corresponds to the wavefunction spatial distribution of the ground state of the jth site. In this situation, tunneling couplings are always real and their magnitude only depends on the separation between sites, typically showing a fast decay as it is increased. Thus, we can assume that the central site of each cell is only tunneled-coupled to its four nearest neighbours, with a tunneling rate J. Introducing the tunneling operators $\hat{a}_k^\dagger \hat{a}_j |h\rangle = |k\rangle \, \delta_{jh}$, where k, j, h are labels denoting sites, the Hamiltonian for the $l = 0$ manifold of a ribbon with n cells can be written as

$$\hat{H}_0 = -\hbar J \sum_{i=1}^{n} \left[(\hat{a}_{3i-2}^\dagger \hat{a}_{3i} + \hat{a}_{3i-1}^\dagger \hat{a}_{3i} + \hat{a}_{3i+1}^\dagger \hat{a}_{3i} + \hat{a}_{3i+2}^\dagger \hat{a}_{3i}) + h.c. \right]. \qquad (7.2)$$

Before deriving the general expressions of the ELS existing in a ribbon, we first consider a reduced system of three sites L, C, R (from left, central and right), with their ground states $|L\rangle$ and $|R\rangle$ equally coupled to $|C\rangle$ and decoupled between each other. This system has an eigenstate of 0 energy $|D\rangle = \frac{1}{\sqrt{2}}(|L\rangle + e^{i\pi}|R\rangle)$, the SDS (equivalent to the one obtained in the three concentric ring configuration derived in Sec. 5.3.1), which is decoupled from the state $|C\rangle$.
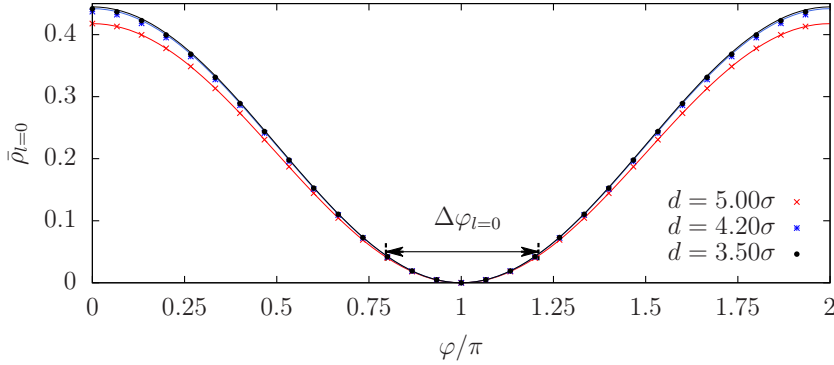
Figure 7.2: Average population of the central sites of a two-cell ribbon over a time $T = 1000\omega^{-1}$ when choosing as initial state $|\Psi(\varphi)\rangle_{l=0}$. Solid lines and points correspond to the results obtained with the few-state models and full numerical integration of the 2D Schrödinger equation, respectively. The horizontal double arrow indicates the range of values of φ for which the average population remains under 0.05.

In a ribbon of n cells, ELS can be found by building different combinations of the previous three-site SDS with population only on the edge sites. Thus, after setting them as initial states, the central sites $\{|3i\rangle\}$ $(i = 1, ..., n)$ will remain unpopulated along the time evolution. For instance, in a single five-site cell there are 3 independent possibilities for such combinations, which correspond to the different ways in which the wavefunction at two of the outer sites can have a π phase difference with respect to the other two. In general, for n cells there are $2^n + 1$ possible ELS with equal population in the external sites,

$$|D_k\rangle_{l=0} = \frac{1}{\sqrt{2(n+1)}}(|1\rangle + e^{i\pi}|2\rangle +$$

$$\sum_{j=1}^{n}(-1)^{B_k^j(n)}(|3j+1\rangle + e^{i\pi}|3j+2\rangle)); \qquad k = 0, ..., 2^n - 1$$

$$|D_{2^n}\rangle_{l=0} = \frac{1}{\sqrt{2(n+1)}}\sum_{j=0}^{n} e^{j \cdot i\pi}(|3j+1\rangle + |3j+2\rangle), \qquad (7.3)$$

where $B_k^j(n)$ is the jth digit (starting from the left) of the binary representation of k using a total of n digits. For instance, $B_7(n = 4) = 0111$, $B_7^1(n = 4) = 0$ and $B_7^2(n = 4) = 1$. It can be checked that all the states in Eq. (7.3) are eigenstates of $\hat{H}_0$ with 0 energy.

To numerically check the existence of the ELS predicted with the few-state model, we consider the $l = 0$ manifold of a ribbon of 2 cells with the following trial state

$$|\Psi(\varphi)\rangle_{l=0} = \frac{1}{\sqrt{6}}\sum_{j=0}^{2} |3j+1\rangle + e^{i\varphi}|3j+2\rangle \qquad (7.4)$$

(a)

(b)
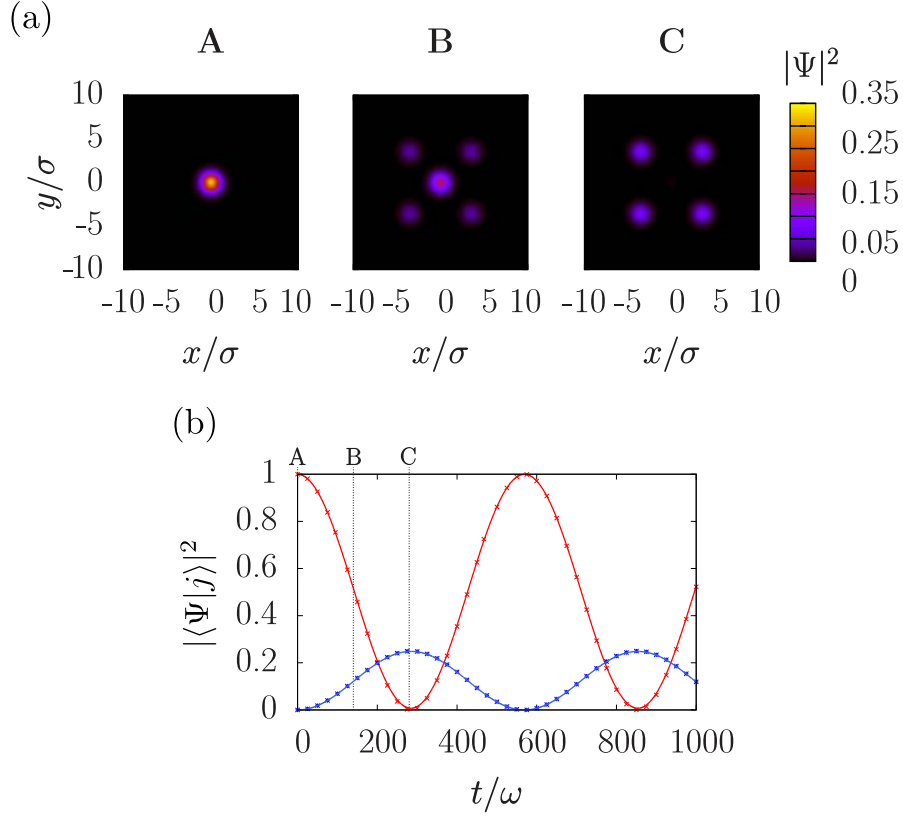
Figure 7.3: (a) Density plots of the atomic wavefunction in a single cell of the considered ribbon when: the atom is located on the central site (A), some population has been transferred to the outer sites (B) and the central site is unpopulated (C). The separation between tunneled-coupled sites is $d = 5\sigma$. (b) Time evolution of the populations of the central (red) and outer (blue) sites of the cell during the Rabi-type oscillations. Continuous lines correspond to the full integration of the Schrödinger equation and dots to the results obtained with the few-state Hamiltonian Eq. (7.2).

as initial state. Its time evolution is found both with the few-state model and by direct integration of the 2D Schrödinger equation. We then compute the average value of the populations of the central sites over the total time T as a function of the relative phase φ:

$$\bar{\rho}_{l=0}(\varphi) = \sum_{i=1,2} \frac{1}{T} \int_0^T dt \left| \left\langle 3i \left| e^{-i\hat{H}t/\hbar} \right| \Psi(\varphi) \right\rangle_{l=0} \right|^2 . \tag{7.5}$$

In Fig. 7.2 we explore the limits of validity of the few-state model by performing a comparison of the average population, Eq. (7.5), calculated with the model and by numerically integrating the Schrödinger equation. We vary the relative phase between the localized states of the sites forming the ribbon (Eq. (7.4)) and the distance between sites d, in units of $\sigma = \sqrt{\hbar/m\omega}$ (m is the mass of the atom). As predicted by the model,

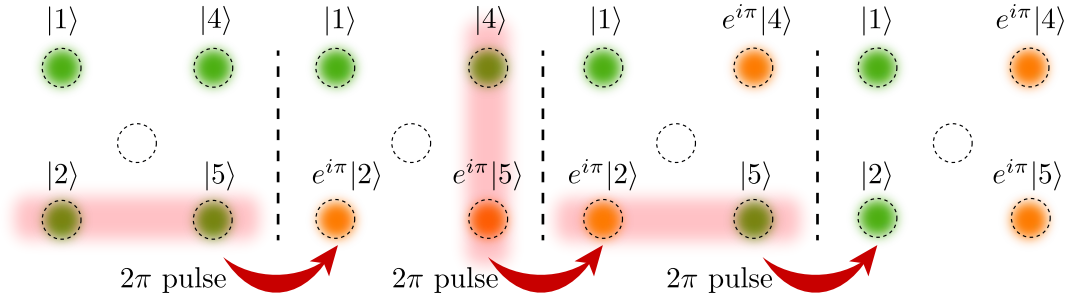Figure 7.4: Sketch showing how by illuminating two sites with a pulse of area 2π, it is possible to induce π phase changes on their local functions. In the leftmost sketch this is done at the instant C of Fig. 7.3(b), giving rise to an ELS. The other panels show how sequential application of pulses allows to switch between the different ELS.

the average population of the central sites has a broad resonance at $\varphi = \pi$, for which the trial state is $|D_0\rangle_{l=0}$. For a range of phase differences $\Delta\varphi_{l=0} = 0.4\pi$ around the minimum, the average population of the central sites remains below 0.05. Thus, we can conclude that ELS are robust against variations of these relative phases in the initial state. The agreement between the model and the numerical integration is excellent for all the values of d that we have considered. For $d < 2\sigma$, the sites become close enough that their local eigenfunctions have large overlaps, and the few-state description breaks down.

In order to test the theory introduced in this section, in Fig. 7.3 we study an example where an atom in a single ribbon cell is prepared in one of the possible ELS of the ribbon, Eq. (7.3). We present a possible experimental implementation of these states by starting with only the central site populated Fig. 7.3 (A). By letting the system evolve freely, the atom undergoes Rabi-type oscillations in which the population is transferred equally and with the same phase to the four outer sites Fig. 7.3 (B). When all the population has been transferred to the outer sites (C), a laser pulse of area 2π is applied, inducing a π change of phase in the states localized in all the sites of either the upper or the lower row, obtaining an ELS that will not populate the central site. First panel of Fig. 7.4 shows the schematic representation of this last step. Moreover, once the system has been prepared in this initial ELS, by applying localized 2π pulses in one column or row of the ribbon it is possible to induce π phase changes in the states localized in any desired pair of sites, and thus switch from one ELS to another (see examples in the three right panels of Fig. 7.4). Thus, these phase-change processes allow to explore the whole $l = 0$ ELS subspace. Also, by applying π pulses to pairs of sites, one could create equally weighted superpositions of ELS.

ELS can also be implemented in more complex geometries. An example, corresponding to a tilted square lattice, is shown in Fig. 7.7 (a). By populating equally all

the edge sites but the four corners and setting π phase differences between local states of adjacent edge sites, quantum interference would prevent population transfer to any tunneled-coupled site of the total lattice and, an ELS would be created.

7.3 Edge-like states within the manifold of angular momentum states

We now consider the $l = 1$ manifold of the 2D ribbon shown in Fig. 7.1. The basis of this manifold is formed by the set of first excited eigenstates of each site with winding number $m = \pm 1$, denoted as $\{|j, +\rangle, |j, -\rangle\}$. Their wavefunctions are of the form $\langle \vec{r}|j, \pm\rangle \sim \Psi(r_j)e^{\pm i(\phi_j - \phi_0)}$, where (r_j, ϕ_j) are the polar coordinates with origin at the position of the jth site and ϕ_0 is a free phase parameter. Because of the angular dependence of the wavefunctions, the couplings between the different states depend both on the distance between sites and on their relative orientation, and can in general take complex values. Further details on the complex nature of the couplings can be found in chapter 6, where an equivalent system using ring potentials has been studied. By using symmetry considerations, we can show that there are only three independent coupling rates: a self-coupling rate between the two eigenstates of a site, $J_1 \sim \left|\left\langle j, \pm \left| \hat{H} \right| j, \mp \right\rangle\right|$, and two cross-coupling rates between the eigenstates of different sites with equal or different winding number, $J_2 \sim \left|\left\langle j, \pm \left| \hat{H} \right| k, \pm \right\rangle\right|$ and $J_3 \sim \left|\left\langle j, \pm \left| \hat{H} \right| k, \mp \right\rangle\right|$, respectively. The phases of the complex tunneling amplitudes depend on ϕ_0 and the winding numbers of the states involved in the coupling. As for $l = 0$, the coupling rates decay fast with the inter-site separation (see Fig. B.2 in appendix B), so again we will consider that only the central sites are tunneled-coupled to their neighbors. By setting $\phi_0 = -\pi/4$, all the couplings between the sites $3i - 2 \leftrightarrow 3i$ and $3i \leftrightarrow 3i + 2$ are real, whereas between the sites $3i - 1 \leftrightarrow 3i$ and $3i \leftrightarrow 3i + 1$ the couplings involving winding number change acquire π phases (see Sec. 6.2 where these phases have been studied as a function of the apex angle of an isosceles triangular configuration of ring potentials). By defining the tunneling operators $\hat{a}_{j,\alpha''}^\dagger \hat{a}_{k,\alpha'} |h, \alpha\rangle = |j, \alpha''\rangle \delta_{kh}\delta_{\alpha'\alpha}$, where $\alpha = \pm$ is the winding number, the Hamiltonian of a ribbon with n cells reads

$$
\begin{aligned}
\hat{H}_1 = &-\hbar \sum_{i=1}^{n} \sum_{\alpha,\alpha'=\pm 1} (U_1)_{\alpha\alpha'}(\hat{a}_{3i,\alpha}^\dagger \hat{a}_{3i-1,\alpha'} + \hat{a}_{3i,\alpha}^\dagger \hat{a}_{3i+1,\alpha'}) \\
&-\hbar \sum_{i=1}^{n} \sum_{\alpha,\alpha'=\pm 1} (U_2)_{\alpha\alpha'}(\hat{a}_{3i,\alpha}^\dagger \hat{a}_{3i-2,\alpha'} + \hat{a}_{3i,\alpha}^\dagger \hat{a}_{3i+2,\alpha'}) \\
&-\hbar \sum_{\alpha,\alpha'} (S_1)_{\alpha\alpha'}(\hat{a}_{1,\alpha}^\dagger \hat{a}_{1,\alpha'} + \hat{a}_{N-1,\alpha}^\dagger \hat{a}_{N-1,\alpha'}) \\
&-\hbar \sum_{\alpha,\alpha'} (S_2)_{\alpha\alpha'}(\hat{a}_{2,\alpha}^\dagger \hat{a}_{2,\alpha'} + \hat{a}_{N,\alpha}^\dagger \hat{a}_{N,\alpha'}) + h.c.,
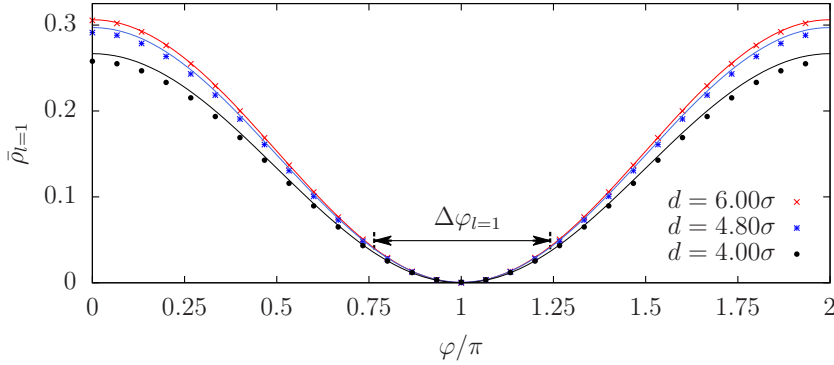\end{aligned}
\tag{7.6}
$$

Figure 7.5: Average population of the central sites of a two-cell ribbon over a time $T = 1000\omega^{-1}$ when choosing as initial state $|\Psi(\varphi)\rangle_{l=1}$. Solid lines and points correspond to the results obtained with the few-state models and full numerical integration of the 2D Schrödinger equation, respectively. The horizontal double arrow indicates the range of values of φ for which the average population remains under 0.05.

with coupling matrices

$$
\begin{aligned}
U_1 &= \begin{pmatrix} J_2 & J_3 e^{-i\pi} \\ J_3 e^{i\pi} & J_2 \end{pmatrix}; & U_2 &= \begin{pmatrix} J_2 & J_3 \\ J_3 & J_2 \end{pmatrix}; \\
S_1 &= \begin{pmatrix} 0 & J_1 \\ J_1 & 0 \end{pmatrix}; & S_2 &= \begin{pmatrix} 0 & J_1 e^{-i\pi} \\ J_1 e^{i\pi} & 0 \end{pmatrix}.
\end{aligned}
\tag{7.7}
$$

Note that the complex number sum rule for the contributions to the self-coupling (see Sec. 6.2) makes this term vanish at all the sites but the four corners of the ribbon. In addition, $|J_2| \approx |J_3|$ and $|J_1| \ll |J_2|, |J_3|$, so in a first approximation the self-couplings can be neglected (see appendix B). Within this approximation, a system of three in-line sites L, C and R (L and R equally separated from C) with $l = 1$ local eigenstates $|L, \pm\rangle$, $|C, \pm\rangle$ and $|R, \pm\rangle$ have two SDS of 0 energy, $|D+\rangle = \frac{1}{2}(|L, +\rangle + |L, -\rangle - |R, +\rangle - |R, -\rangle)$ and $|D-\rangle = \frac{1}{2}(|L, +\rangle - |L, -\rangle - |R, +\rangle + |R, -\rangle)$. Note that these SDS for the in-line configuration ($\phi_0 = \pi$) do not coincide with the ones considered in chapter 6 for the triangular configuration ($\phi_0 = \pi/2$). On a ribbon of n cells, ELS can be implemented by setting the SDS $|D\pm\rangle$ along the lines $3i - 2 \leftrightarrow 3i \leftrightarrow 3i + 2$ and $3i - 1 \leftrightarrow 3i \leftrightarrow 3i + 1$, that is, setting three in-line-sites SDS along the diagonals and contradiagonals of the ribbon. Among the many possibilities to do so, two are particularly interesting because the orientation of the nodal lines of the wavefunction gives rise to global chirality, as shown in Fig. 7.6. These two ELS read
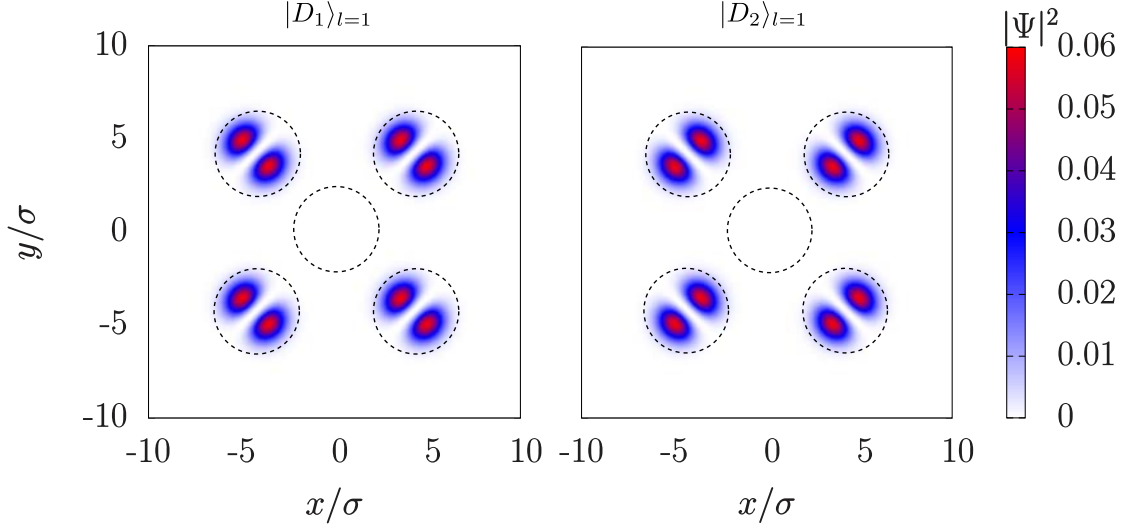
Figure 7.6: Density profile of the two ELS Eq. (7.8) of the $l = 1$ manifold restricted to one cell of a ribbon with $d = 6\sigma$. For each state, the wavefunction has a nodal line with the same orientation at all sites, giving rise to global chirality.

$$|D_1\rangle_{l=1} = \frac{1}{\sqrt{4(n+1)}} \sum_{j=0}^{n} (|3j+1,+\rangle + |3j+1,-\rangle) + e^{i\pi}(|3j+2,+\rangle + |3j+2,-\rangle)$$

(7.8a)

$$|D_2\rangle_{l=1} = \frac{1}{\sqrt{4(n+1)}} \sum_{j=0}^{n} (|3j+1,+\rangle - |3j+1,-\rangle) + e^{i\pi}(|3j+2,+\rangle - |3j+2,-\rangle).$$

(7.8b)

To test these ELS, we consider the following trial state in a ribbon of 2 cells

$$|\Psi(\varphi)\rangle_{l=1} = \frac{1}{\sqrt{12}} \sum_{j=0}^{2} (|3j+1,+\rangle |3j+1,-\rangle) + e^{i\varphi}(|3j+2,+\rangle + |3j+2,-\rangle) \quad (7.9)$$

and compute the average population of the central-site states $\bar{\rho}_{l=1}(\varphi)$ (see Fig. 7.5). As expected, $\bar{\rho}_{l=1}(\varphi)$ has a resonance at $\varphi = \pi$, where it becomes 0, whose width is even larger than in the $l = 0$ case: the average population of the central sites remains under 0.05 for $\Delta\varphi_{l=1} = 0.5\pi$. Thus, the ELS constructed from combinations of $l = 1$ SDS are also robust. The few-state model starts breaking down at longer inter-site separations than in the $l = 0$ case because the wavefunctions of the first excited states are more extended than the ground state ones. Note that the numerical simulations account for the self-coupling terms neglected on the derivation of the ELS expressions. Thus, although the states shown in Eq. (7.8) are eigenstates of $\hat{H}_1$ only for $J_1 = 0$, they
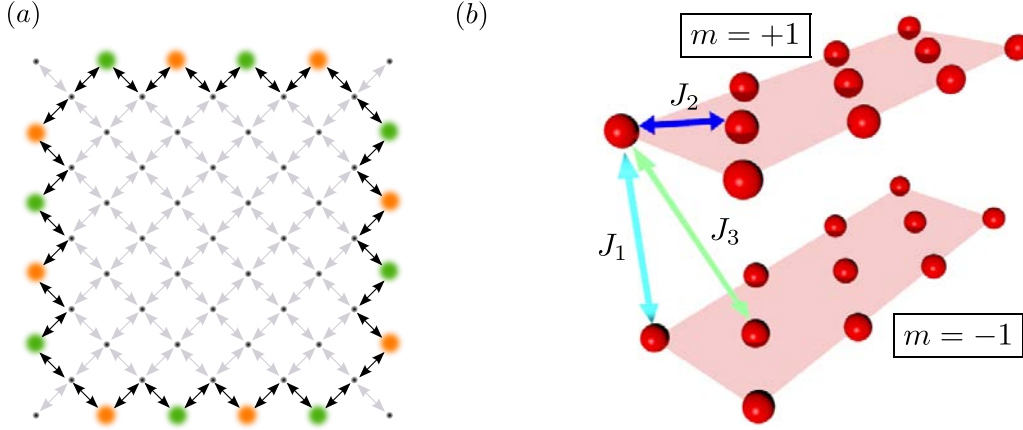
Figure 7.7: (a) ELS constructed from SDS of $l = 0$ on a tilted square lattice, with all edge sites but the corners equally populated. As indicated by the alternating orange and green colourings, the atomic states at adjacent sites have π relative phases. Double arrows indicate nearest neighbour tunneling couplings, with the ones involved in the SDS highlighted in black. (b) Schematics of the extension of the optical ribbon into the synthetic dimension given by the winding number in the $l = 1$ case. Each red dot can host only one state, and tunneling-coupling (represented by the double arrows) can occur through sites in the same or different winding number planes.

work well as ELS in the sense that they do not populate the central sites for $J_1 \neq 0$. The fact that they are not actual eigenstates is manifested in small oscillations of the populations of the occupied edge sites. Nonetheless, we have checked that in the longest time scale of the system, typically $\frac{2\pi}{J_1} \sim 10^4 \omega^{-1}$, these oscillations decay as the number of cells in the ribbon increases. Hence, they may be considered as by finite-size effects due to the corners of the ribbon, with no relevance in the limit of large number of cells.

So far, we have considered the winding number associated to the OAM as a degree of freedom that increases the number of states per site. However, one could also regard it as a synthetic dimension, see Fig. 7.7 (b). In this picture, the 2D ribbon splits into two layers, each containing only states with a well-defined winding number. Within each layer, the central sites are connected to their nearest neighbours through J_2 cross-couplings. The two layers are connected by cross-couplings $\pm J_3$ between central and edge sites, and at the four corners there are vertical connections between edge sites corresponding to self-couplings $\pm J_1$. This approach could open the possibility of using 2D optical lattices to simulate three-dimensional systems, in which the high variety of possible closed paths could yield non-abelian artificial gauge fields [371].

7.4   Conclusions

In this work we have shown that quantum interference effects can lead to the generation of robust single atom ELS in arbitrarily large optical ribbons. These ELS may be built within the manifolds of local eigenstates with total OAM $l = 0$ or $l = 1$ and are based on three-site SDS. We have discussed that when using the local ground states of the sites, i.e., $l = 0$, the different possible ELS existing in a ribbon could be coupled with laser pulses, which would allow to induce oscillations between global eigenstates of the ribbon. Taking advantage of the versatility of three-site SDS, we have also explored the possibility to implement ELS in other geometries. When considering the manifold of angular momentum states, $l = 1$, we have seen that a large variety of ELS can also be constructed and, some configurations can present interesting features such as global chirality in the system. We have also analyzed the robustness of ELS against variations of the relative phase within the three-site SDS and for different separations between the localized sites, finding that ELS are robust. Finally, we have briefly discussed that the winding number can be regarded as a synthetic dimension, which could lead to quantum-simulate exotic three-dimensional lattices or synthetic gauge fields.

CHAPTER 8

Conclusions

In this last chapter we will summarize the main results presented in this thesis and outline possible future perspectives.

Tunneling, being one of the paradigms of Quantum Mechanics, has been considered as the common thread that binds the presented work together. We have investigated tunneling-related phenomena in a variety of ultracold atomic systems, including matter-wave bright solitons in 1D Bose–Einstein condensates (BECs), two component BECs (TCBECS) in a single harmonic trap and single atoms in multiple connected traps. Before delving into the details of our research, in chapter 2 we have reviewed some preliminary concepts required to describe the physical systems considered throughout the thesis. Specifically, we have introduced the Gross–Pitaevskii equation (GPE), the Thomas–Fermi approximation (TFA), the two-component Gross–Pitaevskii equation (TCGPE), the matter-wave soliton solutions of the 1D GPE, the trapping techniques available for ultracold neutral atoms and the derivation of the few-state model.

In chapter 3, we have proposed a soliton-based matter-wave interferometer in which the splitting mechanism is given by the tunneling of a matter-wave bright soliton through a finite width barrier. Specifically, the interferometer consists of a harmonic potential trap with a Rosen–Morse potential barrier located at its center with which the matter-wave soliton, created in an attractive 1D BEC, collides and splits into two. Then, the two split solitons undergo a dipole oscillation in the harmonic potential to finally recombine at the position of the barrier [48]. The novel element of this interferometric scheme is that the number of particles at the outputs gives a measure of the relative phase between the two arms of the interferometer. We have first focused on analyzing the splitting mechanism. We have characterized the area of the barrier required to obtain a 50-50 splitting, the phase difference acquired during the splitting process and the

velocity of the split solitons. Our results have shown that the phase difference acquired by the two split solitons strongly depends on the width of the barrier, the nonlinearity and the velocity of the incident soliton and, that only for extremely thin barriers and low nonlinearities one recovers the typically assumed $\pi/2$ relative phase between transmitted and reflected matter-waves. In addition, we have seen that the velocities of the split solitons are different, and in general, the reflected soliton is slower. This is particularly relevant, as it affects the relative phase that the solitons accumulate over time. Finally, the full interferometric sequence has been tested by imprinting a phase on one of its arms and showing that the number of particles at the outputs depends on this imprinted phase.

Next we consider TCBECs. These systems are formed by two BECs coupled through a non-coherent collisional term, and they exhibit two different phases, the immiscible and the miscible one. Both are clearly delimited by the ratio of the inter- and intra-species interactions in spatially homogeneous systems. However, in trapped systems the frontier between the two phases is no longer obvious. In chapter 4, we have focused on the miscible phase, where no previous analytical studies reproducing the density profile around the boundaries of TCBECs existed. The aim of this chapter has been to obtain an analytical formulation of these boundaries in TCBECs trapped in isotropic harmonic potentials of different dimensionalities within the mean field approximation. This analytical formulation is important in estimating, for instance, the tunneling rate across a potential barrier or between tunnel-coupled potentials. Note that, around these regions the density is very low and therefore, the well known TFA is no longer valid and other approaches are required. Specifically, our analytical procedure consists on deriving universal equations that provide a good estimation of the density profile around each boundary [173], softening the sharp edges found in the TFA. Such analytical approach has several possible extensions, for instance, we could define an analogue of the healing length for TCBECs which could be useful for studies of instabilities, or we could apply this method to determine the density at the boundaries in more involving potential trap configurations. In addition, in chapter 4, we have also studied the Thomas–Fermi (TF) solution in 1D, 2D and 3D for miscible TCBECs trapped in isotropic harmonic potentials. These TF solutions have allowed us to analytically delimit the frontier separating the coexisting and spatially separated regimes within the miscible phase. In this context, we have found that the spatially separated regime has no analytical solution in 1D and 3D. For those cases, we have presented a method that reduces the complexity of the numerical problem to a single numerical inversion instead of solving two coupled equations.

Whilst in previous chapters we have considered single trap systems, in chapters 5, 6 and 7 we have studied dynamics of single atoms trapped in 2D tunnel-coupled potentials. In all the cases investigated in these three chapters we have derived few-state models in order to describe the dynamics of the system using a reduced set of eigenstates of the local potentials and all the results have been compared with numerical simulations of

the full 2D Schrödinger equation (SE), obtaining an excellent agreement.

Our first study in chapter 5 was meant to introduce robust and efficient techniques for the transport and loading of single ultracold atoms between cylindrically symmetric concentric potentials using spatial adiabatic passage (SAP) processes [59, 74]. First, we have proposed a mechanism to load and transport a single atom trapped in two cylindrically symmetric concentric potentials using the matter-wave analogue of the rapid adiabatic passage (RAP) technique [75], a technique that consists on adiabatically following one of the eigenstates of the system. The loading is performed from an inner harmonic potential to a concentric outer ring, and the transport occurs between two concentric ring potentials. To perform the adiabatic following, in both cases we have tunned appropriately the frequency and radius of the outer ring obtaining a robust full population transfer from the localized ground state of the inner potential to the localized ground state of the outer one. We have demonstrated that matter-wave RAP-like processes are robust under parameter deviations obtaining a 99% population transfer over a 15% deviation from the optimal minimum radial distance between rings in the two concentric ring configuration. In this chapter 5, we have also investigated the matter-wave analogue of the stimulated Raman adiabatic passage (STIRAP) [76, 304] for the transport between the innermost and the outermost rings in a system of three concentric ring potentials. We have shown that, using the few-state model approach, a spatial dark state (SDS) appears as an eigenstate of the system, with no contribution from the localized ground state of the middle ring. Thus, it only depends on the localized eigenstates of the inner and outer rings. Therefore, by adiabatically following the SDS, one can transfer an atom from the innermost ring to the outermost one with a very small probability to occupy the central ring during the process. We have also checked that this STIRAP-like protocol can be applied successfully to transport states carrying orbital angular momentum (OAM), with potential applications in the field of Atomtronics. When using angular momentum states, we have noted that, for equal total times, the fidelity of the transport using the STIRAP-like process is slightly reduced when compared to the fidelity obtained with the localized ground states, from 99% using the localized ground states to 97%. This reduction in fidelity can be explained by recalling that the local angular momentum eigenenergies of the rings have a dependence on the ring radius. In this regard, it would be interesting to characterize the adiabaticity condition of the matter-wave STIRAP in the limit of large angular momenta.

In chapter 6, we have studied the dynamics of single utracold atoms in ring potentials, but in this case, instead of considering concentric rings we have explored the dynamics of sided-coupled ring potentials. We have seen that this configuration brings to light new and interesting features appearing when using the manifold of states carrying orbital angular momentum. By using geometrical symmetries, we have shown that complex tunneling amplitudes exist between subsystem eigenstates with different winding number [63], which represents an alternative method to the generation of complex tunneling amplitudes with respect to techniques that use external means such as shaking an optical

lattice [61] or using RF and Raman fields coupled to the atoms [62]. We have also observed that, due to the breaking of cylindrical symmetry, a complex self-coupling, which couples angular momentum states within the same ring, arises. The dynamics of these tunnel-coupled ring potentials appear to be rather complicated, but using few-state models we have been able to decrypt it in terms of the localized eigenstates of the local traps. In particular, we have studied two different sided-coupled configurations, two inline ring potentials and three rings forming an isosceles triangle. In the triangular configuration, contrary to the two inline ring case, complex tunneling amplitudes play a crucial role in the dynamics. We have already pointed out that the complex nature of the tunnelings is related to the geometry. In particular, we have demonstrated that the self-coupling of the middle ring can be completely suppressed for certain configurations as a consequence of quantum interference. In addition, by using a change of basis we have shown that the manifold of six states associated to the angular momentum states with orbital angular momentum (OAM) $l = 1$ can be mapped to two two-level systems plus two SDS decoupled from the dynamics, which can be used to manipulate the transport of orbital angular momentum states via quantum interference. The natural extension of this work is to investigate the role of the nonlinearity when using the angular momentum states of sided-coupled 2D trapped BECs and how tunneling affects the persistent currents appearing in these systems.

In previous chapters, we have seen SDS appearing in different configurations of tunnel-coupled potentials. In chapter 7, we have explored the generation of single-atom robust edge-like states (ELS) as combinations of SDS in an optical ribbon, a scheme in which ELS are generated without the need to create synthetic gauge fields. In particular, we have demonstrated the existence of ELS within the manifolds of local eigenstates with total OAM $l = 0$ or $l = 1$ [77]. First, for the $l = 0$ case we have shown that multiple ELS consisting on different combinations of phase differences of π between sites can be implemented and, we have proposed a possible experimental implementation by introducing phase differences between sites of different rows of the ribbon using laser pulses. In addition, we have also presented a mechanism to switch from one ELS to another or to create equally weighted superpositions of different ELS. We have also found an interesting feature when using the manifold of states with OAM $l = 1$; some specific configurations of SDS give rise to ELS with global chirality. To conclude our analysis of the ELS with OAM $l = 0$ and $l = 1$ in a ribbon, we have studied their robustness against variations of the initial relative phase between sites, showing that in both cases for a range of phase differences $\Delta\varphi_{l=1} = 0.5\pi$ the average population of the central sites remains below 0.05 in an optical ribbon of two cells. Moreover, these ELS can be extended to other geometries as we have briefly discussed at the end of the chapter. In addition, the existence of ELS with OAM opens the possibility to regard the winding number associated to the angular momentum as a synthetic dimension [378] opening the possibility to simulate 3D systems with 2D ribbons. The next step in this research line would be to include nonlinearity and explore if ELS also exist in the system.

In conclusion, in this thesis we have investigated several ultracold atom systems where tunneling-related phenomena was present using numerical simulations, analytical approaches and semi-analytical models. In all cases we have checked the feasibility of our proposals by taking into account the experimental parameters available in current experiments. This work aims at contributing to the fields of Atomtronics and Quantum technologies, either with applications such as the interferometric proposal and the SAP techniques presented here, or with fundamental studies, like the generation of complex tunnelings in sided-coupled systems and the creation of ELS in ribbons.

Appendices

Transmission coefficients of the delta, square and Rosen–Morse potential barriers

We compare the analytical transmission coefficients of the delta, square and Rosen–Morse potential barriers for an incident free particle described by $\Psi(z) = \frac{1}{\sqrt{L}}e^{ikz}$ where $k = p/\hbar$ is the wave number, p is the linear momentum and L is the normalization length.

The analytical linear transmission coefficients are:

$$T_{RM} = \frac{\sinh^2\left(\sigma\pi\sqrt{\frac{2mE_k^v}{\hbar^2}}\right)}{\text{sech}^2\left(\sigma\pi\sqrt{\frac{2mE_k^v}{\hbar^2}}\right) + \cosh^2\left(\frac{\pi}{2}\sqrt{\frac{8mV_b\sigma^2}{\hbar^2}-1}\right)} \tag{A.1}$$

for a Rosen–Morse potential barrier of strength V_b and width σ when $\frac{8mV_b\sigma^2}{\hbar^2} > 1$ [283],

$$T_{SQ} = \frac{1}{1 + \frac{V_{SQ}^2 \sinh^2(\sigma\sqrt{2m(E_k^v-V_{SQ})/\hbar^2})}{4E_k^v(V_{SQ}-E_k^v)}} \tag{A.2}$$

for a square potential barrier given by:

$$V_{SQ} = \begin{cases} V_{SQ} & \text{for } |z| < \sigma/2 \\ 0 & \text{for } |z| > \sigma/2 \end{cases}, \tag{A.3}$$

with V_{SQ} and σ being the strength and width of the barrier, and

$$T_D = \frac{1}{1 + \frac{mV_D^2}{2\hbar^2 E_k^v}} \qquad (A.4)$$

for a delta barrier $V_D = V_D \delta(z)$.

A comparison between the three transmission coefficients, T_{SQ}, T_D and T_{RM} for different input kinetic energies E_k^v, is given in Fig. A.1. The potential barrier heights for the square and Rosen-Morse barriers are chosen in such a way that for small widths, σ, we recover the delta case, that is, $V_{SQ} = V_D/\sigma$ for the square barrier and $V_b = V_D/(2\sigma)$ for the Rosen–Morse barrier. In Fig. A.1 we show two different widths; an experimentally feasible one where $\sigma = 0.667$ μm (Fig. A.1(a)) and a very thin barrier, $\sigma = 0.067$ μm (Fig. A.1(b)) for which the delta behavior is recovered for both, the square and the Rosen–Morse barriers.
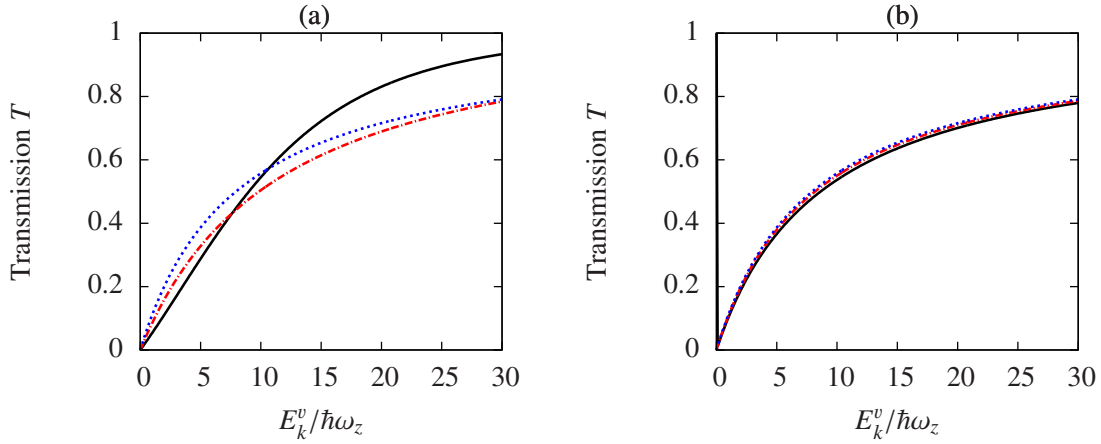
Figure A.1: Transmission coefficients, for a square barrier T_{SQ} (red solid-dotted line), a delta potential barrier T_D (blue dotted line) and a Rosen–Morse barrier T_{RM} (black solid-line) for two different widths for the square and Rosen–Morse potentials, (a) $\sigma = 0.667$ μm and (b) $\sigma = 0.067$ μm. The rest of parameter values are: $V_b = \frac{17.14\hbar\omega_z}{2\sigma}$, $V_{SQ} = \frac{17.14\hbar\omega_z}{\sigma}$, $V_D = 17.14\hbar\omega_z$ and $\omega_z = 2\pi \times 78$ Hz.

Tunneling amplitudes in sided-coupled ring potentials

Within the few-state model approach (see Sec. 2.5), the tunneling amplitudes that couple subsystem eigenstates, $\{\Phi_1(\mathbf{r}, t), ..., \Phi_i(\mathbf{r}, t), ..., \Phi_n(\mathbf{r}, t)\}$, are provided by:

$$J_{i,j} = \frac{2}{\hbar} \int_{-\infty}^{\infty} d\mathbf{r}\, \psi_j^*(\mathbf{r}) \hat{H}_{SE} \psi_i(\mathbf{r}). \tag{B.1}$$

where $\hat{H}_{SE}$ is the Schrödinger Hamiltonian given in Eq. (2.28) and $\psi_i(\mathbf{r})$ gives the spatial dependence of the ith subsystem eigenstate, $\Phi_i(\mathbf{r}, t) = a_i(t)\psi_i(\mathbf{r})$, and fulfills:

$$\int_{-\infty}^{\infty} d\mathbf{r}\, \psi_i(\mathbf{r})\psi_j(\mathbf{r}) = \delta_{i,j}. \tag{B.2}$$

Therefore, according to Eq. (B.2) few-state models are valid whenever subsystem eigenstates are orthogonal to each other or their overlap is zero. However, when subsystem trapping potentials are very close to one another an orthonormalization procedure is needed, examples being the Gram–Schmidt orthogonalization method [386] or the Holstein–Herring method [387, 388]. Nevertheless, the tunneling rates obtained through the orthogonalization protocols provide a qualitative description of the dynamics and for a quantitative description other approaches are required.

Here we present a method that allows us to calculate the tunneling amplitudes of the few-state model such that the dynamics resulting from the model is in perfect agreement with the numerical results of the 2D Schrödinger equation (SE). To illustrate this approach, we consider a single atom trapped in a system of two sided-coupled ring potentials (Sec. 6.1). The angular momentum manifold, $l = 1$, within the zero vibrational state is formed by four degenerated localized states, two in the left ring that we denote as $|L, 0, \pm 1\rangle$ and two in the right ring denoted by $|R, 0, \pm 1\rangle$ (see the general

case in Sec. 6.1). This manifold of states takes the form of a four-state Hamiltonian:

$$
\hat{H}_{FS}^{0,1} = \frac{\hbar}{2}
\begin{pmatrix}
0 & J_{L,+1}^{L,-1} & J_{L,+1}^{R,+1} & J_{L,+1}^{R,-1} \\
J_{L,+1}^{L,-1} & 0 & J_{L,+1}^{R,-1} & J_{L,+1}^{R,+1} \\
J_{L,+1}^{R,+1} & J_{L,+1}^{R,-1} & 0 & J_{L,+1}^{L,-1} \\
J_{L,+1}^{R,-1} & J_{L,+1}^{R,+1} & J_{L,+1}^{L,-1} & 0
\end{pmatrix},
\tag{B.3}
$$

with eigenstates:

$$
|\phi_0\rangle = \frac{1}{2} \left(-|L,0,+\rangle - |L,0,-\rangle + |R,0,+\rangle + |R,0,-\rangle \right)
$$

$$
|\phi_1\rangle = \frac{1}{2} \left(-|L,0,+\rangle + |L,0,-\rangle - |R,0,+\rangle + |R,0,-\rangle \right)
$$

$$
|\phi_2\rangle = \frac{1}{2} \left(+|L,0,+\rangle - |L,0,-\rangle - |R,0,+\rangle + |R,0,-\rangle \right)
$$

$$
|\phi_3\rangle = \frac{1}{2} \left(+|L,0,+\rangle - |L,0,-\rangle + |R,0,+\rangle + |R,0,-\rangle \right),
\tag{B.4}
$$

and eigenenergies:

$$
E_0 = J_{L,+1}^{L,-1} - J_{L,+1}^{R,+1} - J_{L,+1}^{R,-1}
$$

$$
E_1 = -J_{L,+1}^{L,-1} + J_{L,+1}^{R,+1} - J_{L,+1}^{R,-1}
$$

$$
E_2 = -J_{L,+1}^{L,-1} - J_{L,+1}^{R,+1} + J_{L,+1}^{R,-1}
$$

$$
E_3 = J_{L,+1}^{L,-1} + J_{L,+1}^{R,+1} + J_{L,+1}^{R,-1}.
\tag{B.5}
$$

with $J_{j,n}^{j,-n}(m)$ being the self-coupling tunnelings amplitudes and $J_{j,n}^{k,-n}(m)$ and $J_{j,n}^{k,n}(m)$ with $j \neq k$ the cross-coupling tunneling amplitudes.

The first step in our approach consists on numerically calculate the eigenenergies of the total system by integrating the 2D SE. The actual potential used in the SE consists of two sided-coupled truncated harmonic ring potentials defined in Eq. (6.8). For concreteness, let us fix the distance between rings to $d = 14$ and the ring radius to $r_0 = 5$, both given in harmonic oscillator units. Thus, integrating the SE in imaginary time (see chapter C) we obtain the eigenenergies $E_0 = 0.512236$, $E_1 = 0.515710$, $E_2 = 0.515926$ and $E_3 = 0.518584$, from which we can infer all the couplings by adding and subtracting the relations found in Eqs. (B.5) obtaining, for this particular case, $J_{L,1}^{R,1} = 3.06 \times 10^{-3}$, $J_{L,1}^{R,-1} = 3.28 \times 10^{-3}$ and $J_{L,1}^{L,-1} = -4.06 \times 10^{-4}$. Note that, due to the use of truncated potentials in the numerically approach, the obtained states slightly differ from the analytical ones Eq. (B.4)

Moreover, it is worth mentioning that this approach is applicable as long as the numerically calculated manifold of states forming the total system is widely separated from the other manifolds, and thus, the dynamics is enclosed within four states. In addition

we have also seen that the differences between this approach and the orthonormalization protocols [386–388] are enhanced in 2D systems when compared to 1D ones.

In Fig. B.1, we show the calculated self- and cross-coupling tunneling amplitudes as a function of the distance separating the two sided-coupled ring potentials (also studied in Sec. 6.1) obtained with the numerical approach presented here. Nonetheless, it is important to recall that few-state models are only valid for distances such that the overlap of the localized eigenfunctions is small, which for this example implies $(d-2r_0) > 2\sigma$, i.e., $d > 12$.

In chapter 7 we study an optical ribbon formed by 2D sided-coupled harmonic potentials using few-state models. However, in order to obtain quantitative values of the self- and cross-couplings when using the first angular momentum states of the local harmonic traps we use the procedure developed here. In Fig. B.2 we plot the tunneling amplitudes as a function of the distance separating two sided-coupled 2D harmonic potentials in the manifold of states with one unit of orbital angular momentum.

Note that in both figures the self-couplings are always much smaller than the cross-couplings. In the two in-line ring potentials we see that the self-coupling undergoes a change of sign, and in the two sided-coupled harmonic potentials we observe that the self-coupling has a non-monotonic behavior. These behaviors are produced by the fact that the self-couplings have two contributions, one coming from the kinetic term of the Hamiltonian and one from the truncated potential (see Eq. (B.1)).

Figure B.1: Tunneling amplitudes of a single atom trapped in two sided-coupled ring potentials as a function of the distance that separates them (see schematics in Fig. 6.1) when using the orbital angular momentum states of the rings with $l = 1$. Both ring radius are $r_0 = 5$ in radial harmonic oscillator units.
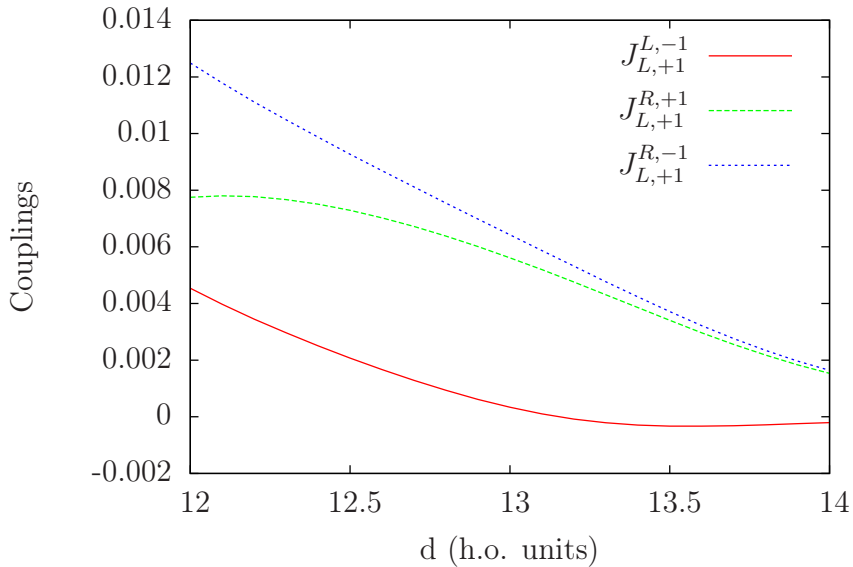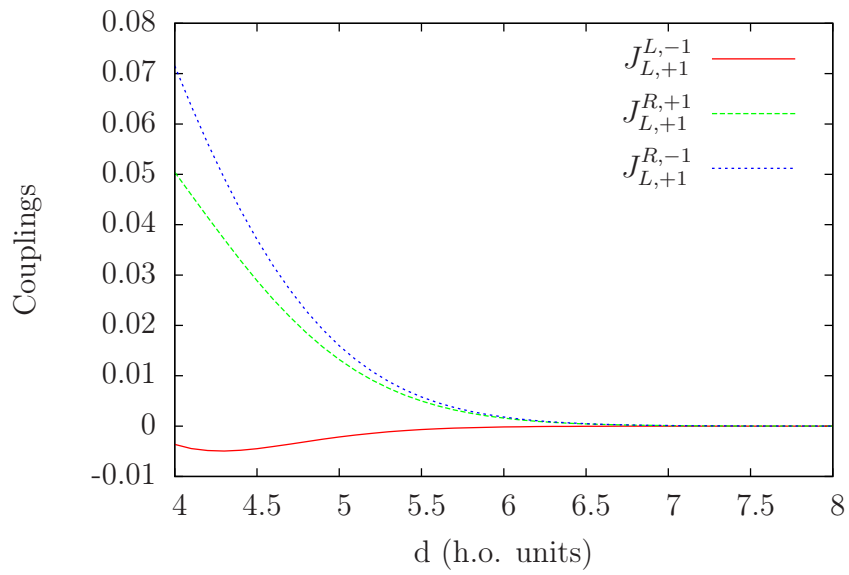
Figure B.2: Tunneling amplitudes of a single atom trapped in two sided-coupled 2D harmonic potentials as a function of the distance that separates them when being in the manifold of states with one unit of orbital angular momentum. The results are shown in 2D radial harmonic oscillator units.

Numerical methods

In this appendix, we introduce the numerical methods that we have used in the thesis. In particular, we have numerically integrated the Schrödinger equation (SE), the Gross–Pitaevskii equation (GPE) and the two-component Gross–Pitaevskii equation (TCGPE), in different dimensionalities, using the Crank–Nicolson (CN) method [389].

C.1 One-dimensional Crank-Nicolson

In order to introduce the CN method, we consider a BEC described by the 1D GPE in its dimensionless form (see Sec. 2.2 for the general 1D GPE):

$$i\frac{\partial \psi(z,t)}{\partial t} = \hat{H}\psi(z,t) = \left[-\frac{1}{2}\frac{\partial}{\partial z^2} + V(z) + g_{1D}|\psi(z,t)|^2 \right]\psi(z,t). \tag{C.1}$$

The time evolution of the wavefunction is given by $\psi(z, t + \Delta t) = e^{-i\Delta t \hat{H}}\psi(z,t)$. For numerical purposes the evolution operator, $e^{-i\Delta t \hat{H}}$, can be replaced by its Cayley's form [390]:

$$e^{-i\hat{H}\Delta t} = \frac{1 - \frac{i\Delta t}{2}\hat{H}}{1 + \frac{i\Delta t}{2}\hat{H}} + O(\Delta t^2). \tag{C.2}$$

Then, by expressing the wavefunction in a discrete time representation such that $\psi(z, n\Delta t) = \psi^n(z)$, we can write the time evolution of the wavefunction after a single time step as:

$$\left[1 + \frac{i\Delta t}{2}H^{n+1}(z)\right]\psi^{n+1}(z) = \left[1 - \frac{i\Delta t}{2}H^n(z)\right]\psi^n(z), \qquad (C.3)$$

where $H^n(z)$ is the Gross–Pitaevskii (GP) Hamiltonian, Eq. (C.1), at the nth time step. The left hand side of Eq. (C.3) shows that the CN method uses the so called backward Euler method. This method calculates the state of the system at a future time step, $t + \Delta t$, using the state of the system at $t + \Delta t$ after going trough the operation $H^{n+1}(z)\psi^{n+1}(z)$. This makes the CN approach implicit, and, in general, requires solving a system of algebraic equations to calculate the final state of the system. The right hand side of Eq. (C.3) shows that the CN method also uses the so called forward Euler method, which is explicit and depends on the wavefunction at the previous time. Therefore, the CN method is build as a combination of both Euler methods, making it a second order method in time. The solution of a linear implicit method is, in general, solved by writing the system of algebraic equations in a tridiagonal matrix form, which can then be diagonalized using any of the tridiagonalization subroutines found in the literature [391].

Note that when applying the CN method to the GPE, we obtain the typical linear term of an implicit method plus a nonlinear term, $|\psi^{n+1}(z)|^2$, coming from the Hamiltonian H^{n+1}. This nonlinear term leads to nonlinear algebraic equations which can be highly computationally demanding. Therefore, we use an intermediate state approach. First, we define $\tilde{\psi}^{n+1}(z)$ by solving Eq. (C.3), where we replace $|\psi^{n+1}(z)|^2$ with $|\psi^n(z)|^2$. Then, we use this solution to calculate the nonlinear cubic term, $|\tilde{\psi}^{n+1}(z)|^2$, in H^{n+1}. With this approach, we can find the solution at time $t + \Delta t$, $\psi^{n+1}(z)$ in Eq. (C.3), by using the tridiagonalization procedure typically employed in the CN method.

We define the discretization in space of the wavefunction as $\psi^n(z) = \psi^n_j$, along with the spatial derivatives of ψ^n_j using finite differences:

$$\frac{\partial \psi^n(z)}{\partial z} \longrightarrow \frac{\psi^n_{j_z+1} - \psi^n_{j_z-1}}{2\Delta z}, \qquad (C.4)$$

$$\frac{\partial \psi^n(z)}{\partial z} \longrightarrow \frac{\psi^n_{j_z+1} - 2\psi^n_{j_z} + \psi^n_{j_z-1}}{\Delta z^2}, \qquad (C.5)$$

such that the CN method becomes accurate in the second order, in space and time. We also need to fulfill $\Delta t < \Delta z^2/2$ [392] to have an unconditionally stable method.

Using the same CN numerical method presented here, one can calculate the eigenstates of the system using what is known as imaginary time propagation. The idea behind this method can be understood by looking at the expansion of an initial trial state in the basis of its energy eigenstates:

$$\psi(z,t) = \sum_{j}^{\infty} \phi(z)e^{-i\frac{E_j t}{\hbar}}, \qquad (C.6)$$

where E_j is the eigenenergy of the jth energy eigenstate.

When using an imaginary time, $\tau = it$, only eigenstates with very low energy will survive long imaginary time propagations. This occurs because high energy eigenstates have a larger exponential decay-rate. Note that, even the ground state is lost after long imaginary time propagations, therefore it is necessary to normalize after every imaginary time step. This method can also be used to calculate excited states by subtracting the projections to the eigenstates with lower energy at each time step. Another approach for calculating excited states is to introduce an *ansatz* orthogonal to the lower eigenstates, i.e. with no contribution of low energetic states in its eigenstate expansion, which, in general, will directly evolve to the desired excited state.

C.2 Two-dimensional Crank–Nicolson

The extension of the CN method to two dimensions is typically performed with an alternating direction implicit (ADI) approach [393] or with an operator-splitting method [394].

The ADI approach consists on splitting the finite difference evolution equation into two parts. In a first stage, one takes a half-time step using the backward Euler method in x (which involves $\psi^{n+1/2}(x,y)$) and the forward Euler method in y; and then in a second stage, the forward method in x (using the previous $\psi^{n+1/2}(x,y)$) and the backward method in y are used. As one can see, this approach employs the backward Euler method in both steps, thus it requires solving two algebraic equations with a tridiagonal matrix form. Note however, that the ADI method can be difficult to extend to nonlinear problems or when mixed derivatives appear in the equation of motion.

Here we have used the operator-splitting method to study 2D systems, in some cases, in presence of nonlinearity. This method is based on the idea of splitting the evolution operator, $e^{-i\hat{H}(x,y)\Delta t}$, into two parts, assuming that $\hat{H}(x,y) = \hat{H}(x) + \hat{H}(y)$, i.e, $e^{-i\hat{H}(x,y)\Delta t} = e^{-i\hat{H}(x)\Delta t}e^{-i\hat{H}(y)\Delta t}$. This splitting, also known as the Trotter product formula, is exact whenever the total Hamiltonian is separable and each of its terms commute, $[\hat{H}(x),\hat{H}(y)] = 0$. Nonetheless, even if the operators do not commute, the error of this splitting is $O(\Delta t^2)$, thus keeping the same local error as the CN finite difference method.

Note that, for the GPE, the Hamiltonian is never fully separable due to the non-linear cubic term and, in addition, we can also encounter situations where neither the potential is separable. Nevertheless, there exist some approaches that can be applied to use the operator-splitting method for those cases. A simple strategy is to split the nonseparable elements of the total Hamiltonian between each dimensional separable Hamiltonian. For instance, let us consider a system described by the 2D GPE with a nonseparable potential, $V(x,y) \neq V(x)V(y)$. Our approach in this situation would consist on including in each of the separable terms of the total Hamiltonian, $\hat{H}(x)$ and

$\hat{H}(y)$, the term $\frac{1}{2}V(x,y) + \frac{1}{2}g_{2D}|\psi(x,y,t)|^2$. Some approaches have been investigated using similar splitting procedures [395] or using explicit methods with different splitting arrangements [396].

Operator-splitting methods also benefit from an easy parallelization. Each dimension can be calculated separately, thus we can parallelize all x steps for each value of y and vice-versa obtaining good performances. It is also possible to parallelize the tridiagonalization of the matrices involved in the CN protocol. However, due to the large number of iterations in typical simulations, the overall performance in 2D would be affected by the time that the processor needs to create and gather the information of each subprocess launched during the parallelization. Therefore, in this thesis we have only parallelized the $e^{-i\hat{H}(x)\Delta t}$ and $e^{-i\hat{H}(y)\Delta t}$ evolutions. With this parallelization, we obtain a reduction of the total computational time in 2D of up to 5 times in a 8 core processor, without any further optimization.

Finally, it is worth mentioning that we have also written a 2D numerical code in cylindrical coordinates to efficiently study ring potentials. This approach is very useful when studying cylindrically symmetric systems where no radial dynamics is expected, as we can introduce a larger number of grid points in the angular direction than in the radial one. The code in cylindrical-coordinates was specially useful to reproduce the trapping of BECs in a blue-detuned ring [92] with a large ring radius. In particular, we defined a truncated radial grid around the ring radius, eliminating the entire central part of the ring where there was no population at any time. Note that a code in cylindrical coordinates requires cylindrical boundary conditions in the tridiagonalizaton subroutine of the angular coordinate.

Bibliography

[1] G. Gamow, Z. f. Phys. **51**, 204 (1928).

[2] R. W. Gurney and E. U. Condon, Nature **122**, 439 (1928).

[3] L. Rosenfeld, *Cosmology, Fusion and Other Matters* (Colorado Associated University Press, 1972).

[4] A. B. Balantekin and N. Takigawa, Rev. Mod. Phys. **70**, 77 (1998).

[5] C. Qi, Reviews in Physics **1**, 77 (2016).

[6] R. P. Bell, *The tunnel effect in chemistry* (Chapman and Hall London, 1980).

[7] R. J. McMahon, Science **299**, 833 (2003).

[8] Y. F. Li, T. Kaneko, and R. Hatakeyama, Appl. Phys. Lett. **96**, 023104 (2010).

[9] N. Lambert, Y. N. Chen, Y. C. Cheng, C. M. Li, G. Y. Chen, and F. Nori, Nature Phys. **9**, 10 (2013).

[10] G. Binnig and H. Rohrer, IBM J. Res. Dev. **30**, 355 (1986).

[11] J. Clarke and A. I. Braginski, *The SQUID handbook* (Wiley Online Library, 2004).

[12] K. C. Wright, R. B. Blakestad, C. J. Lobb, W. D. Phillips, and G. K. Campbell, Phys. Rev. Lett. **110**, 025302 (2013).

[13] C. Ryu, P. W. Blackburn, A. A. Blinova, and M. G. Boshier, Phys. Rev. Lett. **111**, 205301 (2013).

[14] S. Eckel, J. G. Lee, F. Jendrzejewski, N. Murray, C. W. Clark, C. J. Lobb, W. D. Phillips, M. Edwards, and G. K. Campbell, Nature **506**, 200 (2014).

[15] D. Aghamalyan, M. Cominotti, M. Rizzi, D. Rossini, F. Hekking, A. Minguzzi, L.-C. Kwek, and L. Amico, New J. Phys. **17**, 045023 (2015).

[16] A. D. Cronin, J. Schmiedmayer, and D. E. Pritchard, Rev. Mod. Phys. **81**, 1051 (2009).

[17] B. Josephson, Physics Letters **1**, 251 (1962).

[18] Y. Makhlin, G. Schön, and A. Shnirman, Rev. Mod. Phys. **73**, 357 (2001).

[19] A. Smerzi, S. Fantoni, S. Giovanazzi, and S. R. Shenoy, Phys. Rev. Lett. **79**, 4950 (1997).

[20] B. Juliá-Díaz, M. Melé-Messeguer, M. Guilleumas, and A. Polls, Phys. Rev. A **80**, 043622 (2009).

[21] B. Juliá-Díaz, J. Martorell, M. Melé-Messeguer, and A. Polls, Phys. Rev. A **82**, 063626 (2010).

[22] B. Juliá-Díaz, T. Zibold, M. K. Oberthaler, M. Melé-Messeguer, J. Martorell, and A. Polls, Phys. Rev. A **86**, 023615 (2012).

[23] L. Amico and M. G. Boshier, ArXiv e-prints (2015), arXiv:1511.07215 [quant-ph] .

[24] B. T. Seaman, M. Krämer, D. Z. Anderson, and M. J. Holland, Phys. Rev. A **75**, 023615 (2007).

[25] A. Ramanathan, K. C. Wright, S. R. Muniz, M. Zelan, W. T. Hill, C. J. Lobb, K. Helmerson, W. D. Phillips, and G. K. Campbell, Phys. Rev. Lett. **106**, 130401 (2011).

[26] S. C. Caliga, C. J. E. Straatsma, A. A. Zozulya, and D. Z. Anderson, ArXiv e-prints (2012), arXiv:1208.3109 [physics.atom-ph] .

[27] J. J. Sakurai and J. Napolitano, *Modern quantum mechanics* (Addison-Wesley, 2011).

[28] A. J. Leggett, Contemporary Physics **25**, 583 (1984).

[29] S. N. Bose, Z. phys **26**, 178 (1924).

[30] A. Einstein, Sitzungsber. Preuss. Akad. Wiss. , 2161 (1924).

[31] A. Einstein, Sitzungsber. Kgl. Preuss. Akad. Wiss. **1**, 3 (1925).

[32] M. H. Anderson, J. R. Ensher, M. R. Matthews, C. E. Wieman, and E. A. Cornell, Science **269**, 198 (1995).

[33] K. B. Davis, M. O. Mewes, M. R. Andrews, N. J. van Druten, D. S. Durfee, D. M. Kurn, and W. Ketterle, Phys. Rev. Lett. **75**, 3969 (1995).

[34] C. C. Bradley, C. A. Sackett, J. J. Tollett, and R. G. Hulet, Phys. Rev. Lett. **75**, 1687 (1995).

[35] S. Chu, C. Cohen-Tannoudji, and W. D. Phillips, Nobel Lectures (2002).

[36] J. Weiner, *Cold and ultracold collisions in quantum microscopic and mesoscopic systems* (Cambridge University Press, 2003).

[37] S. Inouye, M. Andrews, J. Stenger, H.-J. Miesner, D. Stamper-Kurn, and W. Ketterle, Nature **392**, 151 (1998).

[38] J. L. Roberts, N. R. Claussen, J. P. Burke, C. H. Greene, E. A. Cornell, and C. E. Wieman, Phys. Rev. Lett. **81**, 5109 (1998).

[39] A. J. Moerdijk, B. J. Verhaar, and A. Axelsson, Phys. Rev. A **51**, 4852 (1995).

[40] J. L. Roberts, N. R. Claussen, S. L. Cornish, and C. E. Wieman, Phys. Rev. Lett. **85**, 728 (2000).

[41] C. Chin, R. Grimm, P. Julienne, and E. Tiesinga, Rev. Mod. Phys. **82**, 1225 (2010).

[42] P. O. Fedichev, Y. Kagan, G. V. Shlyapnikov, and J. T. M. Walraven, Phys. Rev. Lett. **77**, 2913 (1996).

[43] M. Theis, G. Thalhammer, K. Winkler, M. Hellwig, G. Ruff, R. Grimm, and J. H. Denschlag, Phys. Rev. Lett. **93**, 123001 (2004).

[44] K. E. Strecker, G. B. Partridge, A. G. Truscott, and R. G. Hulet, Nature **417**, 150 (2002).

[45] L. Khaykovich, F. Schreck, G. Ferrari, T. Bourdel, J. Cubizolles, L. D. Carr, Y. Castin, and C. Salomon, Science **296**, 1290 (2002).

[46] D. Poletti, T. J. Alexander, E. A. Ostrovskaya, B. Li, and Y. S. Kivshar, Phys. Rev. Lett. **101**, 150403 (2008).

[47] A. D. Martin, C. S. Adams, and S. A. Gardiner, Phys. Rev. Lett. **98**, 020402 (2007).

[48] J. Polo and V. Ahufinger, Phys. Rev. A **88**, 053628 (2013).

[49] L. D. Carr, R. R. Miller, D. R. Bolton, and S. A. Strong, Phys. Rev. A **86**, 023621 (2012).

[50] S. Damgaard Hansen, N. Nygaard, and K. Mølmer, ArXiv e-prints (2012), arXiv:1210.1681 [cond-mat.quant-gas] .

[51] H. Sakaguchi and M. Tamura, JPSJ **74**, 292 (2005).

[52] J. L. Helm, T. P. Billam, and S. A. Gardiner, Phys. Rev. A **85**, 053621 (2012).

[53] J. Holmer, J. Marzuola, and M. Zworski, Commun. Math. Phys. **274**, 187 (2007).

[54] J. Holmer, J. Marzuola, and M. Zworski, J. Nonlinear Sci. **17**, 349 (2007).

[55] B. Gertjerenken and C. Weiss, J. Phys. B: At. Mol. Opt. Phys. **45**, 165301 (2012).

[56] B. Gertjerenken, T. P. Billam, L. Khaykovich, and C. Weiss, Phys. Rev. A **86**, 033608 (2012).

[57] C. Weiss and Y. Castin, J. Phys. A: Math. and Theo. **45**, 455306 (2012).

[58] A. L. Marchant, T. P. Billam, T. P. Wiles, M. M. H. Yu, S. A. Gardiner, and S. L. Cornish, Nature Commun. **4**, 1865 (2013).

[59] R. Menchon-Enrich, A. Benseny, V. Ahufinger, A. D. Greentree, T. Busch, and J. Mompart, Rep. Prog. Phys. **79**, 074401 (2016).

[60] M. Albiez, R. Gati, J. Fölling, S. Hunsmann, M. Cristiani, and M. K. Oberthaler, Phys. Rev. Lett. **95**, 010402 (2005).

[61] J. Struck, C. Ölschläger, M. Weinberg, P. Hauke, J. Simonet, A. Eckardt, M. Lewenstein, K. Sengstock, and P. Windpassinger, Phys. Rev. Lett. **108**, 225304 (2012).

[62] K. Jiménez-García, L. J. LeBlanc, R. A. Williams, M. C. Beeler, A. R. Perry, and I. B. Spielman, Phys. Rev. Lett. **108**, 225303 (2012).

[63] J. Polo, J. Mompart, and V. Ahufinger, Phys. Rev. A **93**, 033613 (2016).

[64] M. Aidelsburger, M. Atala, S. Nascimbène, S. Trotzky, Y.-A. Chen, and I. Bloch, Phys. Rev. Lett. **107**, 255301 (2011).

[65] J. Struck, M. Weinberg, C. Ölschläger, P. Windpassinger, J. Simonet, K. Sengstock, R. Höppner, P. Hauke, A. Eckardt, M. Lewenstein, and L. Mathey, Nature Phys. **9**, 738 (2013).

[66] M. Aidelsburger, M. Atala, M. Lohse, J. T. Barreiro, B. Paredes, and I. Bloch, Phys. Rev. Lett. **111**, 185301 (2013).

[67] G. Jotzu, M. Messer, R. Desbuquois, M. Lebrat, T. Uehlinger, D. Greif, and T. Esslinger, Nature **515**, 237 (2014).

[68] H. Miyake, G. A. Siviloglou, C. J. Kennedy, W. C. Burton, and W. Ketterle, Phys. Rev. Lett. **111**, 185302 (2013).

[69] T. Dubček, C. J. Kennedy, L. Lu, W. Ketterle, M. Soljačić, and H. Buljan, Phys. Rev. Lett. **114**, 225301 (2015).

[70] L. Dobrek, M. Gajda, M. Lewenstein, K. Sengstock, G. Birkl, and W. Ertmer, Phys. Rev. A **60**, R3381 (1999).

[71] J. L. Helm, S. L. Cornish, and S. A. Gardiner, Phys. Rev. Lett. **114**, 134101 (2015).

[72] A. L. Fetter and D. L. Feder, Phys. Rev. A **58**, 3185 (1998).

[73] F. Dalfovo, L. Pitaevskii, and S. Stringari, Phys. Rev. A **54**, 4213 (1996).

[74] J. Polo, A. Benseny, T. Busch, V. Ahufinger, and J. Mompart, New J. Phys. **18**, 015010 (2016).

[75] N. V. Vitanov, T. Halfmann, B. W. Shore, and K. Bergmann, Annual Review of Physical Chemistry **52**, 763 (2001).

[76] K. Bergmann, H. Theuer, and B. W. Shore, Rev. Mod. Phys. **70**, 1003 (1998).

[77] G. Pelegrí, J. Polo, A. Turpin, M. Lewenstein, J. Mompart, and V. Ahufinger, ArXiv e-prints (2016), 1609.02729 [quant-ph] .

[78] L. P. Pitaevskii and S. Stringari, *Bose–Einstein condensation* (Oxford University Press, 2003).

[79] F. Dalfovo, S. Giorgini, L. P. Pitaevskii, and S. Stringari, Rev. Mod. Phys. **71**, 463 (1999).

[80] C. Pethick and H. Smith, *Bose-Einstein Condensation in Dilute Gases* (Cambridge University Press, 2002).

[81] E. P. Gross, Phys. Rev. **106**, 161 (1957).

[82] V. Ginzburg and L. Pitaevskii, Sov. Phys. JETP **7**, 858 (1958).

[83] S. Stock, Z. Hadzibabic, B. Battelier, M. Cheneau, and J. Dalibard, Phys. Rev. Lett. **95**, 190403 (2005).

[84] J. Esteve, J.-B. Trebbia, T. Schumm, A. Aspect, C. I. Westbrook, and I. Bouchoule, Phys. Rev. Lett. **96**, 130403 (2006).

[85] Z. Hadzibabic, P. Krüger, M. Cheneau, B. Battelier, and J. Dalibard, Nature **441**, 1118 (2006).

[86] S. Tung, G. Lamporesi, D. Lobser, L. Xia, and E. A. Cornell, Phys. Rev. Lett. **105**, 230408 (2010).

[87] S. P. Rath, T. Yefsah, K. J. Günter, M. Cheneau, R. Desbuquois, M. Holzmann, W. Krauth, and J. Dalibard, Phys. Rev. A **82**, 013609 (2010).

[88] T. Yefsah, R. Desbuquois, L. Chomaz, K. J. Günter, and J. Dalibard, Phys. Rev. Lett. **107**, 130401 (2011).

[89] C.-L. Hung, X. Zhang, N. Gemelke, and C. Chin, Nature **470**, 236 (2011).

[90] J.-Y. Choi, S. W. Seo, W. J. Kwon, and Y.-I. Shin, Phys. Rev. Lett. **109**, 125301 (2012).

[91] L.-C. Ha, C.-L. Hung, X. Zhang, U. Eismann, S.-K. Tung, and C. Chin, Phys. Rev. Lett. **110**, 145302 (2013).

[92] A. Turpin, J. Polo, Y. V. Loiko, J. Küber, F. Schmaltz, T. K. Kalkandjiev, V. Ahufinger, G. Birkl, and J. Mompart, Opt. Express **23**, 1638 (2015).

[93] C. D. Rossi, R. Dubessy, K. Merloti, M. de Goër de Herve, T. Badr, A. Perrin, L. Longchambon, and H. Perrin, New J. Phys. **18**, 062001 (2016).

[94] A. Rakonjac, A. L. Marchant, T. P. Billam, J. L. Helm, M. M. H. Yu, S. A. Gardiner, and S. L. Cornish, Phys. Rev. A **93**, 013607 (2016).

[95] A. Görlitz, J. M. Vogels, A. E. Leanhardt, C. Raman, T. L. Gustavson, J. R. Abo-Shaeer, A. P. Chikkatur, S. Gupta, S. Inouye, T. Rosenband, and W. Ketterle, Phys. Rev. Lett. **87**, 130402 (2001).

[96] H. Moritz, T. Stöferle, M. Köhl, and T. Esslinger, Phys. Rev. Lett. **91**, 250402 (2003).

[97] D. Hellweg, L. Cacciapuoti, M. Kottke, T. Schulte, K. Sengstock, W. Ertmer, and J. J. Arlt, Phys. Rev. Lett. **91**, 010406 (2003).

[98] B. L. Tolra, K. M. O'Hara, J. H. Huckans, W. D. Phillips, S. L. Rolston, and J. V. Porto, Phys. Rev. Lett. **92**, 190401 (2004).

[99] T. Kinoshita, T. Wenger, and D. S. Weiss, Phys. Rev. Lett. **95**, 190406 (2005).

[100] C.-S. Chuu, F. Schreck, T. P. Meyrath, J. L. Hanssen, G. N. Price, and M. G. Raizen, Phys. Rev. Lett. **95**, 260403 (2005).

[101] Y. Colombe, T. Steinmetz, G. Dubois, F. Linke, D. Hunger, and J. Reichel, Nature **450**, 272 (2007).

[102] S. Hofferberth, I. Lesanovsky, B. Fischer, T. Schumm, and J. Schmiedmayer, Nature **449**, 324 (2007).

[103] M. Eckart, R. Walser, and W. P. Schleich, New J. Phys. **10**, 045024 (2008).

[104] A. L. Marchant, T. P. Billam, M. M. H. Yu, A. Rakonjac, J. L. Helm, J. Polo, C. Weiss, S. A. Gardiner, and S. L. Cornish, Phys. Rev. A **93**, 021604 (2016).

[105] D. S. Petrov, *Bose-Einstein condensation in low-dimensional trapped gases*, Ph.D. thesis, Van der Waals-Zeeman Institute (WZI) (2003).

[106] V. Popov, *Functional integrals in quantum field theory and statistical physics* (D. Reidel Publishing Co., 1983).

[107] J. W. Kane and L. P. Kadanoff, Phys. Rev. **155**, 80 (1967).

[108] D. S. Petrov, M. Holzmann, and G. V. Shlyapnikov, Phys. Rev. Lett. **84**, 2551 (2000).

[109] V. L. Berezinskii, Sov. Phys. JETP **32**, 493 (1971).

[110] V. L. Kosterlitz, Sov. Phys. JETP **34**, 610 (1972).

[111] J. M. Berezinskii and D. J. Thouless, J. Phys. C **6**, 1181 (1973).

[112] R. J. Fletcher, M. Robert-de Saint-Vincent, J. Man, N. Navon, R. P. Smith, K. G. H. Viebahn, and Z. Hadzibabic, Phys. Rev. Lett. **114**, 255302 (2015).

[113] D. S. Petrov, G. V. Shlyapnikov, and J. T. M. Walraven, Phys. Rev. Lett. **85**, 3745 (2000).

[114] L. Tonks, Phys. Rev. **50**, 955 (1936).

[115] E. Lifshitz and L. Pitaevskii, *Statistical physics, vol. 2* (Pergamon, Oxford, 1980).

[116] L. H. Thomas, Mathematical Proceedings of the Cambridge Philosophical Society **23**, 542 (1927).

[117] E. Fermi, Rend. Accad. Naz. Lincei **6**, 602 (1927).

[118] P. G. Drazin, *Solitons* (Cambridge University Press, 1983).

[119] A. B. S. V. E. Zakharov, JETP **34**, 62 (1972).

[120] P. G. Kevrekidis, D. J. Frantzeskakis, and R. Carretero-González, *Emergent nonlinear phenomena in Bose-Einstein condensates: theory and experiment*, Vol. 45 (Springer Science & Business Media, 2007).

[121] C. J. Pethick and H. Smith, *Bose–Einstein Condensation in Dilute Gases*, 2nd ed. (Cambridge University Press, 2008).

[122] A. D. Martin, C. S. Adams, and S. A. Gardiner, Phys. Rev. A **77**, 013620 (2008).

[123] P. A. Ruprecht, M. J. Holland, K. Burnett, and M. Edwards, Phys. Rev. A **51**, 4704 (1995).

[124] M. I. Weinstein, Commun. Math. Phys. **87**, 567 (1983).

[125] A. Gammal, T. Frederico, and L. Tomio, Phys. Rev. A **64**, 055602 (2001).

[126] V. M. Pérez-García, H. Michinel, J. I. Cirac, M. Lewenstein, and P. Zoller, Phys. Rev. A **56**, 1424 (1997).

[127] J. L. Roberts, N. R. Claussen, S. L. Cornish, E. A. Donley, E. A. Cornell, and C. E. Wieman, Phys. Rev. Lett. **86**, 4211 (2001).

[128] S. L. Cornish, S. T. Thompson, and C. E. Wieman, Phys. Rev. Lett. **96**, 170401 (2006).

[129] C. Eigen, A. L. Gaunt, A. Suleymanzade, N. Navon, Z. Hadzibabic, and R. P. Smith, ArXiv e-prints (2016), 1609.00352 [cond-mat.quant-gas] .

[130] B. Eiermann, T. Anker, M. Albiez, M. Taglieber, P. Treutlein, K.-P. Marzlin, and M. K. Oberthaler, Phys. Rev. Lett. **92**, 230401 (2004).

[131] S. Burger, K. Bongs, S. Dettmer, W. Ertmer, K. Sengstock, A. Sanpera, G. V. Shlyapnikov, and M. Lewenstein, Phys. Rev. Lett. **83**, 5198 (1999).

[132] J. Denschlag, J. E. Simsarian, D. L. Feder, C. W. Clark, L. A. Collins, J. Cubizolles, L. Deng, E. W. Hagley, K. Helmerson, W. P. Reinhardt, S. L. Rolston, B. I. Schneider, and W. D. Phillips, Science **287**, 97 (2000).

[133] Z. Dutton, M. Budde, C. Slowe, and L. V. Hau, Science **293**, 663 (2001).

[134] N. S. Ginsberg, J. Brand, and L. V. Hau, Phys. Rev. Lett. **94**, 040403 (2005).

[135] M. R. Andrews, C. G. Townsend, H.-J. Miesner, D. S. Durfee, D. M. Kurn, and W. Ketterle, Science **275**, 637 (1997).

[136] A. Weller, J. P. Ronzheimer, C. Gross, J. Esteve, M. K. Oberthaler, D. J. Frantzeskakis, G. Theocharis, and P. G. Kevrekidis, Phys. Rev. Lett. **101**, 130401 (2008).

[137] P. Engels and C. Atherton, Phys. Rev. Lett. **99**, 160405 (2007).

[138] P. G. Kevrekidis and D. J. Frantzeskakis, Mod. Phys. Lett. B **18**, 173 (2004).

[139] T. Kovachy, J. M. Hogan, A. Sugarbaker, S. M. Dickerson, C. A. Donnelly, C. Overstreet, and M. A. Kasevich, Phys. Rev. Lett. **114**, 143004 (2015).

[140] G. Modugno, M. Modugno, F. Riboli, G. Roati, and M. Inguscio, Phys. Rev. Lett. **89**, 190404 (2002).

[141] G. Ferrari, M. Inguscio, W. Jastrzebski, G. Modugno, G. Roati, and A. Simoni, Phys. Rev. Lett. **89**, 053202 (2002).

[142] G. Thalhammer, G. Barontini, L. De Sarlo, J. Catani, F. Minardi, and M. Inguscio, Phys. Rev. Lett. **100**, 210402 (2008).

[143] D. J. McCarron, H. W. Cho, D. L. Jenkin, M. P. Köppinger, and S. L. Cornish, Phys. Rev. A **84**, 011603 (2011).

[144] F. Wang, X. Li, D. Xiong, and D. Wang, J. Phys. B: At. Mol. Opt. Phys. **49**, 015302 (2016).

[145] S. B. Papp, J. M. Pino, and C. E. Wieman, Phys. Rev. Lett. **101**, 040402 (2008).

[146] C. J. Myatt, E. A. Burt, R. W. Ghrist, E. A. Cornell, and C. E. Wieman, Phys. Rev. Lett. **78**, 586 (1997).

[147] J. Stenger, S. Inouye, D. Stamper-Kurn, H.-J. Miesner, A. Chikkatur, and W. Ketterle, Nature **396**, 345 (1998).

[148] D. S. Hall, M. R. Matthews, J. R. Ensher, C. E. Wieman, and E. A. Cornell, Phys. Rev. Lett. **81**, 1539 (1998).

[149] M. R. Matthews, B. P. Anderson, P. C. Haljan, D. S. Hall, C. E. Wieman, and E. A. Cornell, Phys. Rev. Lett. **83**, 2498 (1999).

[150] P. Maddaloni, M. Modugno, C. Fort, F. Minardi, and M. Inguscio, Phys. Rev. Lett. **85**, 2413 (2000).

[151] G. Delannoy, S. G. Murdoch, V. Boyer, V. Josse, P. Bouyer, and A. Aspect, Phys. Rev. A **63**, 051602 (2001).

[152] V. Schweikhard, I. Coddington, P. Engels, S. Tung, and E. A. Cornell, Phys. Rev. Lett. **93**, 210403 (2004).

[153] R. P. Anderson, C. Ticknor, A. I. Sidorov, and B. V. Hall, Phys. Rev. A **80**, 023603 (2009).

[154] T.-L. Ho and V. B. Shenoy, Phys. Rev. Lett. **77**, 3276 (1996).

[155] B. D. Esry, C. H. Greene, J. P. Burke, Jr., and J. L. Bohn, Phys. Rev. Lett. **78**, 3594 (1997).

[156] H. Pu and N. P. Bigelow, Phys. Rev. Lett. **80**, 1130 (1998).

[157] D. S. Hall, M. R. Matthews, J. R. Ensher, C. E. Wieman, and E. A. Cornell, Phys. Rev. Lett. **81**, 1539 (1998).

[158] K. Kasamatsu, Y. Yasui, and M. Tsubota, Phys. Rev. A **64**, 053605 (2001).

[159] P. Mason, The European Physical Journal B **86**, 1 (2013).

[160] N. R. Cooper, E. H. Rezayi, and S. H. Simon, Phys. Rev. Lett. **95**, 200402 (2005).

[161] J. Zhang and H. Zhai, Phys. Rev. Lett. **95**, 200403 (2005).

[162] J.-y. Choi, W. J. Kwon, and Y.-i. Shin, Phys. Rev. Lett. **108**, 035301 (2012).

[163] H. Zeng, W. Zhang, and F. Lin, Phys. Rev. A **52**, 2155 (1995).

[164] B. Tanatar and K. Erkan, Phys. Rev. A **62**, 053601 (2000).

[165] R. A. Barankov, Phys. Rev. A **66**, 013612 (2002).

[166] P. Ao and S. T. Chui, Phys. Rev. A **58**, 4836 (1998).

[167] E. Timmermans, Phys. Rev. Lett. **81**, 5718 (1998).

[168] P. Ao and S. T. Chui, Phys. Rev. A **58**, 4836 (1998).

[169] T. Congy, A. M. Kamchatnov, and N. Pavloff, ArXiv e-prints (2016), arXiv:1607.08760 [cond-mat.quant-gas] .

[170] T. Bienaimé, E. Fava, G. Colzi, C. Mordini, S. Serafini, C. Qu, S. Stringari, G. Lamporesi, and G. Ferrari, ArXiv e-prints (2016), arXiv:1607.04574 [cond-mat.quant-gas] .

[171] K. L. Lee, N. B. Jørgensen, I.-K. Liu, L. Wacker, J. J. Arlt, and N. P. Proukakis, Phys. Rev. A **94**, 013602 (2016).

[172] M. Abad, A. Recati, S. Stringari, and F. Chevy, Eur. Phys. J. D **69**, 1 (2015).

[173] J. Polo, V. Ahufinger, P. Mason, S. Sridhar, T. P. Billam, and S. A. Gardiner, Phys. Rev. A **91**, 053626 (2015).

[174] T. Bergeman, G. Erez, and H. J. Metcalf, Phys. Rev. A **35**, 1535 (1987).

[175] J. D. Miller, R. A. Cline, and D. J. Heinzen, Phys. Rev. A **47**, R4567 (1993).

[176] D. E. Pritchard, E. L. Raab, V. Bagnato, C. E. Wieman, and R. N. Watts, Phys. Rev. Lett. **57**, 310 (1986).

[177] E. L. Raab, M. Prentiss, A. Cable, S. Chu, and D. E. Pritchard, Phys. Rev. Lett. **59**, 2631 (1987).

[178] W. Ketterle and N. V. Druten, Adv. At. Mol. Opt. Phys. **37**, 181 (1996).

[179] J. Fortágh and C. Zimmermann, Rev. Mod. Phys. **79**, 235 (2007).

[180] P. Böhi, M. F. Riedel, J. Hoffrogge, J. Reichel, T. W. Hänsch, and P. Treutlein, Nature Phys. **5**, 592 (2009).

[181] M. F. Riedel, P. Böhi, Y. Li, T. W. Hänsch, A. Sinatra, and P. Treutlein, Nature **464**, 1170 (2010).

[182] J. Dalibard and C. Cohen-Tannoudji, J. Opt. Soc. Am. B **2**, 1707 (1985).

[183] S. K. Schnelle, E. D. van Ooijen, M. J. Davis, N. R. Heckenberg, and H. Rubinsztein-Dunlop, Opt. Express **16**, 1405 (2008).

[184] N. Houston, E. Riis, and A. S. Arnold, J. Phys. B: At. Mol. Opt. Phys. **41**, 211001 (2008).

[185] K. Henderson, C. Ryu, C. MacCormick, and M. G. Boshier, New J. Phys. **11**, 043030 (2009).

[186] S. Franke-Arnold, J. Leach, M. J. Padgett, V. E. Lembessis, D. Ellinas, A. J. Wright, J. M. Girkin, P. Öhberg, and A. S. Arnold, Opt. Express **15**, 8619 (2007).

[187] A. S. Arnold, Opt. Lett. **37**, 2505 (2012).

[188] S. Chu, Rev. Mod. Phys. **70**, 685 (1998).

[189] C. N. Cohen-Tannoudji, Rev. Mod. Phys. **70**, 707 (1998).

[190] W. D. Phillips, Rev. Mod. Phys. **70**, 721 (1998).

[191] R. Grimm, M. Weidemüller, and Y. B. Ovchinnikov, Adv. At. Mol. Opt. Phys. **42**, 95 (2000).

[192] N. Lundblad, M. Schlosser, and J. V. Porto, Phys. Rev. A **81**, 031611 (2010).

[193] S. Chu, J. E. Bjorkholm, A. Ashkin, and A. Cable, Phys. Rev. Lett. **57**, 314 (1986).

[194] G. Birkl, F. Buchkremer, R. Dumke, and W. Ertmer, Opt. Commun. **191**, 67 (2001).

[195] L. Isenhower, W. Williams, A. Dally, and M. Saffman, Opt. Lett. **34**, 1159 (2009).

[196] P. Rudy, R. Ejnisman, A. Rahman, S. Lee, and N. P. Bigelow, Opt. Express **8**, 159 (2001).

[197] G. Li, S. Zhang, L. Isenhower, K. Maller, and M. Saffman, Opt. Lett. **37**, 851 (2012).

[198] V. G. Shvedov, C. Hnatovsky, N. Shostka, and W. Krolikowski, J. Opt. Soc. Am. B **30**, 1 (2013).

[199] A. Turpin, *Conical refraction: fundamentals and applications*, Ph.D. thesis, Universitat Autònoma de Barcelona (2015).

[200] J. A. Sauer, M. D. Barrett, and M. S. Chapman, Phys. Rev. Lett. **87**, 270401 (2001).

[201] S. Wu, W. Rooijakkers, P. Striehl, and M. Prentiss, Phys. Rev. A **70**, 013409 (2004).

[202] A. S. Arnold, C. S. Garvie, and E. Riis, Phys. Rev. A **73**, 041606 (2006).

[203] P. Weiss, M. Knufinke, S. Bernon, D. Bothner, L. Sárkány, C. Zimmermann, R. Kleiner, D. Koelle, J. Fortágh, and H. Hattermann, Phys. Rev. Lett. **114**, 113003 (2015).

[204] A. S. Arnold, J. Phys. B: At. Mol. Opt. Phys. **37**, L29 (2004).

[205] S. Gupta, K. W. Murch, K. L. Moore, T. P. Purdy, and D. M. Stamper-Kurn, Phys. Rev. Lett. **95**, 143201 (2005).

[206] A. D. West, C. G. Wade, K. J. Weatherill, and I. G. Hughes, Appl. Phys. Lett. **101**, 023115 (2012).

[207] P. F. Griffin, E. Riis, and A. S. Arnold, Phys. Rev. A **77**, 051402 (2008).

[208] J. D. Pritchard, A. N. Dinkelaker, A. S. Arnold, P. F. Griffin, and E. Riis, New J. Phys. **14**, 103047 (2012).

[209] B. E. Sherlock, M. Gildemeister, E. Owen, E. Nugent, and C. J. Foot, Phys. Rev. A **83**, 043408 (2011).

[210] D. S. Naik and C. Raman, Phys. Rev. A **71**, 033617 (2005).

[211] C. Ryu, M. F. Andersen, P. Cladé, V. Natarajan, K. Helmerson, and W. D. Phillips, Phys. Rev. Lett. **99**, 260401 (2007).

[212] E. M. Wright, J. Arlt, and K. Dholakia, Phys. Rev. A **63**, 013608 (2000).

[213] S. Moulder, S. Beattie, R. P. Smith, N. Tammuz, and Z. Hadzibabic, Phys. Rev. A **86**, 013629 (2012).

[214] S. Beattie, S. Moulder, R. J. Fletcher, and Z. Hadzibabic, Phys. Rev. Lett. **110**, 025301 (2013).

[215] E. Courtade, O. Houde, J.-F. m. c. Clément, P. Verkerk, and D. Hennequin, Phys. Rev. A **74**, 031403 (2006).

[216] S. E. Olson, M. L. Terraciano, M. Bashkansky, and F. K. Fatemi, Phys. Rev. A **76**, 061404 (2007).

[217] A. I. Yakimenko, Y. M. Bidasyuk, O. O. Prikhodko, S. I. Vilchinskii, E. A. Ostro-vskaya, and Y. S. Kivshar, Phys. Rev. A **88**, 043637 (2013).

[218] T. Lauber, J. Küber, O. Wille, and G. Birkl, Phys. Rev. A **84**, 043641 (2011).

[219] L. Corman, L. Chomaz, T. Bienaimé, R. Desbuquois, C. Weitenberg, S. Nascimbène, J. Dalibard, and J. Beugnon, Phys. Rev. Lett. **113**, 135302 (2014).

[220] R. Menchon-Enrich, S. McEndoo, J. Mompart, V. Ahufinger, and T. Busch, Phys. Rev. A **89**, 013626 (2014).

[221] B. Juliá-Díaz, D. Dagnino, M. Lewenstein, J. Martorell, and A. Polls, Phys. Rev. A **81**, 023615 (2010).

[222] B. Juliá-Díaz, J. Martorell, and A. Polls, Phys. Rev. A **81**, 063625 (2010).

[223] J. Gillet, M. A. Garcia-March, T. Busch, and F. Sols, Phys. Rev. A **89**, 023614 (2014).

[224] J. L. Rubio, V. Ahufinger, T. Bush, and J. Mompart, (2016), submitted to Phys. Rev. A.

[225] R. Geiger, V. Ménoret, G. Stern, N. Zahzam, P. Cheinet, B. Battelier, A. Villing, F. Moron, M. Lours, Y. Bidel, A. Bresson, A. Landragin, and P. Bouyer, Nature Commun. **2**, 474 (2011).

[226] F. Riehle, T. Kisters, A. Witte, J. Helmcke, and C. J. Bordé, Phys. Rev. Lett. **67**, 177 (1991).

[227] D. S. Durfee, Y. K. Shaham, and M. A. Kasevich, Phys. Rev. Lett. **97**, 240801 (2006).

[228] S. Wu, E. Su, and M. Prentiss, Phys. Rev. Lett. **99**, 173201 (2007).

[229] J. K. Stockton, K. Takase, and M. A. Kasevich, Phys. Rev. Lett. **107**, 133001 (2011).

[230] M. J. Snadden, J. M. McGuirk, P. Bouyer, K. G. Haritos, and M. A. Kasevich, Phys. Rev. Lett. **81**, 971 (1998).

[231] A. Peters, K. Y. Chung, and S. Chu, Nature **400**, 849 (1999).

[232] G. Rosi, L. Cacciapuoti, F. Sorrentino, M. Menchetti, M. Prevedelli, and G. M. Tino, Phys. Rev. Lett. **114**, 013001 (2015).

[233] J. B. Fixler, G. T. Foster, J. M. McGuirk, and M. A. Kasevich, Science **315**, 74 (2007).

[234] G. Lamporesi, A. Bertoldi, L. Cacciapuoti, M. Prevedelli, and G. M. Tino, Phys. Rev. Lett. **100**, 050801 (2008).

[235] G. Rosi, F. Sorrentino, L. Cacciapuoti, M. Prevedelli, and G. M. Tino, Nature **510**, 518 (2014).

[236] P. Cladé, E. de Mirandes, M. Cadoret, S. Guellati-Khélifa, C. Schwob, F. m. c. Nez, L. Julien, and F. m. c. Biraben, Phys. Rev. Lett. **96**, 033001 (2006).

[237] R. Bouchendira, P. Cladé, S. Guellati-Khélifa, F. m. c. Nez, and F. m. c. Biraben, Phys. Rev. Lett. **106**, 080801 (2011).

[238] M. A. Hohensee, S. Chu, A. Peters, and H. Müller, Phys. Rev. Lett. **106**, 151102 (2011).

[239] S. Dimopoulos, P. W. Graham, J. M. Hogan, and M. A. Kasevich, Phys. Rev. Lett. **98**, 111102 (2007).

[240] H. Müller, S.-w. Chiow, S. Herrmann, S. Chu, and K.-Y. Chung, Phys. Rev. Lett. **100**, 031101 (2008).

[241] S. Dimopoulos, P. W. Graham, J. M. Hogan, M. A. Kasevich, and S. Rajendran, Phys. Rev. D **78**, 122002 (2008).

[242] P. W. Graham, J. M. Hogan, M. A. Kasevich, and S. Rajendran, Phys. Rev. Lett. **110**, 171102 (2013).

[243] E. W. Hagley, L. Deng, M. Kozuma, M. Trippenbach, Y. B. Band, M. Edwards, M. Doery, P. S. Julienne, K. Helmerson, S. L. Rolston, and W. D. Phillips, Phys. Rev. Lett. **83**, 3112 (1999).

[244] I. Bloch, T. W. Hänsch, and T. Esslinger, Nature **403**, 166 (2000).

[245] Y. Castin and J. Dalibard, Phys. Rev. A **55**, 4330 (1997).

[246] J. Javanainen and M. Wilkens, Phys. Rev. Lett. **78**, 4675 (1997).

[247] M. Lewenstein and L. You, Phys. Rev. Lett. **77**, 3489 (1996).

[248] M. Fattori, C. D'Errico, G. Roati, M. Zaccanti, M. Jona-Lasinio, M. Modugno, M. Inguscio, and G. Modugno, Phys. Rev. Lett. **100**, 080405 (2008).

[249] C. Chin, R. Grimm, P. Julienne, and E. Tiesinga, Rev. Mod. Phys. **82**, 1225 (2010).

[250] G. B. Jo, Y. Shin, S. Will, T. A. Pasquini, M. Saba, W. Ketterle, D. E. Pritchard, M. Vengalattore, and M. Prentiss, Phys. Rev. Lett. **98**, 030407 (2007).

[251] T. Berrada, S. van Frank, R. Bücker, T. Schumm, J.-F. Schaff, and J. Schmiedmayer, Nat. Commun. **4**, 2077 (2013).

[252] M. Kitagawa and M. Ueda, Phys. Rev. A **47**, 5138 (1993).

[253] J. Estève, C. Gross, A. Weller, S. Giovanazzi, and M. Oberthaler, Nature **455**, 1216 (2008).

[254] M. F. Riedel, P. Böhi, Y. Li, T. W. Hänsch, A. Sinatra, and P. Treutlein, Nature **464**, 1170 (2010).

[255] C. Gross, T. Zibold, E. Nicklas, J. Estève, and M. Oberthaler, Nature **464**, 1165 (2010).

[256] C. Gross, H. Strobel, E. Nicklas, T. Zibold, N. Bar-Gill, G. Kurizki, and M. K. Oberthaler, Nature **480**, 219 (2011).

[257] B. Lücke, M. Scherer, J. Kruse, L. Pezzé, F. Deuretzbacher, P. Hyllus, O. Topic, J. Peise, W. Ertmer, J. Arlt, L. Santos, A. Smerzi, and C. Klempt, Science **334**, 773 (2011).

[258] C. Hamley, C. Gerving, T. Hoang, E. Bookjans, and M. Chapman, Nat. Phys. **8**, 305 (2012).

[259] S. Gupta, K. Dieckmann, Z. Hadzibabic, and D. E. Pritchard, Phys. Rev. Lett. **89**, 140401 (2002).

[260] Y.-J. Wang, D. Z. Anderson, V. M. Bright, E. A. Cornell, Q. Diot, T. Kishimoto, M. Prentiss, R. A. Saravanan, S. R. Segal, and S. Wu, Phys. Rev. Lett. **94**, 090405 (2005).

[261] O. Garcia, B. Deissler, K. J. Hughes, J. M. Reeves, and C. A. Sackett, Phys. Rev. A **74**, 031601 (2006).

[262] G.-B. Jo, J.-H. Choi, C. A. Christensen, Y.-R. Lee, T. A. Pasquini, W. Ketterle, and D. E. Pritchard, Phys. Rev. Lett. **99**, 240406 (2007).

[263] S. J. Kim, H. Yu, S. T. Gang, and J. B. Kim, ArXiv e-prints (2016), arXiv:1601.06901 [physics.atom-ph] .

[264] P. Dyke, S. Lei, and R. Hulet, in *Book of Abstracts of the 23rd International Conference on Atomic Physics* (ICAP2012) p. 174.

[265] M. Kasevich, (Jan. 17-21, 2012), presentation at the NASA Quantum Future Technologies Conference, http://quantum.nasa.gov/agenda.html .

[266] A. D. Martin and J. Ruostekoski, New J. Phys. **14**, 043040 (2012).

[267] T. P. Billam, S. L. Cornish, and S. A. Gardiner, Phys. Rev. A **83**, 041602 (2011).

[268] J. Cuevas, P. G. Kevrekidis, B. A. Malomed, P. Dyke, and R. G. Hulet, New J. Phys. **15**, 063006 (2013).

[269] J. L. Helm, S. J. Rooney, C. Weiss, and S. A. Gardiner, Phys. Rev. A **89**, 033610 (2014).

[270] J. H. V. Nguyen, P. Dyke, D. Luo, B. A. Malomed, and R. G. Hulet, Nature Phys. **10**, 918 (2014).

[271] G. D. McDonald, C. C. N. Kuhn, K. S. Hardman, S. Bennetts, P. J. Everitt, P. A. Altin, J. E. Debs, J. D. Close, and N. P. Robins, Phys. Rev. Lett. **113**, 013002 (2014).

[272] H. Michinel, A. Paredes, M. M. Valado, and D. Feijoo, Phys. Rev. A **86**, 013620 (2012).

[273] T. P. Billam, S. A. Wrathmall, and S. A. Gardiner, Phys. Rev. A **85**, 013627 (2012).

[274] T. Ernst and J. Brand, Phys. Rev. A **81**, 033614 (2010).

[275] A. D. Martin, *Theoretical Studies of Bright Solitons in Trapped Atomic Bose-Einstein Condensates*, Ph.D. thesis, University of Durham (2008).

[276] S. Jian-Wen, H. Wen-Hua, Z. Hong-Hua, and L. Xiao-Bing, Commun. Theor. Phys. **50**, 89 (2008).

[277] J. Lekner, Am. J. Phys. **75**, 1151 (2007).

[278] H. Ishkhanyan and V. Krainov, JETP **109**, 585 (2009).

[279] C. Lee and J. Brand, , Europhys. Lett. **73**, 321 (2006).

[280] Y. Loiko, V. Ahufinger, R. Corbalán, G. Birkl, and J. Mompart, Phys. Rev. A **83**, 033629 (2011).

[281] H. Sakaguchi and M. Tamura, J. Phys. Soc. Japan **74**, 292 (2005).

[282] S. D. Hansen, N. Nygaard, and K. Mølmer, e-print (2012), arXiv:1210.1681 .

[283] L. D. Landau and E. M. Lifshitz, *Quantum Mechanics: Non-relativistic Theory*, 2nd ed. (Pergamon, Oxford, 1965).

[284] D. Bohm, *Quantum theory* (Prentice-Hall, 1951).

[285] J. P. Gordon, Opt. Lett. **8**, 596 (1983).

[286] J. Holmer, J. Marzuola, and M. Zworski, J. Nonlinear Sci. **17**, 349 (2007).

[287] B. D. Esry, C. H. Greene, J. P. Burke, Jr., and J. L. Bohn, Phys. Rev. Lett. **78**, 3594 (1997).

[288] F. Riboli and M. Modugno, Phys. Rev. A **65**, 063614 (2002).

[289] E. Lundh, C. J. Pethick, and H. Smith, Phys. Rev. A **55**, 2126 (1997).

[290] U. A. Khawaja, C. J. Pethick, and H. Smith, Phys. Rev. A **60**, 1507 (1999).

[291] A. Gallemí, A. M. Mateo, R. Mayol, and M. Guilleumas, New J. Phys. **18**, 015003 (2016).

[292] B. Van Schaeybroeck, Phys. Rev. A **78**, 023624 (2008).

[293] B. Van Schaeybroeck and J. O. Indekeu, Phys. Rev. A **91**, 013626 (2015).

[294] Z. Deng, B. V. Schaeybroeck, C.-Y. Lin, N. V. Thu, and J. O. Indekeu, Phys. A: Stat. Mech. App. **444**, 1027 (2016).

[295] M. Trippenbach, K. Góral, K. Rzazewski, B. Malomed, and Y. B. Band, J. Phys. B: At. Mol. Opt. Phys. **33**, 4017 (2000).

[296] S. Theodorakis, Phys. Rev. A **70**, 063619 (2004).

[297] A. Muñoz Mateo and V. Delgado, Phys. Rev. A **74**, 065602 (2006).

[298] A. M. n. Mateo and V. Delgado, Phys. Rev. A **75**, 063610 (2007).

[299] H. Salman, Phys. Rev. A **85**, 063622 (2012).

[300] S. Gautam and S. K. Adhikari, Phys. Rev. A **92**, 023616 (2015).

[301] M. Eto, K. Kasamatsu, M. Nitta, H. Takeuchi, and M. Tsubota, Phys. Rev. A **83**, 063603 (2011).

[302] S. Hastings and J. McLeod, Archive for Rational Mechanics and Analysis **73**, 31 (1980).

[303] M. Ablowitz and H. Segur, SIAM **4**, 181 (1981).

[304] U. Gaubatz, P. Rudecki, S. Schiemann, and K. Bergmann, J. Chem. Phys. **92**, 5363 (1990).

[305] E. M. Wright, J. Arlt, and K. Dholakia, Phys. Rev. A **63**, 013608 (2000).

[306] E. Courtade, O. Houde, J.-F. m. c. Clément, P. Verkerk, and D. Hennequin, Phys. Rev. A **74**, 031403 (2006).

[307] S. E. Olson, M. L. Terraciano, M. Bashkansky, and F. K. Fatemi, Phys. Rev. A **76**, 061404 (2007).

[308] S. Franke-Arnold, J. Leach, M. J. Padgett, V. E. Lembessis, D. Ellinas, A. J. Wright, J. M. Girkin, P. Öhberg, and A. S. Arnold, Opt. Express **15**, 8619 (2007).

[309] N. Houston, E. Riis, and A. S. Arnold, J. Phys. B: At. Mol. Opt. Phys. **41**, 211001 (2008).

[310] A. I. Yakimenko, Y. M. Bidasyuk, O. O. Prikhodko, S. I. Vilchinskii, E. A. Ostrovskaya, and Y. S. Kivshar, Phys. Rev. A **88**, 043637 (2013).

[311] L. Corman, L. Chomaz, T. Bienaimé, R. Desbuquois, C. Weitenberg, S. Nascimbène, J. Dalibard, and J. Beugnon, Phys. Rev. Lett. **113**, 135302 (2014).

[312] B. E. Sherlock, M. Gildemeister, E. Owen, E. Nugent, and C. J. Foot, Phys. Rev. A **83**, 043408 (2011).

[313] I. Lesanovsky and W. von Klitzing, Phys. Rev. Lett. **99**, 083001 (2007).

[314] Y. Japha, O. Arzouan, Y. Avishai, and R. Folman, Phys. Rev. Lett. **99**, 060402 (2007).

[315] A. Ruschhaupt and J. G. Muga, Phys. Rev. A **70**, 061604 (2004).

[316] J. A. Stickney, D. Z. Anderson, and A. A. Zozulya, Phys. Rev. A **75**, 013608 (2007).

[317] J. J. Thorn, E. A. Schoene, T. Li, and D. A. Steck, Phys. Rev. Lett. **100**, 240407 (2008).

[318] R. A. Pepino, J. Cooper, D. Z. Anderson, and M. J. Holland, Phys. Rev. Lett. **103**, 140405 (2009).

[319] A. Benseny, S. Fernández-Vidal, J. Bagudà, R. Corbalán, A. Picón, L. Roso, G. Birkl, and J. Mompart, Phys. Rev. A **82**, 013604 (2010).

[320] J. Javanainen, S. M. Paik, and S. M. Yoo, Phys. Rev. A **58**, 580 (1998).

[321] L. Salasnich, A. Parola, and L. Reatto, Phys. Rev. A **59**, 2990 (1999).

[322] L. Plaja and J. San Román, Phys. Rev. A **69**, 063612 (2004).

[323] L. Amico, A. Osterloh, and F. Cataliotti, Phys. Rev. Lett. **95**, 063201 (2005).

[324] M. F. Andersen, C. Ryu, P. Cladé, V. Natarajan, A. Vaziri, K. Helmerson, and W. D. Phillips, Phys. Rev. Lett. **97**, 170406 (2006).

[325] A. M. Rey, K. Burnett, I. I. Satija, and C. W. Clark, Phys. Rev. A **75**, 063616 (2007).

[326] T. Wang, J. Javanainen, and S. F. Yelin, Phys. Rev. A **76**, 011601 (2007).

[327] D. Aghamalyan, L. Amico, and L. C. Kwek, Phys. Rev. A **88**, 063627 (2013).

[328] Y.-H. Wang, A. Kumar, F. Jendrzejewski, R. M. Wilson, M. Edwards, S. Eckel, G. K. Campbell, and C. W. Clark, New J. Phys. **17**, 125012 (2015).

[329] R. Mathew, A. Kumar, S. Eckel, F. Jendrzejewski, G. K. Campbell, M. Edwards, and E. Tiesinga, Phys. Rev. A **92**, 033602 (2015).

[330] F. Jendrzejewski, S. Eckel, N. Murray, C. Lanier, M. Edwards, C. J. Lobb, and G. K. Campbell, Phys. Rev. Lett. **113**, 045305 (2014).

[331] T. c. v. Opatrný and K. K. Das, Phys. Rev. A **79**, 012113 (2009).

[332] S. McEndoo, S. Croke, J. Brophy, and T. Busch, Phys. Rev. A **81**, 043640 (2010).

[333] T. Morgan, B. O'Sullivan, and T. Busch, Phys. Rev. A **83**, 053620 (2011).

[334] A. Benseny, J. Bagudà, X. Oriols, and J. Mompart, Phys. Rev. A **85**, 053619 (2012).

[335] Y. Loiko, V. Ahufinger, R. Corbalán, G. Birkl, and J. Mompart, Phys. Rev. A **83**, 033629 (2011).

[336] T. Morgan, L. J. O'Riordan, N. Crowley, B. O'Sullivan, and T. Busch, Phys. Rev. A **88**, 053618 (2013).

[337] K. Eckert, M. Lewenstein, R. Corbalán, G. Birkl, W. Ertmer, and J. Mompart, Phys. Rev. A **70**, 023606 (2004).

[338] K. Eckert, J. Mompart, R. Corbalán, M. Lewenstein, and G. Birkl, Opt. Commun. **264**, 264 (2006).

[339] A. D. Greentree, J. H. Cole, A. R. Hamilton, and L. C. L. Hollenberg, Phys. Rev. B **70**, 235317 (2004).

[340] E. M. Graefe, H. J. Korsch, and D. Witthaut, Phys. Rev. A **73**, 013617 (2006).

[341] M. Rab, J. H. Cole, N. G. Parker, A. D. Greentree, L. C. L. Hollenberg, and A. M. Martin, Phys. Rev. A **77**, 061602 (2008).

[342] V. O. Nesterenko, A. N. Novikov, F. F. de Souza Cruz, and E. L. Lapolli, Laser Phys. **19**, 616 (2009).

[343] M. Rab, A. L. C. Hayward, J. H. Cole, A. D. Greentree, and A. M. Martin, Phys. Rev. A **86**, 063605 (2012).

[344] R. Menchon-Enrich, S. McEndoo, T. Busch, V. Ahufinger, and J. Mompart, Phys. Rev. A **89**, 053611 (2014).

[345] S. Longhi, G. Della Valle, M. Ornigotti, and P. Laporta, Phys. Rev. B **76**, 201101 (2007).

[346] Y. Lahini, F. Pozzi, M. Sorel, R. Morandotti, D. N. Christodoulides, and Y. Silberberg, Phys. Rev. Lett. **101**, 193901 (2008).

[347] R. Menchon-Enrich, A. Llobera, V. J. Cadarso, J. Mompart, and V. Ahufinger, IEEE Phot. Tech. Lett. **24**, 536 (2012).

[348] R. Menchon-Enrich, A. Llobera, J. Vila-Planas, V. J. Cadarso, J. Mompart, and V. Ahufinger, Light Sci. Appl. **2**, e90 (2013).

[349] R. Menchon-Enrich, J. Mompart, and V. Ahufinger, Phys. Rev. B **89**, 094304 (2014).

[350] E. Kierig, U. Schnorrberger, A. Schietinger, J. Tomkovic, and M. K. Oberthaler, Phys. Rev. Lett. **100**, 190405 (2008).

[351] H. Lignier, C. Sias, D. Ciampini, Y. Singh, A. Zenesini, O. Morsch, and E. Arimondo, Phys. Rev. Lett. **99**, 220403 (2007).

[352] A. Zenesini, H. Lignier, D. Ciampini, O. Morsch, and E. Arimondo, Phys. Rev. Lett. **102**, 100403 (2009).

[353] A. Eckardt, C. Weiss, and M. Holthaus, Phys. Rev. Lett. **95**, 260404 (2005).

[354] C. E. Creffield and T. S. Monteiro, Phys. Rev. Lett. **96**, 210403 (2006).

[355] J. Struck, C. Ölschläger, R. Le Targat, P. Soltan-Panahi, A. Eckardt, M. Lewenstein, P. Windpassinger, and K. Sengstock, Science **333**, 996 (2011).

[356] G. A. Sinuco-León, K. A. Burrows, A. S. Arnold, and B. M. Garraway, Nature Commun. **5**, 5289 (2014).

[357] S. Eckel, F. Jendrzejewski, A. Kumar, C. J. Lobb, and G. K. Campbell, Phys. Rev. X **4**, 031052 (2014).

[358] C. Ryu, K. C. Henderson, and M. G. Boshier, New J. Phys. **16**, 013046 (2014).

[359] L. Amico, D. Aghamalyan, F. Auksztol, H. Crepaz, R. Dumke, and L. C. Kwek, Sci. Rep. **4**, 4298 (2014).

[360] G. Watanabe and C. J. Pethick, Phys. Rev. A **76**, 021605 (2007).

[361] M. Lewenstein, A. Sanpera, and V. Ahufinger, *Ultracold Atoms in Optical Lattices: Simulating quantum many-body systems* (OUP Oxford, 2012).

[362] I. Bloch, J. Dalibard, and S. Nascimbene, Nature Phys. **8**, 267 (2012).

[363] D. Jaksch and P. Zoller, New J. Phys. **5**, 56 (2003).

[364] K. Osterloh, M. Baig, L. Santos, P. Zoller, and M. Lewenstein, Phys. Rev. Lett. **95**, 010403 (2005).

[365] E. J. Mueller, Phys. Rev. A **70**, 041603 (2004).

[366] F. Gerbier and J. Dalibard, New J. Phys. **12**, 033007 (2010).

[367] A. Eckardt, P. Hauke, P. Soltan-Panahi, C. Becker, K. Sengstock, and M. Lewenstein, EPL **89**, 10010 (2010).

[368] J. Struck, C. Ölschläger, M. Weinberg, P. Hauke, J. Simonet, A. Eckardt, M. Lewenstein, K. Sengstock, and P. Windpassinger, Phys. Rev. Lett. **108**, 225304 (2012).

[369] P. Hauke, O. Tieleman, A. Celi, C. Ölschläger, J. Simonet, J. Struck, M. Weinberg, P. Windpassinger, K. Sengstock, M. Lewenstein, and A. Eckardt, Phys. Rev. Lett. **109**, 145301 (2012).

[370] J. Dalibard, F. Gerbier, G. Juzeliūnas, and P. Öhberg, Rev. Mod. Phys. **83**, 1523 (2011).

[371] N. Goldman, G. Juzeliūnas, P. Öhberg, and I. B. Spielman, Rep. Prog. Phys. **77**, 126401 (2014).

[372] N. Goldman and J. Dalibard, Phys. Rev. X **4**, 031027 (2014).

[373] M. Aidelsburger, M. Lohse, C. Schweizer, M. Atala, J. T. Barreiro, S. Nascimbène, N. Cooper, I. Bloch, and N. Goldman, Nature Phys. **11**, 162 (2015).

[374] C. J. Kennedy, W. C. Burton, W. C. Chung, and W. Ketterle, Nature Phys. (2015).

[375] M. Atala, M. Aidelsburger, M. Lohse, J. T. Barreiro, B. Paredes, and I. Bloch, Nature Phys. **10**, 588 (2014).

[376] B. K. Stuhl, H.-I. Lu, L. M. Aycock, D. Genkina, and I. B. Spielman, Science **349**, 1514 (2015).

[377] M. Mancini, G. Pagano, G. Cappellini, L. Livi, M. Rider, J. Catani, C. Sias, P. Zoller, M. Inguscio, M. Dalmonte, and L. Fallani, Science **349**, 1510 (2015).

[378] A. Celi, P. Massignan, J. Ruseckas, N. Goldman, I. B. Spielman, G. Juzeliūnas, and M. Lewenstein, Phys. Rev. Lett. **112**, 043001 (2014).

[379] N. Y. Yao, C. R. Laumann, A. V. Gorshkov, H. Weimer, L. Jiang, J. I. Cirac, P. Zoller, and M. D. Lukin, Nature Commun. **4**, 1585 (2013).

[380] C. Dlaska, B. Vermersch, and P. Zoller, ArXiv e-prints (2016), 1607.01154 [quant-ph] .

[381] F. Nogrette, H. Labuhn, S. Ravets, D. Barredo, L. Béguin, A. Vernier, T. Lahaye, and A. Browaeys, Phys. Rev. X **4**, 021034 (2014).

[382] H. Tamura, T. Unakami, J. He, Y. Miyamoto, and K. Nakagawa, Opt. Express **24**, 8132 (2016).

[383] A. Kiely, A. Benseny, T. Busch, and A. Ruschhaupt, ArXiv e-prints (2016), 1603.05927 [quant-ph] .

[384] O. Boada, A. Celi, J. Rodríguez-Laguna, J. I. Latorre, and M. Lewenstein, New J. Phys. **17**, 045007 (2015).

[385] T. Ozawa and I. Carusotto, ArXiv e-prints (2016), 1607.00140 [cond-mat.quant-gas] .

[386] L. N. Trefethen and D. Bau, *Numerical linear algebra* (Society for Industrial and Applied Mathematics, 1997).

[387] C. Herring, Rev. Mod. Phys. **34**, 631 (1962).

[388] T. Holstein, J. Phys. Chem. **56**, 832 (1952).

[389] J. Crank and P. Nicolson, Mathematical Proceedings of the Cambridge Philosophical Society **43**, 50 (2008).

[390] W. Ames, *Numerical methods for partial differential equations*, J. Comp. Sci. Appl. Math (Academic Press, 1977).

[391] W. H. Press, *Numerical recipes 3rd edition: The art of scientific computing* (Cambridge university press, 2007).

[392] W. H. Press, S. A. Teukolsky, W. T. Vetterling, and B. P. Flannery, *Numerical recipes in Fortran 77: the art of scientific computing* (Cambridge University Press, 1992).

[393] J. Douglas, Numerische Mathematik **4**, 41 (1962).

[394] K. A. Bagrynovskii and S. K. Godunov, Dokl. Akad. Nauk. **115**, 431 (1965).

[395] M. Thalhammer, M. Caliari, and C. Neuhauser, J. Comput. Phys. **228**, 822 (2009).

[396] C. Lubich, Math. of Comp. **77**, 2141 (2008).